Faculty of Physics and Astronomy
University of Heidelberg

Diploma thesis
in Physics

submitted by
Florian Ritterbusch
born in Bielefeld

Issued 2009

Realization of a collimated beam of metastable atoms for ATTA of Argon 39

This diploma thesis has been carried out by Florian Ritterbusch at the
Kirchhoff Institute for Physics
under the supervision of
Prof. Dr. M. K. Oberthaler

Realisierung eines kollimierten Strahls metastabiler Atome für ATTA von Argon 39

In dieser Diplomarbeit wird der Beginn der experimentellen Umsetzung von Atom Trap Trace Analysis (ATTA) zur Detektion des seltenen Argon Isotops ^{39}Ar vorgestellt. Im Rahmen der vorliegenden Arbeit wurden sowohl ein Strahl metastabiler Atome als auch der Aufbau der Atomstrahl-Kollimation realisiert.

Die Erzeugung der metastabilen Atome wurde mit einer Radiofrequenz (RF) Gasentladung realisiert. Zur Erzeugung dieses RF-Feldes wurden verschiedene Techniken getestet und die entsprechenden Geräte entwickelt. Eines dieser Bauteile — ein sogenannter Multivibrator — stellte sich in der Erzeugung metastabiler Argonatome bei sehr niedrigen Drücken von bis zu 10^{-6} mbar als sehr effizient heraus. Es zeigte sich, dass dies wesentlich für die Spektroskopie von ^{39}Ar ist.

Der metastabile Atomstrahl wurde über einen Spektroskopie-Aufbau charakterisiert. Aus den Spektroskopiesignalen konnten wesentliche Strahlparameter,
wie die Geschwindigkeitsverteilung und der Fluss metastabiler Atome, berechnet werden.

Um die optimalen Parameter für den Entwurf der Kollimationsstufe zu bestimmen, wurde eine detaillierte theoretische Untersuchung einschließlich numerischer Simulationen durchgeführt. Das technische Design und die Fertigung des Kollimators baute auf den Ergebnissen der Simulationen auf. Eine erste Messung mit dem Kollimator konnte durchgeführt werden, aus der eine Fluss-Überhöhung in der Magneto-Optischen Falle von etwa 50 berechnet wurde. Der theoretisch maximal erreichbare Wert von 125 kann durch genauere Justage näher erreicht werden.

Die Realisierung der ersten apparativen Aufbauten für das ^{39}Ar-ATTA Experiment ist der Anfang einer vielversprechenden Methode zur Altersbestimmung von Wasser für den Zeitraum der letzten fünfzig bis tausend Jahre.

Realization of a collimated beam of metastable atoms for ATTA of Argon 39

In this diploma thesis the launched experimental realization of Atom Trap Trace Analysis (ATTA) for the rare Argon isotope ^{39}Ar is presented. The parts of the experimental apparatus that have been implemented within the scope of this thesis are the metastable atomic beam source as well as the setup for the beam collimation. For the production of the metastable Argon beam a Radio Frequency (RF) excitation scheme has been employed. Several techniques for the generation of the RF-field have been tested and the corresponding experimental devices have been developed. One of these devices – a so-called multivibrator – turned out to be very efficient in the production of metastable Argon atoms even at very low pressures down to 10^{-6} mbar. This resulted to be essential for the spectroscopy of ^{39}Ar.

In order to characterize the metastable Argon beam, a spectroscopy setup has been

assembled. Essential beam parameters, such as the velocity distribution and flux of metastable atoms could be obtained by analysis of the resulting spectroscopy signals.
In order to find the optimal design parameters for the collimation setup, a detailed theoretical study including numerical simulations has been accomplished. The collimation apparatus has been technically designed and manufactured according to the simulation results. A first measurement with the collimator could be performed from which a flux enhancement of about 50 in the Magneto-Optical trap could be calculated. The theoretically obtained maximum of a 125 may be achieved by further improvement of the setup alignment.
The presented first implementations of the ATTA setup for ^{39}Ar depict the first steps towards a promising method for dating water of the past fifty to thousand years.

Contents

1. Introduction 9
- 1.1. Dating of water 10
- 1.2. The tracer Argon 39 12
- 1.3. Applications for dating with Argon 39 13
- 1.4. Methods for measuring ^{39}Ar 15
  - 1.4.1. Low-Level-Decay Counting (LLC) 16
  - 1.4.2. Accelerator Mass Spectrometry (AMS) 17
  - 1.4.3. Atom Trap Trace Analysis (ATTA) 17

2. Principles of Laser Cooling and Trapping 19
- 2.1. The scattering force for a two-level atom at rest 19
- 2.2. Optical Molasses 23
- 2.3. Zeeman slowing 24
- 2.4. Magneto-Optical-Trap (MOT) 26
- 2.5. Doppler cooling limit 27

3. Properties of Argon 29
- 3.1. Argon 40 29
- 3.2. Argon 39 32

4. Atom Trap Trace Analysis of ^{39}Ar 35
- 4.1. Principle of ATTA 35
- 4.2. Experimental setup 37

5. Metastable Argon Source 39
- 5.1. Atom Beam Shaping 39
- 5.2. Excitation methods 41
  - 5.2.1. Excitation by electron impact 41
  - 5.2.2. Optical excitation 41
- 5.3. Excitation by RF-discharge 43
- 5.4. Source characterization 45
- 5.5. Velocity distribution of the atom beam 48
- 5.6. Beam parameters from absorption 50
- 5.7. Beam parameters from longitudinal fluorescence 54
- 5.8. Beam parameters from transversal fluorescence 56
- 5.9. Comparison of the characterization results 57
- 5.10. Pressure dependence 57
- 5.11. Power dependence 59

6. Atomic Beam Collimation **61**
6.1. Collimating with tilted mirrors 65
6.2. Simulation 67
6.3. Design 74
6.4. First result 75

7. Summary and Outlook **77**
7.1. Estimation of the ^{39}Ar counting rate in the MOT 77
7.2. Measurement of a natural water sample 78

A. Detailed transition scheme of ^{40}Ar **81**

B. circuit of multivibrator **83**

C. circuit of power supply **85**

D. Some constants **87**

E. acknowledgements **89**

1. Introduction

In hydrology the *age* of water, i.e. the time between last equilibrium with atmosphere and the sampling of the water, is of great interest. With ocean circulations, climate reconstruction and groundwater management just a few possible applications are named. Important progress in this field has been made by using different isotopes to *trace* water and by employing methods from nuclear physics to measure these so-called *tracers* [1]. This gave birth to a new field of study known as *isotope hydrology*.

Since then several methods to measure rare isotopes, such as ^{14}C, ^{18}O or ^{222}Rn have been developed and further improved to meet the demanding rareness of those isotopes. Examples are Accelerator Mass Spectrometry (AMS), Low Level Decay Counting (LLC) or Resonance Ionization Mass Spectroscopy (RIMS) [2].

In 1999, a new method for the detection of the rare Krypton isotopes ^{85}Kr and ^{81}Kr has been developed at the Argonne National Laboratories. This so-called Atom Trap Trace Analysis (ATTA) is based on single atom counting via a Magneto-Optical Trap [3]. Not much later, the first hydrological field study has been performed with the help of this new detection method, in which water samples from the Sahara could be dated back to ages of up to one million years [4].

Upon this success this method has also been used to detect other rare isotopes important for the environmental sciences as e.g. ^{41}Ca [5],[6].

The rare isotope ^{39}Ar has been identified to be a highly valuable tracer in hydrology [7]. So far its usage in hydrology is severely limited due to the lack of a detection method, that requires only small sample sizes, short measuring times and comprises a table top apparatus. Using the method of ATTA for ^{39}Ar could potentially fulfill these requirements, while meeting its extremely low abundance.

After providing a brief overview of current dating methods and their corresponding tracers in isotope hydrology, the following sections will then focus on dating with ^{39}Ar.

1.1. Dating of water

There are four basic principles of dating in isotope hydrology as indicated in fig. 1.1. The first one uses the **radioactive decay** of unstable isotopes such as ^{14}C, ^{81}Kr or ^{39}Ar. Their decreasing number with time is described by the natural decay law

$$n(t) = n_0 \cdot e^{-\frac{t}{\tau}} \tag{1.1}$$

Knowing the initial particle number n_0 and the particle number at the time of sampling $n(t)$ of a certain radioisotope with the half-life

$$T_{1/2} = \tau \cdot \ln 2 \tag{1.2}$$

where τ is called the mean lifetime, one can calculate the age of the sample

$$t = \tau \ln \left[\frac{n_0}{n(t)} \right] \tag{1.3}$$

The difficulty in this method lies in determining the initial amount n_0 of the radioisotope, which might vary over the years.

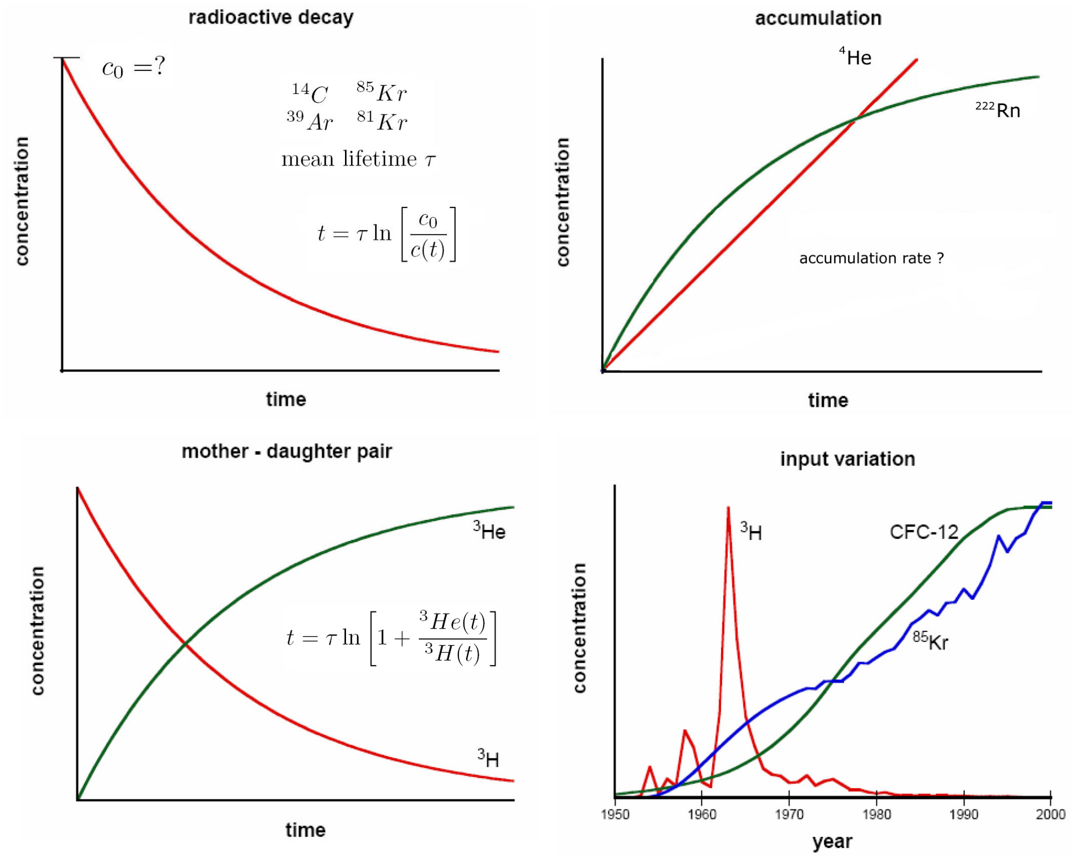

Figure 1.1.: Principles of dating methods in isotope hydrology [8, 9]

In the second method, this drawback is overcome for radioisotopes whose decay products are stable as is the case for Tritium ^{3}H. One of its decay products is the stable ^{3}He. Hence, the sum of **mother and daughter** of the decay is constant. Thus, the age can be expressed in terms of currently measurable quantities (fig. 1.1)
The third method makes use of certain isotopes, that are present in the subsoil. For instance, the **accumulation** of ^{222}Rn in infiltrating water is a function of time. However, the problem that this accumulation function is often not well known remains.
The fourth method makes use of the **input variation** of tracers in the atmosphere, usually due to human activities. Typical examples are ^{3}H, ^{85}Kr or SF$_6$ that originate from bomb tests in the 60's, nuclear power stations or reprocessing plants and electric industry, respectively. For unstable isotopes this method has to be combined with the first method in order to obtain the age from the actual measurement.
Dating with a radioisotope is only possible if the age of the sample lies within a certain time range given by the half-life $T_{1/2}$ of the radiosotope and the precision of the method. If the latter is for instance 5%, only samples with an age t fulfilling

$$95\% > \frac{n(t)}{n_0} > 5\% \tag{1.4}$$

can be dated. Using (1.3) this condition translates to a dating range of about

$$\frac{1}{10}\, T_{1/2} \; ... \; 4\, T_{1/2} \tag{1.5}$$

Hence, each tracer has its specific dating range as illustrated in fig. 1.2

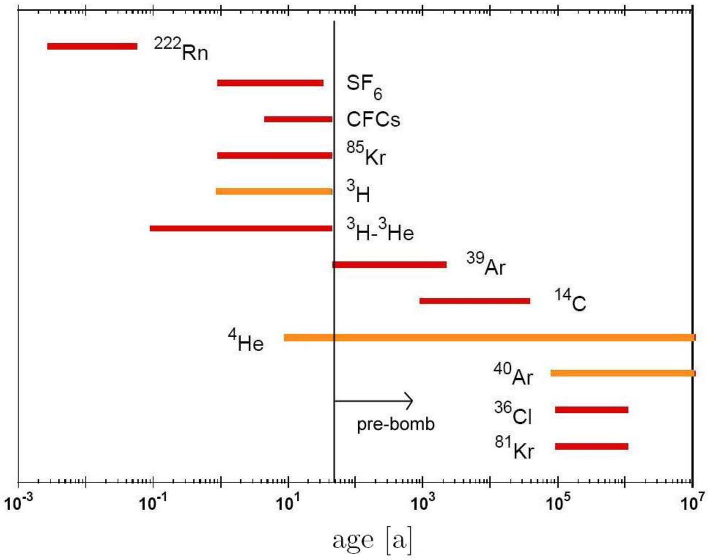

isotope	half-life
^{222}Rn	3.8 d
^{85}Kr	10.76 a
^{3}H	12.32 a
^{14}C	5730 a
^{81}Kr	210'000 a
^{36}Cl	308'000 a
^{39}Ar	269 a

Figure 1.2.: Dating range of several environmental tracers [8]

In fact, the only radioisotope that lies in the important time window between 50 and 1000 years[1] is ^{39}Ar with its half-life $T_{1/2} = 269a$.

---

[1] The yellow indicated ^{4}He-dating is very insecure and can only yield qualitative results.

1.2. The tracer Argon 39

Apart from being the only radioisotope in that time-slot, ^{39}Ar is an ideal tracer because

- as a noble gas it is chemically inert. Thus, no additional variations have to be included when calculating the age
- atmospheric ^{39}Ar is almost exclusively cosmic-ray produced by the ^{40}Ar(n,2n)^{39}Ar process [7]. Consequently, its atmospheric concentration is constant. As this is also the case for the total Argon concentration, the ^{39}Ar/Ar ratio has been constant within 7% over the last 1000 years (the time span of interest) [7]

The last fact greatly simplifies the dating method, as now the age can be expressed in terms of currently measurable quantities. If ^{39}Ar(t) denotes the amount of ^{39}Ar at the time t of sampling and ^{39}Ar(0) the initial amount when the sample was in equilibrium with the atmosphere then

$$\frac{^{39}Ar(t)}{^{39}Ar(0)} = \frac{\left(\frac{^{39}Ar}{Ar}\right)_{sample}}{\left(\frac{^{39}Ar}{Ar}\right)_{modern}} =: \frac{R_{sample}}{R_{modern}} \tag{1.6}$$

where R_{modern} denotes the modern (atmospheric) isotopic abundance and R_{sample} the isotopic ratio in the sample. Thus, equation (1.3) simplifies to

$$t = \tau \cdot \ln \left[\frac{R_{modern}}{R_{sample}}\right] \tag{1.7}$$

Despite being an ideal tracer in many respects, its extremely low isotopic abundance [2]

$$R_{modern} = 8.1 \pm 0.3 \cdot 10^{-16} \tag{1.8}$$

poses severe problems to current detection methods. In comparison, the isotopic abundance of modern ^{14}C is $\sim 10^{-12}$. To further stress the upper number, note that there are only about 8000 ^{39}Ar atoms in a litre of modern water.
Due to to the lack of a proper method to measure ^{39}Ar, only very few studies have been performed with its help. Some of these studies will be presented in the subsequent section.

1.3. Applications for dating with Argon 39

The time range of the past 50-1000 years is very important for water dating and makes ^{39}Ar a valuable tracer in hydrology. This has been first proposed by [10]. In principle, it can be used in any aquatic system like oceans, glaciers or groundwater.
In **oceans**, circulations as the global conveyor belt and mixing processes, as for the study of CO_2-uptake and heat transport, are of great interest [7]. The timescale of these processes coincides well with the dating range of ^{39}Ar. For instance, one cycle of the global conveyor belt takes about 2000 years [2].
Few instructive studies with ^{39}Ar have already been performed along the great conveyor belt. Results of such a study in the North-Atlantic at a depth of 4000-4500m are shown in fig. 1.3. Measured ^{39}Ar concentrations (denoted in percent modern) confirm the current notion of cold water that sinks in the North-Atlantic and flows to the south along the coast of America.
However, these measurements require quite some effort since the necessary sample size of several tons is far beyond the standard probe volumes (~10l) of research ships. Therefore only few oceanographic studies that include ^{39}Ar exist.

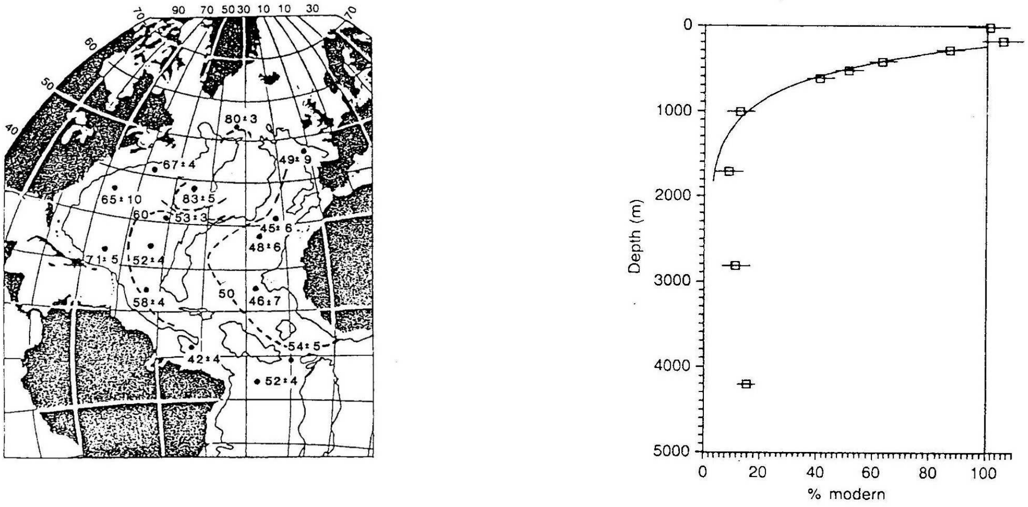

Figure 1.3.: ^{39}Ar-dating in oceans: ^{39}Ar-distribution in the Atlantic Ocean at depth 4000-4500m (left) and ^{39}Ar depth-profile in the North-Pacific (right) [7]

In another study, a depth-profile of ^{39}Ar has been measured in the GEOSECS station 347 in the pacific ocean (fig. 1.3 right). The measurements can be explained by diffusion from equilibrated surface waters down the water column as well as horizontal advection of deep water from the south.

In **ice** the ^{39}Ar in the enclosed air is actually measured, as the Argon eludes during the process of cristallization. A depth-profile of ^{39}Ar in an ice-sheet in greenland is shown in fig. 1.4 which agrees well with corresponding $\delta^{18}O$ measurements.

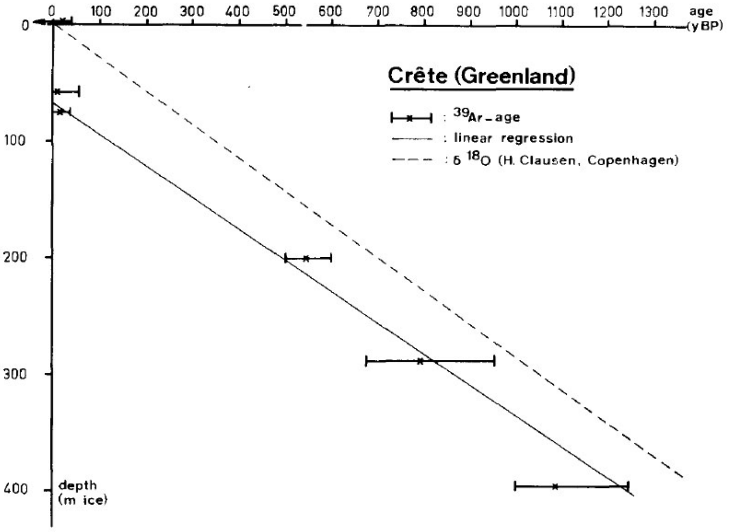

Figure 1.4.: ^{39}Ar-dating in ice from [7]

Furthermore, the depth at which the interconnecting voids are transformed into gas bubbles, that are entrapped in the ice, can clearly be seen at 70m depth. Dating with ^{39}Ar would be particularly interesting for alpine glaciers because their timescale lies well within its dating range [9].

For **groundwater** several studies have been carried out to gain information about the regional hydraulic structure, such as the recharge rate or flow velocity. Especially in multitracer studies, ^{39}Ar helps to determine the older fraction of the age distribution [11]. Fig. 1.5 shows an example of a groundwater study done with ^{39}Ar in comparison with ^{14}C.

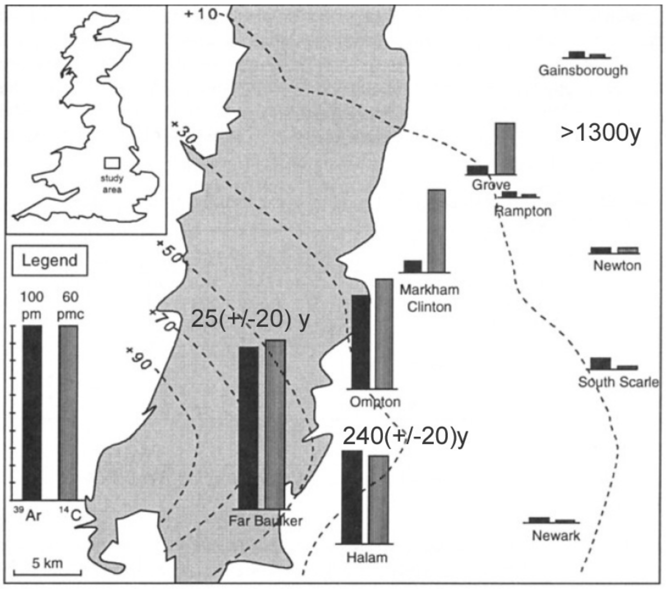
+10
+30
+50
+70
+90
study area
Legend
100 pm
60 pmc
39Ar
14C
5 km
Gainsborough
>1300y
Grove
Rampton
Newton
Markham Clinton
25(+/-20) y
Ompton
South Scarle
240(+/-20)y
Far Baulker
Halam
Newark

Figure 1.5.: ^{39}Ar-dating in the east Midlands Triassic sandstone aquifer (UK). Contours indicate the potentiometric surface and the shaded area denotes the outcrop of the sandstone aquifer [12] (pm=percent modern).

A decrease in ^{39}Ar concentration is visible when going from high to low hydraulic head identifying the aquifer outcrop as recharge area. Furthermore, note the direction of flow perpendicular to the isobaric surface.

Finally, dating with ^{39}Ar also allows for **climate reconstruction**. The temperature on the surface at the time when a water sample was in equilibirium with the atmosphere can be determined by exploiting the temperature dependence of noble gas solubilities (fig. 1.6). In order to obtain the time that corresponds to that temperature, the age of the water sample has to be determined. If the sample is between 50 and 1000 years old this can presently only be done with ^{39}Ar. Fig. 1.6 shows a temperature record over the last 500 years that has been reconstructed this way.

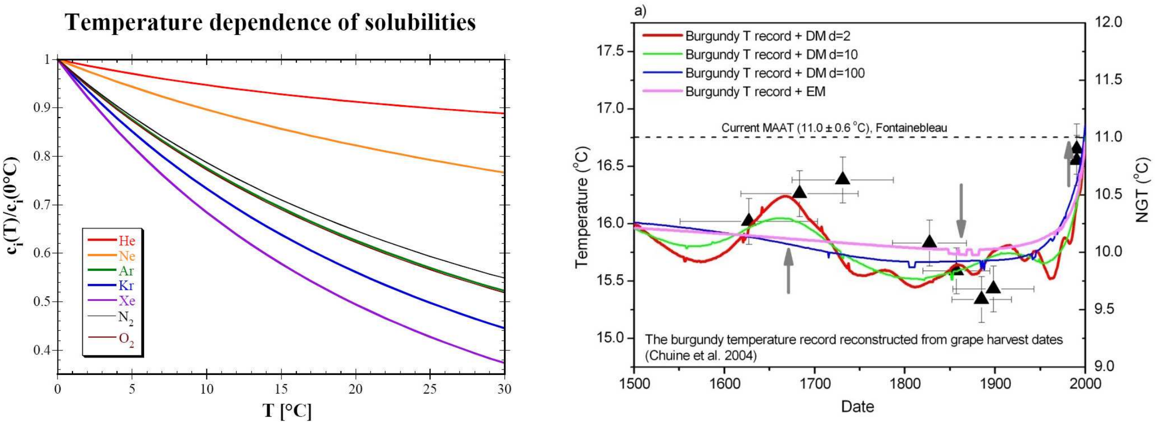

Figure 1.6.: Temperature reconstruction with atmospheric noble gases based on the temperature dependence of solubilities (left) [8]. On the right a ^{39}Ar-dated temperature record over the last 500 years obtained from a groundwater study in the Fontainebleau sands aquifer (France) is shown [13].

1.4. Methods for measuring ^{39}Ar

To measure the amount of ^{39}Ar one has to separate ^{39}Ar from all other Argon isotopes as well as to detect it on the single atom level. In principle, each feature that distinguishes ^{39}Ar from other Argon isotopes can be exploited for the separation. These differences are (see chapter 3)

- radioactivity
- mass
- energy levels
- nuclear spin

The first three are the basis of the methods, which will be presented in the following. For directly exploiting the nuclear spin one could think of some kind of NMR (Nuclear-Magnetic-Resonance)-spectroscopy or Stern-Gerlach setup, but nothing could be found in literature concerning this strategy.

1.4.1. Low-Level-Decay Counting (LLC)

One of the properties that distinguishes ^{39}Ar is its radioactivity[2]. Hence, once all Argon is extracted from a water sample, the amount of ^{39}Ar can be determined from the measurable activity of the ^{39}Ar(n,p)^{39}K reaction.

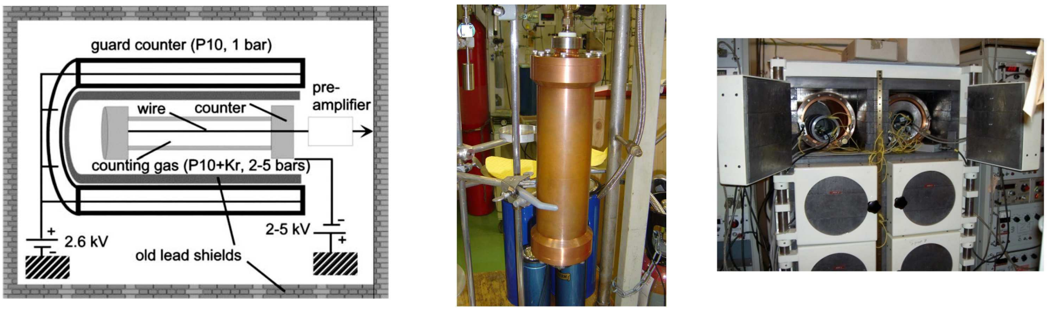

Figure 1.7.: Apparatus for measuring ^{39}Ar by Low-Level-Decay-Counting in Bern [14].

The modern activity for 1 m^3 air of ^{39}Ar is 1.65 Bq [7]. This can be translated into an activity of about 2 dis/h for 2000 litre of modern water, if one takes into account the separation- and counting-efficiency [12]. This leads to a counting time of more than a week to reach a relative error below 5%.
Furthermore, it is essential to eliminate all background activity. The only laboratory, that can measure ^{39}Ar by LLC is 35m underground, where the measurements are performed in big lead-chambers. So far almost all ^{39}Ar-measurements were carried out in this laboratory in Bern, Switzerland [14]. The major drawback of this method is the described need of huge sample sizes and long counting times. For groundwater studies, where usually big quantities are available and the degassing can be conducted in the field, this is not such a problem. However, it severely limits the application regarding oceanographic studies, where the standard sample sizes are far below the required quantities of several tons.

---

[2] All other radioactive Argon isotopes have a half-life of less than a month and are even much less abundant than ^{39}Ar (see chapter 3).

1.4.2. Accelerator Mass Spectrometry (AMS)

AMS uses the mass of ^{39}Ar to separate it from its isotopes. In contrast to ^{14}C, where AMS as a standard technique is even developed as a table-top device, ^{39}Ar poses severe difficulties to AMS, since it does not form negative ions. Therefore, positive-ion accelerators must be used, which requires a much more complicated setup. Fig. 1.8 shows the currently unique experimental setup for measuring ^{39}Ar [15].
In this experiment, $^{39}\text{Ar}^{8+}$ ions are produced in ECR II (electron-cyclotron-resonance)[3], accelerated by the Linac, separated from their isobar $^{39}\text{K}^{8+}$ in the gas-filled spectrograph and finally, detected using a position-sensitive Parallel Plate Avalanche Counter (PPAC), that is followed by an ionization chamber.
This way, modern Argon samples could be measured [16] and later also a field study with ocean water samples from the Southern Atlantic ventilation experiment has been performed [15]. Although AMS does not need big sample sizes or measuring times, it is very costly and requires a huge accelerator facility. Thus, a development as for ^{14}C is not likely.

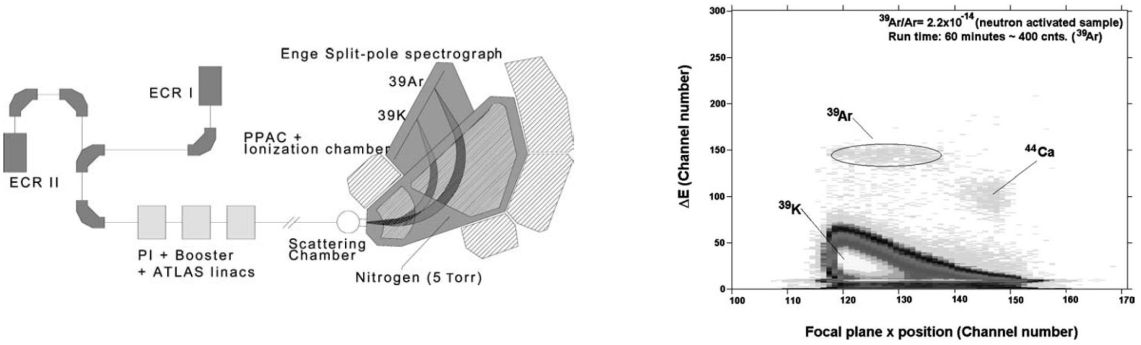

Figure 1.8.: Apparatus for measuring ^{39}Ar by AMS (left). Detector image from oceanic water sample (right). ^{39}Ar is clearly separated from its isobar ^{39}K [2].

1.4.3. Atom Trap Trace Analysis (ATTA)

This method was first realized at the Argonne National Laboratories for the rare Krypton isotopes ^{85}Kr and ^{81}Kr whose isotopic abundance is $\sim 10^{-11}$ and $\sim 10^{-12}$, respectively [3] and has also been applied to rare Calcium isotopes [5, 6]. So far, it has not been applied to ^{39}Ar, which is the endeavour of the experiment presented in this work. Before proceeding to the detailed functioning of ATTA, the prerequisitory theoretical background will be given and some necessary properties of Argon will be collected.

---

[3] ECR I delivers a calibration beam of $^{78}\text{Kr}^{16+}$ ions.

To conclude this chapter a comparison of the discussed methods applied to ^{81}Kr, ^{85}Kr and ^{39}Ar is given.

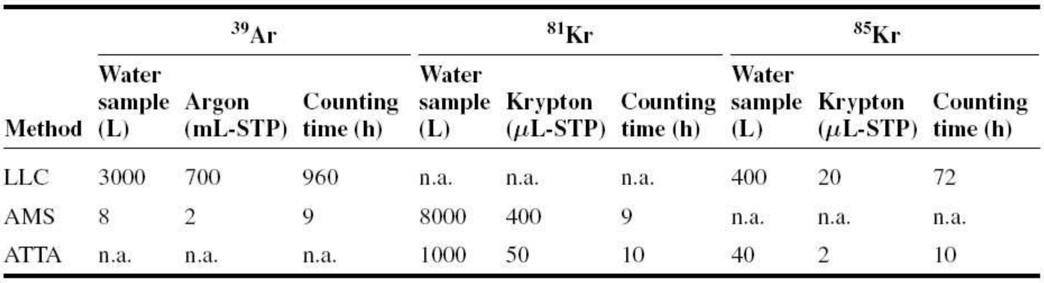

	^{39}**Ar**			^{81}**Kr**			^{85}**Kr**		
Method	**Water sample (L)**	**Argon (mL-STP)**	**Counting time (h)**	**Water sample (L)**	**Krypton (μL-STP)**	**Counting time (h)**	**Water sample (L)**	**Krypton (μL-STP)**	**Counting time (h)**
LLC	3000	700	960	n.a.	n.a.	n.a.	400	20	72
AMS	8	2	9	8000	400	9	n.a.	n.a.	n.a.
ATTA	n.a.	n.a.	n.a.	1000	50	10	40	2	10

Figure 1.9.: Comparison of LLC, AMS and ATTA for the rare isotopes ^{81}Kr, ^{85}Kr and ^{39}Ar [2]

For the rare Krypton isotopes ATTA is already better than LLC and AMS in terms of both sample size and counting time. To reach the same counting time as with ATTA for Krypton, ATTA for ^{39}Ar needs to be more efficient by a factor ~1000 since ^{39}Ar is less abundant than ^{81}Kr by that factor. Once this is achieved, there should not remain a problem of sample size, as there is ~5000 times more Argon in water than Krypton.

2. Principles of Laser Cooling and Trapping

The following chapter aims to provide the basic formulas and principles, that are necessary to understand the presented ATTA method. A detailed formal derivation can be found in e.g. [17, 18, 19, 20, 21].
The approach presented here mainly follows [17] and [21].

2.1. The scattering force for a two-level atom at rest

For simplicity, consider an atom that has only a ground $|g\rangle$ and an excited state $|e\rangle$. These are eigenstates of the atomic Hamiltonian $\mathcal{H}_0$, i.e.

$$\begin{aligned} \mathcal{H}_0 \, |e\rangle &= \hbar\omega_e \, |e\rangle \\ \mathcal{H}_0 \, |g\rangle &= \hbar\omega_g \, |g\rangle \end{aligned}$$

The atom shall now be illuminated with laser light of the angular frequency ω_l corresponding to a detuning $\delta = \omega_l - \omega$ with $\omega := \omega_e - \omega_g$ (see fig. 2.1).

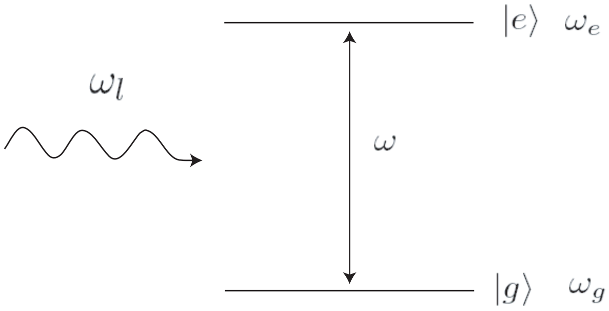

Figure 2.1.: idealized two-level atom

Assuming a classical light field, the time-evolution of the system can be described with the Schrödinger equation. However, including spontaneous emission requires to describe the system by the density matrix

$$\rho = \begin{pmatrix} \rho_{ee} & \rho_{eg} \\ \rho_{ge} & \rho_{gg} \end{pmatrix} \tag{2.1}$$

where ρ_{ee} and ρ_{gg} are the probabilities to find the system in state $|e\rangle$ and $|g\rangle$, respectively. The off-diagonals ρ_{eg} and ρ_{ge} determine the coherence between the two states.

The time evolution of the density and thereby the time evolution of the state populations is obtained by the von Neuman equation

$$i\hbar\dot{\rho} = [\mathcal{H}, \rho] \tag{2.2}$$

where $\mathcal{H} = \mathcal{H}_0 + \mathcal{H}'$ denotes the Hamilton operator which is composed of the atomic Hamiltonian $\mathcal{H}_0$ and the Hamiltonian $\mathcal{H}'$ that describes the atom–light interaction. In the dipole approximation this Hamiltonian can be expressed as

$$\mathcal{H}' = -\mathbf{d} \cdot \mathbf{E} \tag{2.3}$$

where $\mathbf{d}$ is the electric dipole operator and $\mathbf{E}$ the electric field produced by the laser at the location of the atom. Evaluating the differential equation (2.2) and introducing the Rabi-frequency

$$\Omega := \frac{\mathbf{d} \cdot \mathbf{E}}{\hbar} \tag{2.4}$$

yields the so-called Optical Bloch Equations (OBE)

$$\begin{array}{rcrcl}
\dot{\rho}_{gg} & = & \gamma\rho_{ee} & + & \frac{i}{2}\left(\Omega^*\tilde{\rho}_{eg} - \Omega\tilde{\rho}_{ge}\right) \\
\dot{\rho}_{ee} & = & -\gamma\rho_{ee} & + & \frac{i}{2}\left(\Omega\tilde{\rho}_{ge} - \Omega^*\tilde{\rho}_{eg}\right) \\
\dot{\tilde{\rho}}_{ge} & = & -\frac{\gamma}{2}\tilde{\rho}_{ge} & + & \frac{i}{2}\left[\Omega^*(\rho_{ee} - \rho_{gg}) - 2\delta\tilde{\rho}_{ge}\right] \\
\dot{\tilde{\rho}}_{eg} & = & -\frac{\gamma}{2}\tilde{\rho}_{eg} & + & \frac{i}{2}\left[\Omega(\rho_{gg} - \rho_{ee}) + 2\delta\tilde{\rho}_{eg}\right]
\end{array} \tag{2.5}$$

where the first summand has been added to account for spontaneous emission[1], that occurs at the spontaneous decay rate γ. Furthermore, $\tilde{\rho}_{ge} = \rho_{ge}e^{i\delta t}$ and $\tilde{\rho}_{eg} = \rho_{eg}e^{i\delta t}$ have been introduced and * denotes the complex conjugate.

The spontaneous decay rate γ is obtained from a fully quantized theory [17], where also the electromagnetic field is treated quantum mechanically.[2] It is given by

$$\gamma = \frac{\omega^3 e^2 d^2}{3\pi\epsilon_0\hbar c^3} \tag{2.6}$$

Using conservation of population

$$\rho_{gg} + \rho_{ee} = 1 \tag{2.7}$$

and optical coherence

$$\rho_{eg} = \rho_{ge}^* \tag{2.8}$$

these equations can further be reduced to

$$\begin{array}{rcl}
\dot{\rho}_{eg} & = & -\left(\frac{\gamma}{2} - i\delta\right)\rho_{eg} + \frac{i\omega\Omega}{2} \\
\dot{w} & = & -\gamma w - i\left(\Omega\rho_{eg}^* - \Omega^*\rho_{eg}\right) + \gamma
\end{array}$$

where $w := \rho_{gg} - \rho_{ee}$ denotes the difference in population.

---

[1] this is indeed a somewhat sloppy way of introducing the spontaneous emission. However, a more rigourous derivation [22] leads to the same result [17], but would exceed the scope of this work.

[2] The correct expression for the spontaneous decay rate was already found by a phenomenological theory of Einstein [17].

The temporal behaviour of the system can be found by direct numerical integration of the optical Bloch equations. The result for different detunings and Rabi-frequencies is shown in figure 2.2.

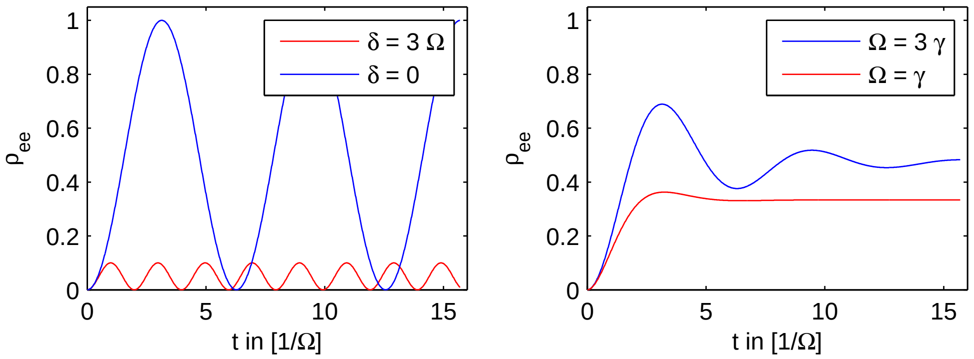

Figure 2.2.: Rabi oscillations for different detunings without spontaneous emission (left) and including spontaneous emission (right) for different Rabi-frequencies

Without spontaneous emission (i.e. $\gamma = 0$) the two-level system performs oscillations between the ground and the excited state. In case of resonance ($\delta = 0$) these oscillations are fully modulated and occur at the Rabi-frequency Ω, whereas for $\delta \neq 0$ the modulation of the oscillations decreases and the frequency increases to

$$\Omega' = \sqrt{\delta^2 + \Omega^2} \tag{2.9}$$

If spontaneous emission is included (i.e. $\gamma \neq 0$) one can distinguish between two different time domains:

- For $t \ll \frac{1}{\gamma}$ the damping caused by spontaneous emission is negligable.
- For $t \gg \frac{1}{\gamma}$ a steady-state will be reached due to damping caused by spontaneous emission.

The steady-state population of the excited state ρ_{ee} in the second case can be obtained by demanding

$$\dot{\rho}_{eg} = \dot{w} = 0 \tag{2.10}$$

which yields

$$\rho_{ee} = \frac{s/2}{1 + s + \frac{4\delta^2}{\gamma^2}} \tag{2.11}$$

where the saturation parameter

$$s := \frac{2\Omega^2}{\gamma^2} = \frac{2|\mathbf{d}|^2|\mathbf{E}|^2}{\hbar\gamma^2} = \frac{I}{I_s} \tag{2.12}$$

has been defined. Furthermore, the saturation intensity

$$I_s := \frac{\hbar c \epsilon_0 \gamma^2}{4d^2} \overset{(2.6)}{=} \frac{\pi h c \gamma}{3\lambda^3} \tag{2.13}$$

is introduced, while using that the intensity of the light field is related to the electric field via

$$I = \frac{1}{2}\epsilon_0 c|\mathbf{E}|^2 \tag{2.14}$$

For the case of low saturation with $s \ll 1$, the population is predominantly in the ground state, whereas in the case of high saturation, the population is equally distributed between ground and excited state.
From (2.11) the total scattering rate γ_s of light from the laser field is given by

$$\gamma_s = \gamma\rho_{ee} = \frac{\gamma}{2}\frac{s}{1+s+\frac{4\delta^2}{\gamma^2}} \tag{2.15}$$

which saturates for large s to the maximum scattering rate $\gamma/2$.
Plotting the scattering rate as a function of detuning δ (fig. 2.3) yields a Lorentzian-profile with a FWHM of

$$\gamma' = \gamma\sqrt{1+s} \tag{2.16}$$

This is referred to as the power-broadened linewidth.

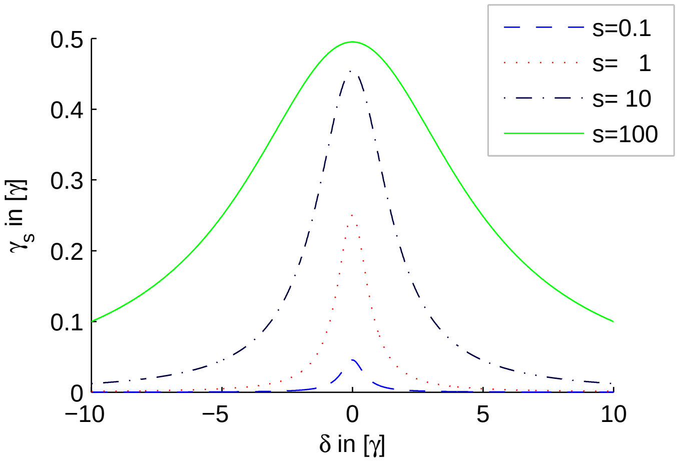

Figure 2.3.: The Scattering rate γ_s as a function of detuning δ for different saturation parameter s is shown. For $s > 1$ the line profiles are substantially broadened.

The nature of spontaneous emission now implies a force of the laser light exerted on a two-level atom. Absorption of light leads to a transfer of momentum from the laser beam to the atom. If the atom decays by spontaneous emission, the associated recoil is in a random direction, hence, the average over many of these recoils is zero. Thus, the force $\mathbf{F_s}$ from absorption in the direction of the laser beam with wavevector $\mathbf{k}$ writes

$$\mathbf{F_s} = \hbar\mathbf{k}\gamma_s = \hbar\mathbf{k}\frac{\gamma}{2}\frac{s}{1+s+\frac{4\delta^2}{\gamma^2}} \tag{2.17}$$

This force provides the basis for all cooling methods that are employed in this experiment and briefly described in the following subsections.

2.2. Optical Molasses

Two counterpropagating laser beams with the wavevectors $\pm\mathbf{k}$ that are red-detuned with respect to the atomic transition frequency exert the forces $\mathbf{F}_\pm$ on an atom with velocity $\mathbf{v}$. Accounting for the Doppler-shift

$$\Delta\omega_D = -\mathbf{k}\cdot\mathbf{v} \tag{2.18}$$

these forces write

$$\mathbf{F}_\pm = \pm\hbar\mathbf{k}\frac{\gamma}{2}\frac{s}{1+s+\frac{4(\delta\mp\mathbf{k}\cdot\mathbf{v})^2}{\gamma^2}} \tag{2.19}$$

In the case of low intensity, the resulting force $\mathbf{F}_{\mathrm{OM}}$ can be expressed as

$$\mathbf{F}_{\mathbf{OM}} = \mathbf{F}_+ + \mathbf{F}_- \overset{v<\gamma/k}{\propto} -\mathbf{v} \tag{2.20}$$

i.e. for small velocities the force is proportional to the velocity $\mathbf{v}$ (fig. 2.4). This causes the atomic velocity along the axis of the beams to be viscously damped. Therefore, such a setup is called Optical Molasses (OM) and sometimes referred to as Doppler cooling.

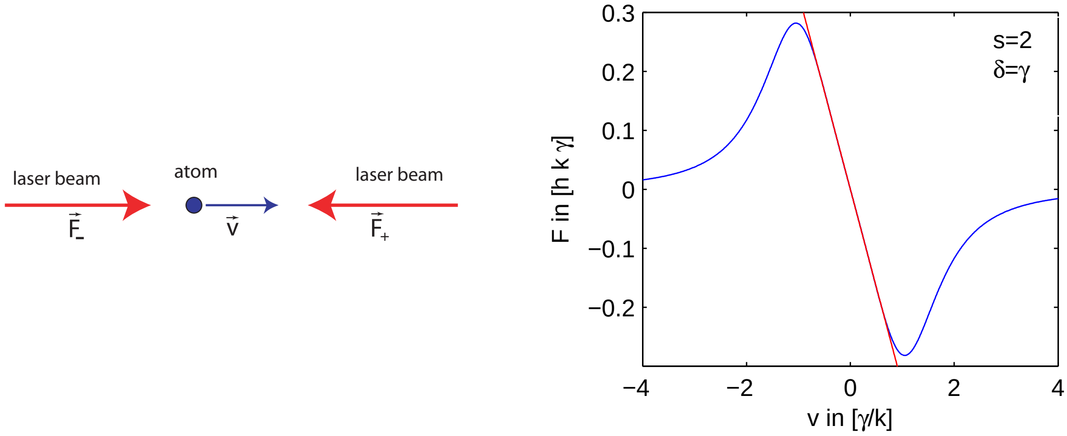

Figure 2.4.: Scheme of Optical Molasses (OM) in one dimension (left) and the resulting force dependent on the atomic velocity (right).

2.3. Zeeman slowing

Optical Molasses only work for small velocities. If one wants to decelerate atoms of thermal velocity, they will not stay in resonance as their velocity and consequently the Doppler-shift changes. Thus, one has to compensate for the changing Doppler-shift during the entire cooling process. Assuming for the moment that this is the case — regardless of how to realize it — the maximum acceleration is given by

$$a_{max} := \frac{F_{max}}{m} = \frac{\hbar k}{m}\frac{\gamma}{2} \tag{2.21}$$

With an initial velocity v_0 this leads to a required cooling distance of

$$L_{cool} = \frac{v_0^2}{2a_{max}} \tag{2.22}$$

The resulting velocity $v(z)$ as a function of the axial position z writes

$$v(z) = v_0 \cdot \sqrt{1 - \frac{z}{L_{cool}}}\,) \tag{2.23}$$

E.g. for Argon atoms with $v_0 = 400\,\mathrm{m/s}$ this translates to a cooling distance of about 40 cm. Note that this is the minimum value, that assumes the atoms to remain in resonance at all times and maximal saturation.

However, the question of how to realize the resonance condition persists. One of the standard solutions to that problem exploits the shift in the atomic resonance frequency caused by a magnetic field of strength B, called Zeeman-shift

$$\Delta\omega_z = -\frac{\mu}{\hbar} \cdot B = -m \cdot \frac{\mu_B g}{\hbar} B \tag{2.24}$$

where μ denotes the magnetic moment of the atom, m the magnetic quantum number, μ_B the Bohr magneton and g the Landé-Faktor. Fig. 2.5 illustrates the Zeeman-shift for the simple case of a non-degenerate ground state and an excited level with three magnetic substates.

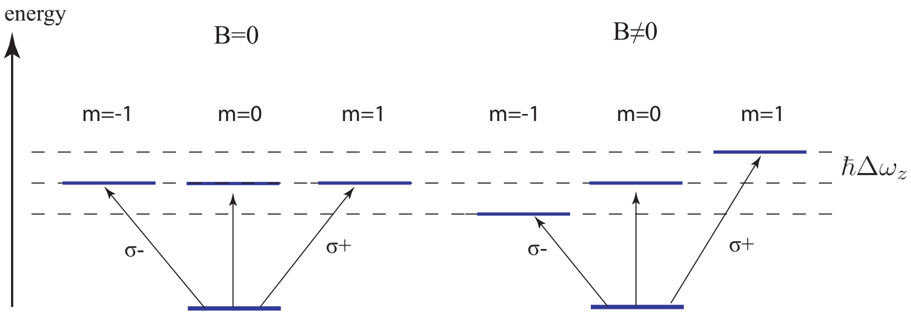

Figure 2.5.: Zeeman Splitting due to a magnetic field

Transitions with $\Delta m = \pm 1$ can be induced by circularly polarized light while the $\Delta m = 0$ transitions are driven by linearly polarized light.

Note that depending on the polarity of the applied magnetic field, the polarization of the laser beam has to be chosen accordingly.
If the magnetic field $B(z)$ is designed along the beam axis z such that the resonance condition

$$\Delta\omega_D(z) \overset{!}{=} \Delta\omega_Z(z) \tag{2.25}$$

is fulfilled for the entire cooling distance, (2.23) yields

$$B(z) = B_0\sqrt{1 - \frac{z}{L_{cool}}} \tag{2.26}$$

This magnetic field is usually realized by a solenoid, whose number of windings increases proportional to $B(z)$ (fig. 2.6).

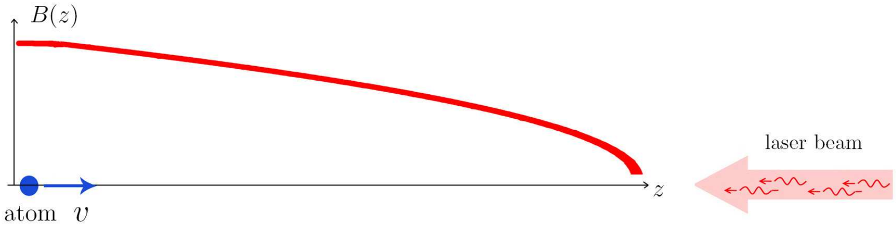

Figure 2.6.: Illustration of the idea of Zeeman slowing.

2.4. Magneto-Optical-Trap (MOT)

From the discussion of the 1D-optical molasses one might be tempted to extent this scheme to three dimensions in order to trap atoms at a certain point. Unfortunately, the force from Optical-Molasses is only velocity and not position dependent. Due to their remaining velocies, the atoms would diffuse out of the trapping region. Hence, in order to trap the atoms a position-dependent force is required in addition. This can again be realized with a magnetic field. In one dimension the trapping scheme would look as sketched in fig. 2.7. The counterpropagating beams need to have σ^+ and σ^- polarization due to the different Zeeman sublevels that are addressed. Extended to three dimensions a MOT can be realized with the setup shown in fig. 2.8. The magnetic field is typically provided by a pair of Anti-Helmholtz coils.

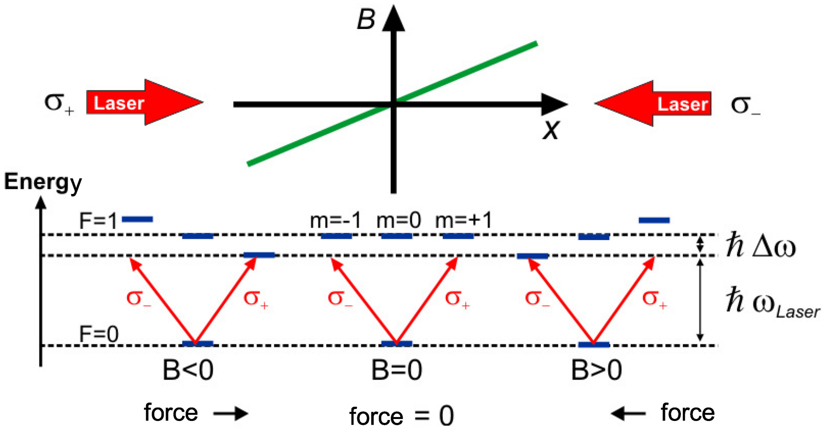

Figure 2.7.: The position-dependent force in a Magneto-Optical-Trap induced by a magnetic field is illustrated

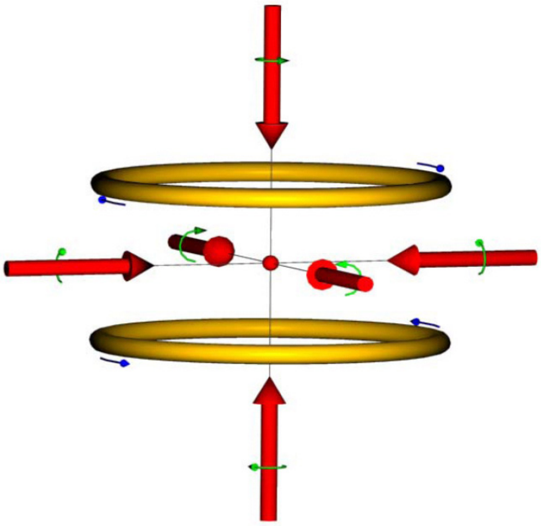

Figure 2.8.: Magneto-Optical-Trap in three dimensions

2.5. Doppler cooling limit

The foregoing sections might suggest that an arbitrary low final velocity can be reached by laser cooling, which naturally is not true. When the scattering force was derived it has been averaged over many photon recoils $\hbar k$. Related to these changes in atomic momentum is an average change in kinetic energy of at least the recoil energy

$$E_r = \frac{\hbar^2 k^2}{2m} = \hbar \omega_r \tag{2.27}$$

Hence the average angular frequency of each absorption is $\omega_{abs} = \omega + \omega_r$ while the average angular frequency of each emission is $\omega_{em} = \omega - \omega_r$. Thus the light field loses an average energy of

$$\hbar(\omega_{abs} - \omega_{em}) = 2\hbar\omega_r \tag{2.28}$$

for each scattering. In case of one-dimensional molasses this occurs at a rate $2\gamma_s$, for there are two beams. The atoms are thereby heated, since these recoils are in random direction.

The competition between this heating and the cooling due to the molasses results in a nonzero steady state kinetic energy. This happens when the cooling rate equals the heating rate

$$\mathbf{F_{OM}} \cdot \mathbf{v} = 4\hbar\omega_r\gamma_s \tag{2.29}$$

which yields the steady-state velocity

$$v_D = \sqrt{\frac{\hbar\gamma}{4m}\left(\frac{2|\delta|}{\gamma} + \frac{\gamma}{2|\delta|}\right)} \tag{2.30}$$

which is minimal for

$$\delta = -\gamma/2 \tag{2.31}$$

Therefore a detuning of $\delta = -\gamma/2$ is often desired when applying laser cooling. For argon this minimal velocity spread is

$$v_D \approx 0.12 \text{ m/s} \tag{2.32}$$

For higher saturation values in (2.30) the natural linewidth γ can be replaced by the power broadened linewidth (2.16) provided that the detuning is large enough, so that the saturation parameter is small around the null velocity [23]. In that case the Doppler velocity writes

$$v_D = \sqrt{\frac{\hbar\gamma'}{4m}\left(\frac{2|\delta|}{\gamma'} + \frac{\gamma'}{2|\delta|}\right)} \tag{2.33}$$

3. Properties of Argon

Argon is the most abundant noble gas in the atmosphere with almost 1 % [24]. It is inert under most conditions and forms no confirmed stable compounds at room temperature. Therefore, it is industrially used as a shielding gas for welding and other applications that require a cheap inert gas.
With atomic number 18 its closest isotopes are [25, 26]

isotope	isotopic ratio	half life $T_{1/2}$
^{40}Ar	99.6	stable
^{36}Ar	0.33	stable
^{38}Ar	0.06	stable
^{39}Ar	$8.5 \cdot 10^{-16}$	269a
^{37}Ar	–	35d
^{42}Ar	–	33a
^{41}Ar	$< 6 \cdot 10^{-21}$	1.8h

All isotopes with even number of nucleons do not have a nuclear spin whereas the ones with odd number of nucleons do. In the following only the two isotopes ^{40}Ar and ^{39}Ar, that are relevant for ATTA, are discussed.

3.1. Argon 40

^{40}Ar is the most abundant argon isotope and does not show hyperfine structure, which makes laser cooling convenient compared to other elements.
Like all noble gases (except for Helium) its groundstate configuration is $n_g s^2 p^6$, where n_g denotes the main quantum number of the groundstate. The 6 p-electrons form a closed shell, therefore the ionization energy is very high. All excited states of noble gases are in a small energy range beneath the ionization border. Thus, the corresponding transition wavelength is in the VUV (Vacuum Ultra Violet) region. Upon excitation, an electron from the groundstate configuration is shifted to an excited state $n_e l$ with the main quantum number of the excited state $n_e > n_g$ and $l = s, p, d, f, ...$ Due to the small binding energy of the excited electron with respect to the others it has a large distance from the nucleus. Therefore, the energy-shift due to the LS-coupling among the body-electrons exceeds the Coulomb-interaction with the excited electron. This leads to the so-called Racah-coupling.
To describe this coupling, the body of the excited noble gas atom is determined by the quantum numbers n_g, L and S where L and S are the angular momentum and spin of the body electrons, respectively. L and S couple to the total angular momentum

$j = L + S$ of the body. The angular momentum l of the excited electron now couples with the latter via $K = j + l$ and finally, the spin s of the excited electron couples to $J = K + s$.
Hence, the electronic state of the excited noble gas atoms is completely described by the following set of quantum numbers

$$n_g, n_e, L, S, j, l, K, s, J \tag{3.1}$$

and is usually denoted by

$$(n_g p^5)^{2s+1} L_j n_e l [K]_J \tag{3.2}$$

The selection rule writes

$$\Delta J = 0, \pm 1 \tag{3.3}$$

As this notation scheme is rather confusing it is usually simplified in the so-called Paschen-Notation:

- All states with the same (n_e, l) are grouped together.
- All other quantum numbers (S, L, j, K, s, J) are replaced by an index q, which corresponds to the energy.
- The total angular momentum J is put in brackets.

The Paschen-Notation writes

$$n_e l_q(J) \tag{3.4}$$

and will be used exclusively throughout this work.
Fig. 3.1 shows a simplified level scheme of ^{40}Ar together with the relevant transitions[1].

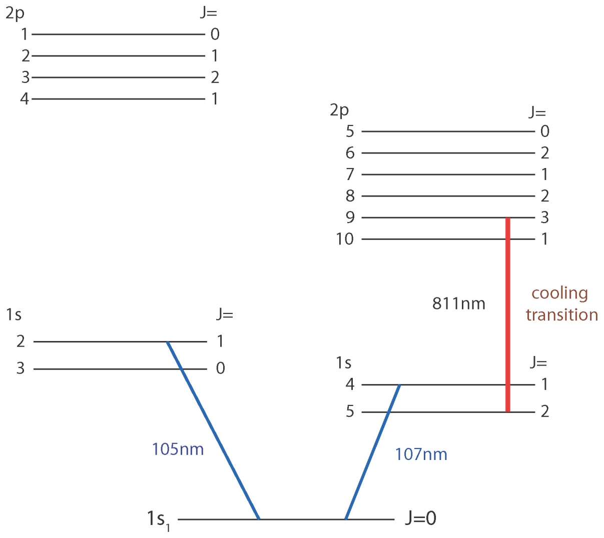

Figure 3.1.: Simplified level scheme of ^{40}Ar

---

[1] A detailed level scheme can be found in Appendix A.

As for almost all noble gases, the transitions from the ground state are in the VUV-regime with a wavelength of 105 nm and 107 nm, which is far below what current commercial lasers can achieve. Hence, laser cooling from the ground state cannot be accomplished. Fortunately, there are two metastable levels with the lifetimes of 45 s ($1s_3$) and 38 s ($1s_5$). This timescale is much longer than cooling processes (typically less than a second).

From the metastable $1s_5(J = 2)$ level there is a closed transition to the $2p_9(J = 3)$ since the selection rule $\Delta J = 0, \pm 1$ does not allow any other decay from the $2p_9(J = 3)$ than the one back to the $1s_5(J = 2)$ level. This transition occurs in the near infrared at a wavelength of 811.754 nm for which commercial lasers are readily available. This is the cooling transition that will always be referred to in the following.

The energy levels of the cooling transition, $1s_5(J = 2)$ and $2p_9(J = 3)$, further split into $2J + 1$ magnetic substates, which are degenerate in absence of a magnetic field (fig. 3.2). The squared Clebsch-Gordan-coefficients represent the coupling among the magnetic substates.

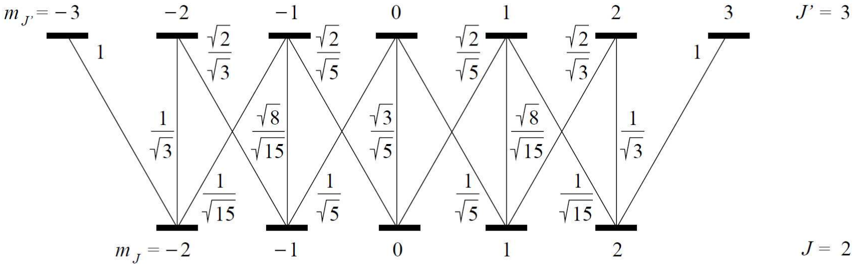

Figure 3.2.: Magnetic substates of the $1s_5(J = 2)$ and the $2p_9(J = 3)$ level with corresponding Clebsch-Gordan-coefficients [27]

Thus, a two-level system can only be realized by σ^+ or σ^- light, driving the closed outer $m_J = \pm 2 \leftrightarrow m_J = \pm 3$ transition, respectively. If the atoms are not polarized, i.e. if no well defined magnetic field is applied, the distribution among the substates has to be included. Usually, this results in a correction for the saturation intensity. In [27] for example an effective Clebsch-Gordan Coefficient $C_{eff} = 0.48$ has been calculated as a scaling parameter for the intensities. However, it has been chosen to experimentally determine the saturation intensity by using the power dependence of the linewidth as described in Chapter two, where the power-broadened linewidth was

$$\gamma' = \gamma \sqrt{1 + \frac{I}{I_s}}$$

The influence of changing polarizations in a setup where there is no defined magnetic field can thereby also be investigated. These measurements have not been accomplished yet, but might later be found in [28]. For the time being, the uncorrected saturation intensity is used.

3.2. Argon 39

As ^{39}Ar has a nuclear momentum ($I = 7/2$), its level scheme is more complicated than the one of ^{40}Ar due to hyperfine splitting. For simplicity, only the relevant $1s_5(J = 2) \leftrightarrow 2p_9(J = 3)$ transition shall be considered. The $J = 2$ state is split into five hyperfine levels with

$$F = |I - J| = 3/2 \; ... \; |I + J| = 11/2 \tag{3.5}$$

whereas the $J = 3$ state splits into seven hyperfine levels, accordingly[2] (fig. 3.3). Thus, the question arises which transition is now the most suitable for cooling.

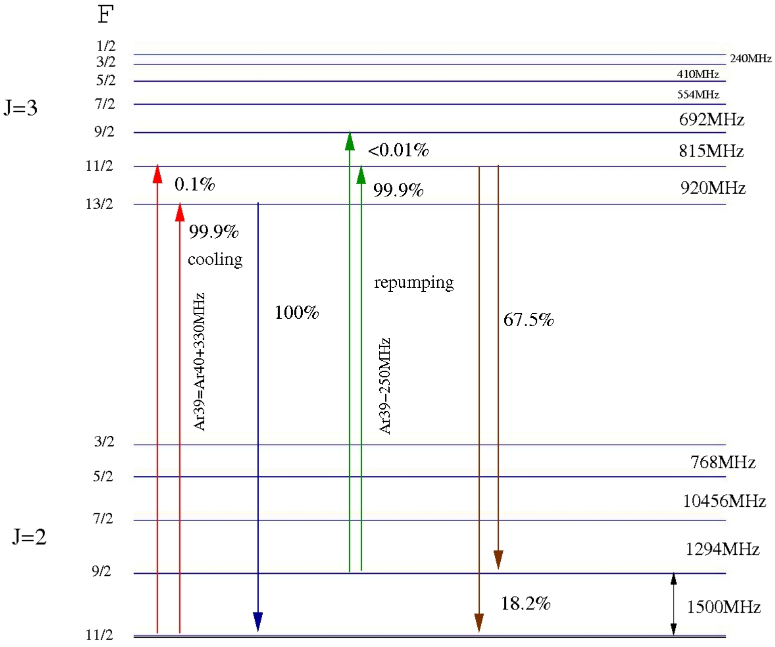
F
J=3
1/2
3/2
5/2
7/2
9/2
11/2
13/2
240MHz
410MHz
554MHz
692MHz
815MHz
920MHz
<0.01%
0.1%
99.9%
99.9%
cooling
repumping
100%
67.5%
Ar39=Ar40+330MHz
Ar39−250MHz
J=2
3/2
5/2
7/2
9/2
11/2
768MHz
10456MHz
1294MHz
18.2%
1500MHz

Figure 3.3.: Transition scheme of ^{39}Ar with cooling and pumping transitions. Due to off-resonant excitation some $F_2 = 11/2$ atoms are excited to the non-desired $F_3 = 11/2$ state. The intensity of the repumper has to be chosen, such that only very little atoms are transferred to $F_3 = 9/2$. All frequencies are denoted with respects to ^{40}Ar.

According to the selection rule

$$\Delta F = 0, \pm 1 \tag{3.6}$$

the transition from[3] $F_2(11/2)$ to $F_3(13/2)$ is the most suitable one for cooling and trapping ^{39}Ar, since from the latter state the atoms can only deexcite to the inital $F_2(11/2)$. In principle, this is a closed transition, but due to off-resonant excitation enhanced by power-broadening, some atoms will be shifted to the $F_3(11/2)$ state. From there they will most probably deexcite to the $F_2(9/2)$ state and thus, they will be lost.

---

[2] The spectroscopy data has only recently been measured [29].

[3] The subscipt denotes the total angular momentum J.

Recognizing that more than a hundred thousand photons may be scattered, eventually this would be the fate of all atoms. Therefore a repumper is essential, such that the atoms are shifted to the $F_3(11/2)$ state, from where they will finally decay back to the $F_2(11/2)$ state.

Assuming that all ^{39}Ar atoms are equally distributed over the $J = 2$ hyperfine levels only $2/5$ would be susceptible to laser manipulations using only one repumper. This number could further be enhanced by a second repumper, that is resonant with the $F_2(7/2) \rightarrow F_3(9/2)$ transition. One could also try to initially shift all atoms to the $F_2(11/2)$ state by feeding all possible transitions $F_2 \rightarrow (F+1)_3$.

The $F_2(11/2)$ and the $F_3(13/2)$ level further split into $2F+1$ magnetic substates as indicated in fig. 3.4.

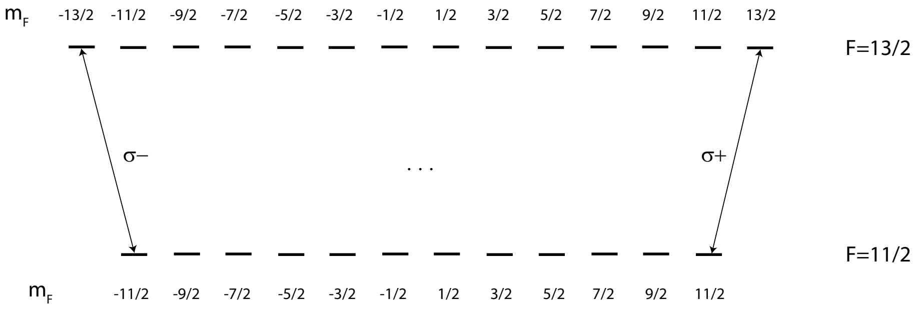
m_F
-13/2
-11/2
-9/2
-7/2
-5/2
-3/2
-1/2
1/2
3/2
5/2
7/2
9/2
11/2
13/2
F=13/2
σ−
. . .
σ+
F=11/2
m_F
-11/2
-9/2
-7/2
-5/2
-3/2
-1/2
1/2
3/2
5/2
7/2
9/2
11/2

Figure 3.4.: Magnetic substates of the $F_2(11/2)$ and $F_3(13/2)$ levels of ^{39}Ar.

This vast amount of substates has to be taken into account, especially when pumping processes among the substates are critical as is the case in the Zeeman-slower or the MOT. Since the two hyperfine levels have different Landé-factors, over many m_F the difference in frequency can be quite big, such that not all substates may be pumped efficiently.

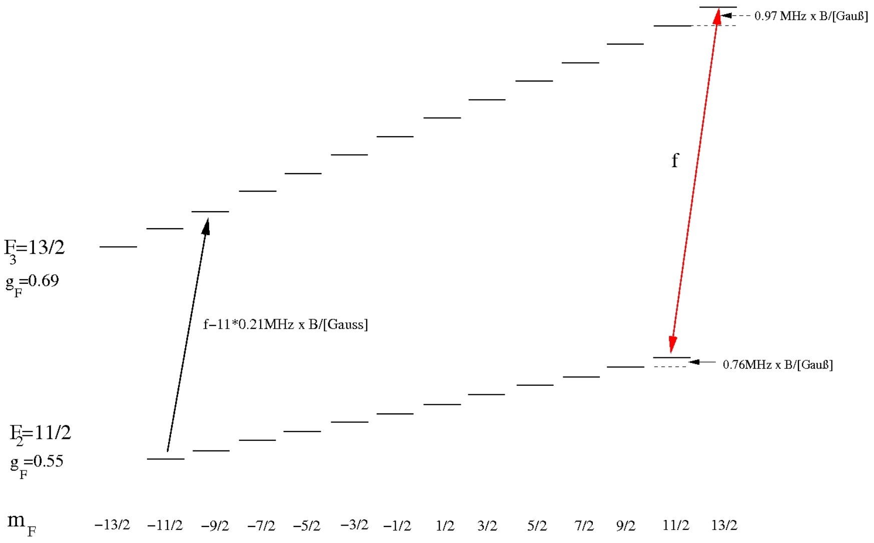
0.97 MHz x B/[Gauß]
f
F_3=13/2
g_F=0.69
f−11*0.21MHz x B/[Gauss]
0.76MHz x B/[Gauß]
F_2=11/2
g_F=0.55
m_F
−13/2
−11/2
−9/2
−7/2
−5/2
−3/2
−1/2
1/2
3/2
5/2
7/2
9/2
11/2
13/2

Figure 3.5.: Splitting of the magnetic substates in a magnetic field.

4. Atom Trap Trace Analysis of ^{39}Ar

After all prerequisites for the ATTA method have been gathered, it is time to proceed to its working principle as well as its experimental realization. As mentioned in the first Chapter, ATTA has been used for rare isotopes of Krypton and Calcium but not yet for ^{39}Ar.
In the following, the launched experimental realization of ATTA for ^{39}Ar will be presented. After describing its basic principle, the experimental setup will be discussed in detail.

4.1. Principle of ATTA

Since the isotopic abundance of ^{39}Ar is so tiny, detection on the single atom level is necessary. As described in chapter two, it is possible to trap atoms in a certain region using a Magneto-Optical Trap (MOT). Usually, this is done with a large number of atoms, but it is also feasible for just one single atom. If an atom is caught in the MOT, it may stay there for several hundred milliseconds. In the meantime it constantly absorbs and emits photons from the laser beams that confine the atom in the trapping region. This fluorescence from the single atom can be detected with a highly sensitive photon-detector and an imaging system that eliminates background light.
Such a system has already been realized for ^{40}Ar by [30] using a setup that is shown in fig. 4.1.

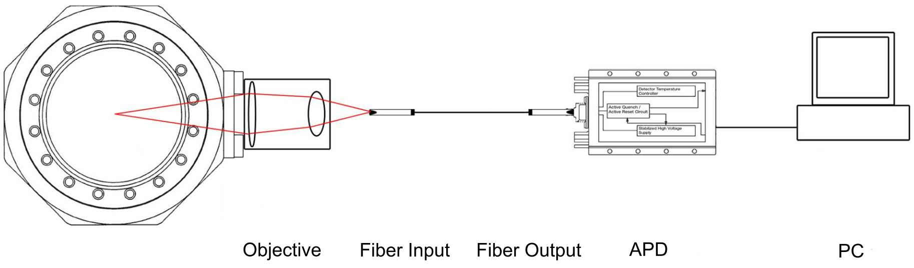
Detector Temperature Controller
Active Quench / Active Reset Circuit
Stabilized High Voltage Supply
Objective
Fiber Input
Fiber Output
APD
PC

Figure 4.1.: Single atom detection from fluorescence [30]

A 1:1 image of the trapping region is focused onto an optical fibre with a 70 μm core, that is connected to an avalanche photodiode (APD), which is read out by the computer.

The fluorescence signals obtained from this setup are presented in fig. 4.2. They show distinct one-atom events, two-atom events and so on.

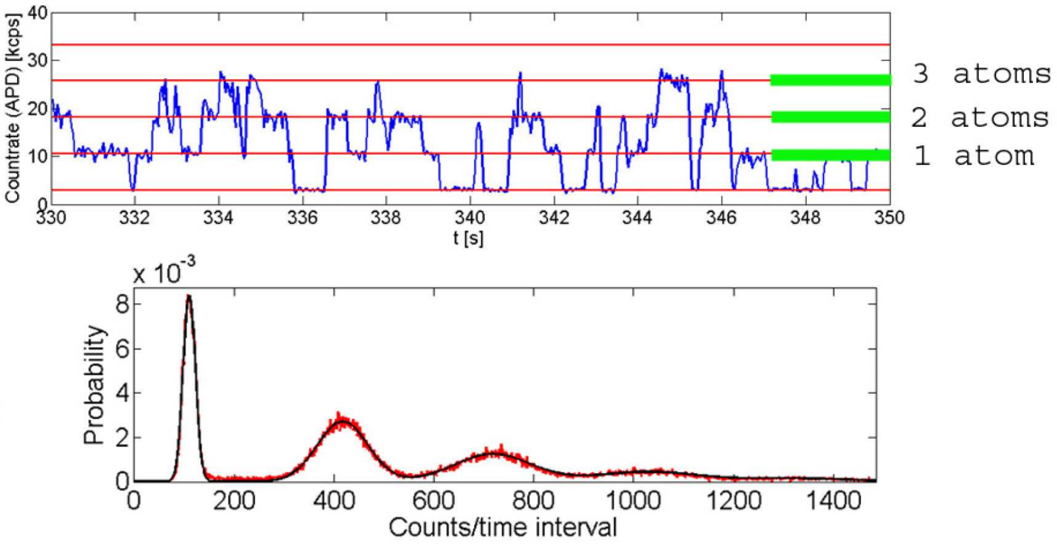

Figure 4.2.: Single atom detection from fluorescence. The upper graph shows the photon count rate of the avalanche photodiode. The height of the red horizontal bars correponds to the number of Argon atoms in the MOT. A histogramm over the countrate axis yields the graph below [30].

To be able to capture Argon atoms in the MOT an atomic beam needs to be prepared, such that its atoms have a velocity below the capture velocity of the MOT ($\sim$30 m/s). This is done as sketched in fig. 4.3. In the first stage Argon atoms are excited to the metastable $1s_5$ state. Subsequently, the atoms are susceptible to laser manipulation.

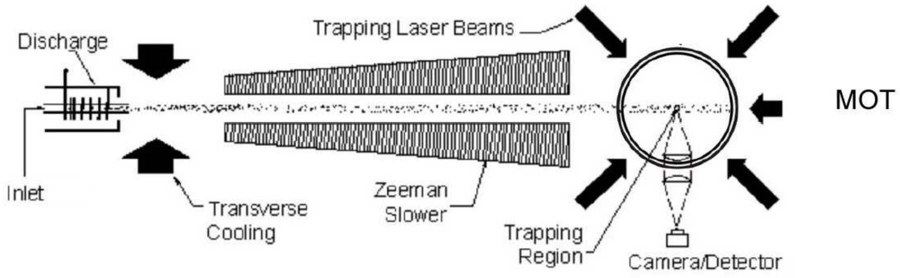

Figure 4.3.: Scheme of the ATTA-setup

The diverging metastable atom beam is thereafter collimated by transverse laser cooling. This cooling stage is followed by the one of the Zeeman-slower, which decreases the mean velocity of the atoms down to the capture velocity of the MOT. This way, a MOT can be used to detect single ^{39}Ar atoms.
However, the question of seperating ^{39}Ar from ^{40}Ar remains.
Recalling the scattering rate (2.15) one can estimate the relative photon scattering rate. Assuming that the laser is resonant with ^{39}Ar while its detuning relative to ^{40}Ar

is $\delta = 2\pi \cdot 494\,\mathrm{MHz}$ ([29]) yields

$$\frac{\gamma_s(^{39}\mathrm{Ar})}{\gamma_s(^{40}\mathrm{Ar})} = \frac{1 + s + \frac{4\delta^2}{\gamma^2}}{1+s} \overset{s\ll 1}{\approx} \frac{4\delta^2}{\gamma^2} \approx 27.000$$

This means that fluorescence from ^{40}Ar in the MOT and similarly the overall laser cooling of ^{40}Ar is strongly suppressed and reveals how ATTA seperates the two isotopes from each other.
Although the scattering of light by ^{40}Ar is much lower, this isotope is still $\sim 10^{15}$ times more abundant then ^{39}Ar. This might compensate for the small scattering rate and the fluorescence signal from ^{39}Ar would disappear in the ^{40}Ar background. That is why in the ATTA setup for rare Calcium isotopes in [6] an additional deflection stage behind the Zeeman-slower is used. If the ^{40}Ar-background results to be a problem in our setup, we would integrate this deflection stage by tilting the source, as indicated in fig. 4.5.

4.2. Experimental setup

Fig. 4.4 shows a technical drawing of the complete apparatus in comparison to the current state in the laboratory (picture on the left). On the left hand side of the apparatus, the sample can be attached to the big vacuum chamber, that bears a 2000 l/s turbo pump on its top. Through the side window the collimator can be seen followed by an intermediate differential pumping chamber that allows to implement beam diagnostics, additional transversal cooling or a mass spectrometer. This chamber is pumped by a 250 l/s turbo pump. The attached Zeeman-slower tube then leads to the MOT chamber which is also pumped by a 250 l/s turbo pump.

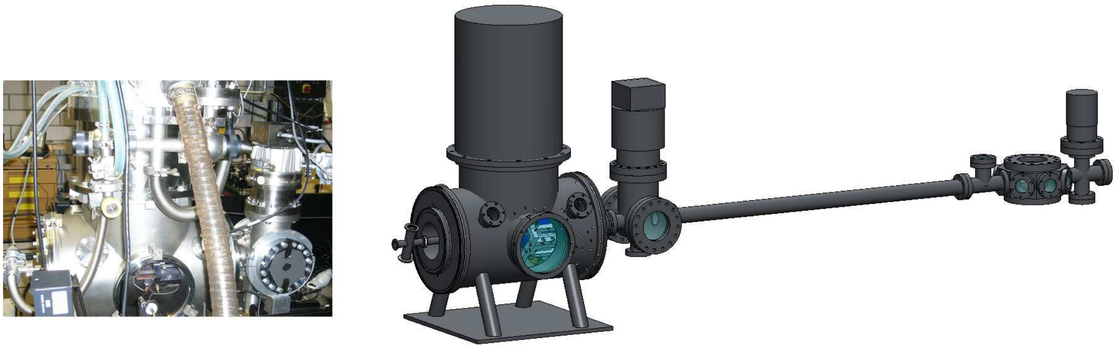

Figure 4.4.: Technical drawing of the entire apparatus (right) and the current state (left)

If all the atoms that pass the MOT chamber were pumped away, the pressure in the source chamber, and thereby the atomic flow, would deteriorate as soon as the sample is exhausted. Consequently, the counting signal would also decrease till vanishing entirely. Therefore, the vacuum setup is connected in recirculation mode as indicated in fig. 4.5. Atoms pumped off from each chamber are guided back to the source chamber. This way, the measurement could in principle last forever without exhausting the sample.

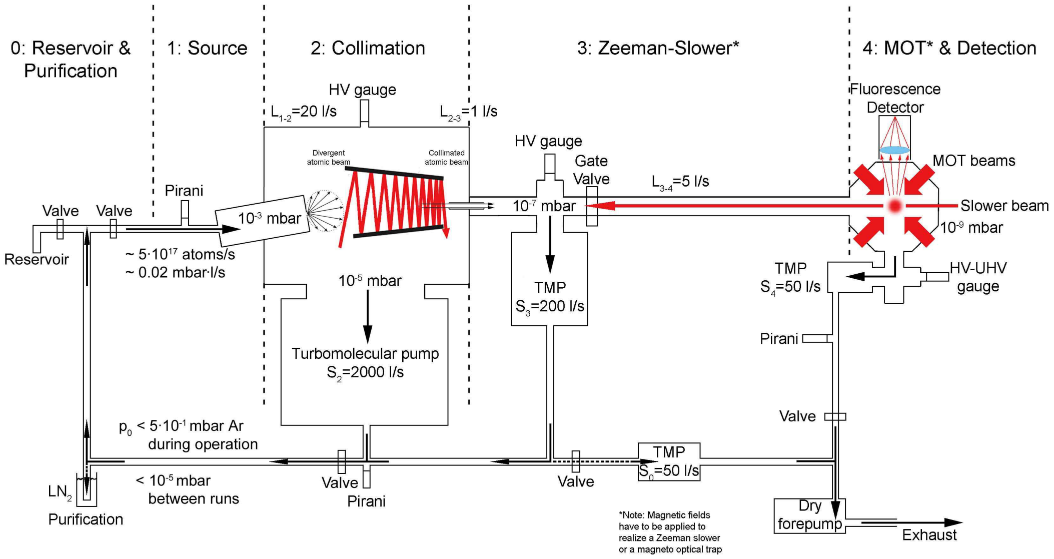
0: Reservoir & Purification
1: Source
2: Collimation
3: Zeeman-Slower*
4: MOT* & Detection
HV gauge
$L_{1\text{-}2}$=20 l/s
$L_{2\text{-}3}$=1 l/s
Divergent atomic beam
Collimated atomic beam
Pirani
Valve
Valve
Reservoir
10^{-3} mbar
~ $5\cdot10^{17}$ atoms/s
~ 0.02 mbar·l/s
10^{-5} mbar
Turbomolecular pump
S_2=2000 l/s
HV gauge
Gate Valve
10^{-7} mbar
TMP
S_3=200 l/s
$L_{3\text{-}4}$=5 l/s
Fluorescence Detector
MOT beams
Slower beam
10^{-9} mbar
TMP
S_4=50 l/s
HV-UHV gauge
Pirani
Valve
p_0 < $5\cdot10^{-1}$ mbar Ar during operation
< 10^{-5} mbar between runs
LN_2
Purification
Valve
Pirani
Valve
TMP
S_0=50 l/s
Dry forepump
Exhaust
*Note: Magnetic fields have to be applied to realize a Zeeman slower or a magneto optical trap

Figure 4.5.: Recirculation mode of the vacuum setup.

According to [31] the limiting factors of the recirculation mode will probably be

- cross sample contamination due to argon that has been imbedded into the vacuum parts during a former measurement which is sputtered out of the walls by the current Argon plasma
- Argon diffusing into the vacuum machine from outside

The first problem may be addressed by rinsing the entire setup with e.g. a Krypton discharge for several hours. Thereby, imbedded Argon atoms are sputtered out of the walls and are replaced by Krypton atoms. During the succeeding measurement then Krypton instead of Argon will be sputtered out of the walls by the plasma. This will deteriorate the partial pressure of argon which is tolerable up to a certain point, where the counting efficiency of ^{39}Ar is severely changed. In the Krypton setup [31] this occured after ~10 h.

The second problem may be cured by placing the entire apparatus into a big vacuum chamber.

5. Metastable Argon Source

Argon has no transition from the ground state that can be driven by currently available lasers. The potential transitions for such a laser would be the ones indicated in fig. 3.1 with 105 nm and 107 nm. The lowest wavelength for which a commercial laser is available is around 300 nm which is still far away from the required wavelength. Nevertheless, technical developments in the production of VUV-lasers should be tracked.
With the sophisticated setup in [32], the required wavelength of 105 nm has been produced by frequency up-conversion. However, this setup is far too elaborate for laser cooling.
Hence, for laser cooling the closed transition from the metastable $1s_5$ level needs to be employed, as discussed in Chapter 3.
The question rises how to populate that metastable level most efficiently, noticing that the flow of metastables in the MOT directly scales with the excitation efficiency η_{exc}.
In the following, different excitation methods and their implementation will be discussed. Subsequently, the excitation method of choice will be described in greater detail together with its technical realization.
Before proceeding to experimental results, the setup for the source characterization will be described and the theory for evaluating its signals developed.

5.1. Atom Beam Shaping

The flow of metastable Argon atoms in the MOT can already be influenced by the way the atomic beam is shaped. One can roughly distinguish between two extreme types of sources [33]: *effusive source* and *supersonic source*. An illustration of the relevant parameters in a beam shaping setup is given in fig. 5.1.

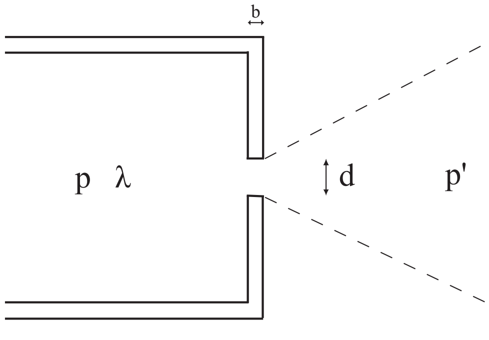

Figure 5.1.: Illustration of the relevant properties in a general source setup

The conditions of an effusive source are met when

- the thermal equilibrium in the source is not disturbed by the aperture. This can be realized if the aperture size d is small compared to the dimensions of the source chamber.
- the flow is governed by collisions with the wall (molecular flow). This is the case if the mean free path λ is much larger than the aperture size and aperture thickness, i.e. $\lambda \gg d$ and $\lambda \gg b$

If these requirements are met, the velocity distribution can be calculated exactly from thermodynamics. In spherical coordinates it writes

$$f(v, \theta) = \frac{4}{\sqrt{\pi}} \; \frac{v^2}{\hat{v}^3} \; e^{-\frac{v^2}{\hat{v}^2}} \; \cos(\theta) \tag{5.1}$$

where $v = |\mathbf{v}|$ denotes the velocity of the atom, θ the angle respective to the beam axis and $\hat{v}$ the most probable velocity. The mean free path is roughly related to the pressure by [33]

$$\lambda = \frac{66\,\mu\mathrm{m}}{p/\mathrm{mbar}} \tag{5.2}$$

For example, if the aperture is a hole with a diameter of 1 mm, the source pressure p should not exceed 10^{-3} mbar in order to stay in the effusive regime.

In the case that the flow through the aperture is governed by the collisions of atoms among each other (gasdynamic flow), i.e. when the mean free path is much smaller than the dimensions of the aperture, the source is called supersonic.
To achieve that condition either an increase in pressure or a reduction of the aperture size is needed. Increasing pressure requires a bigger pumping speed. Therefore, usually the latter possibility is exhausted as far as possible, leading to apertures of typically 10...50 μm. Still, huge pressures of some 10...100 bar in the source chamber and additional differential pumping stages are needed for this kind of source. Usually, the center beam is cut out by a so-called *skimmer* that is shaped such that it does not destroy the supersonic expansion.

Advantages of the supersonic beam over the effusive one are a higher intensity and a narrower velocity distribution — in longitudinal as well as in transverse direction [33]. The trade off is a more complicated vacuum setup and a higher longitudinal mean velocity. For example, the mean longitudinal velocity of the effusive source in [27] is ~300 m/s while the supersonic one in [33] is ~580 m/s. Such a high mean velocity would require a Zeeman-slower length of at least 2 m length. For the intended measurement of ^{39}Ar it might also be difficult to maintain the required pressures with the limited sample sizes.

5.2. Excitation methods

One can distuingish two different approaches for exciting argon atoms from the ground state to the metastable $1s_5$ state: excitation by electron impact and optical excitation.

5.2.1. Excitation by electron impact

After colliding with an electron, the argon atom is either ionized or excited to some higher level. In the latter case, the atom will deexcite either back to the ground states or to one of the metastable states. The electrons can be provided by

- electron bombardment
- DC-discharge
- RF-discharge
- microwave-discharge

Each of these excitation techniques can be combined with one of the source types described above. There exists a vast amount of papers [23, 34, 35, 36, 37, 38, 39, 40, 41] on many different combinations, that report the maximum flux-density in forward direction they achieve. Unfortunately these numbers cannot be compared directly, since the pumping speed varies from experiment to experiment, some sources are pulsed, and additionally are the flux-measurements usually only correct by a factor of 2-3. However, the best flux densities in forward direction for the different combinations are all around $10^{15}\,\frac{\text{atoms}}{\text{s}\cdot\text{sr}}$.

All these methods have the common disadvantage, that a large variety of undesired species may be produced, such as ions, photons and electrons. This drawback can be avoided if the desired state is prepared by optical pumping.

5.2.2. Optical excitation

In [38] a thermal beam of metastable Krypton has been produced by optical excitation. They report a flux density in forward direction of $3 \cdot 10^{14}\,\frac{\text{atoms}}{\text{s}\cdot\text{sr}}$ at a total gas flow rate of $3 \cdot 10^{17}\,\frac{\text{atoms}}{\text{s}\cdot\text{sr}}$. Applied to Argon, the excitation scheme would look as indicated in fig. 5.2.

The 107 nm VUV-photons could be produced in an Argon discharge flow lamp and through a VUV-window directed on the Argon beam. A laser beam of 800 nm could then pump the argon atoms from the $1s_4$ to the $2p_6$ level from where they will finally deexcite to the $1s_5$ level.

The problem remains, that for 107 nm only Lithium-Florid (LiF) windows are transparent[1], but they loose 70% of their transmission in about 3 hours and then decay more slowly over 40 hours [42]. Although the transmission can be restored by baking at 400 °C in a dry atmosphere for an hour or two, such an excitation setup is quite a challenge. Nevertheless track should be kept with new developments in VUV-windows.

---

[1] In the case of Krypton, the required wavelength is 124 nm which is within the range of MgF-windows

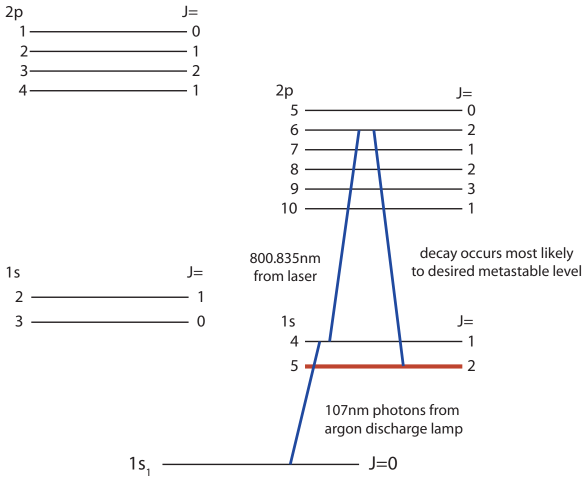
2p
J=
1
2
3
4
0
1
2
1
2p
J=
5
6
7
8
9
10
0
2
1
2
3
1
800.835nm
from laser
decay occurs most likely
to desired metastable level
1s
J=
2
3
1
0
1s
J=
4
5
1
2
107nm photons from
argon discharge lamp
1s1
J=0

Figure 5.2.: Optical excitation scheme

One could also think of combining electron and optical excitation, by e.g. shifting atoms from the other metastable level $1s_3$ to the $1s_5$ via the transition indicated in fig. 5.3. Unfortunately, the $1s_3$ metastable level is much less populated then the $1s_5$ (only about 1/4 [43]) and only some 25% of those atoms end up in the $1s_5$ state due to the branching ratios from the $1p_6$ level (see Appendix A). So finally an increase of only some 5% could be achieved this way. This explains why experimentally no improvement was observed, although a strong absorption of the pumping beam occurred.

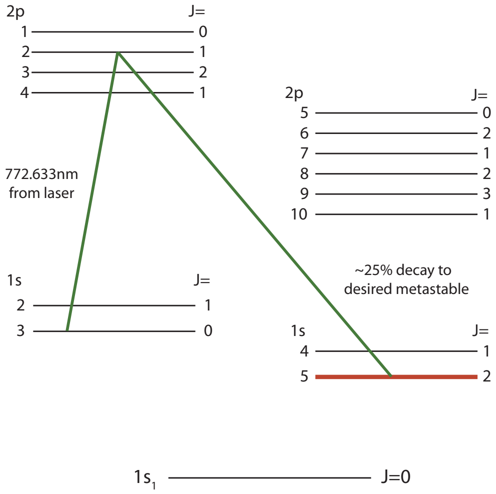
2p
J=
1
2
3
4
0
1
2
1
2p
J=
5
6
7
8
9
10
0
2
1
2
3
1
772.633nm
from laser
~25% decay to
desired metastable
1s
J=
2
3
1
0
1s
J=
4
5
1
2
1s1
J=0

Figure 5.3.: Scheme for optically shifting atoms from the $1s_3$ to the $1s_5$ metastable level

Another possibility would be to pump an intermediate short-lived level, like the $1s_4$ state for instance, since many atoms pass this level on their way to the groundstate or are excited to that state by 107nm photons from other deexciting atoms. Although again a strong absorption of the pumping beam was observed, no improvement in flux resulted. Optical excitation would definitely be the cleanest possibility of all excitation methods but the major obstacle of VUV-windows at 107 nm will need to be overcome first. In the meantime, due to its ease in construction and operation, excitation by RF-discharge is chosen, which will be described in further detail in the subsequent section.

5.3. Excitation by RF-discharge

In the RF-field, electrons and ions are accelerated and thereby collide with Argon atoms. If the electron density reaches a certain limit, a plasma is formed, visually observed as a glow discharge (fig. 5.4). In that phase transition the number of metastables increases dramatically. There exist several methods to generate a plasma through a RF-signal, as it is a standard technique in the material processing industry. A brief overview can be found in [44]. For a detailed description [45] or [46] may be consulted.

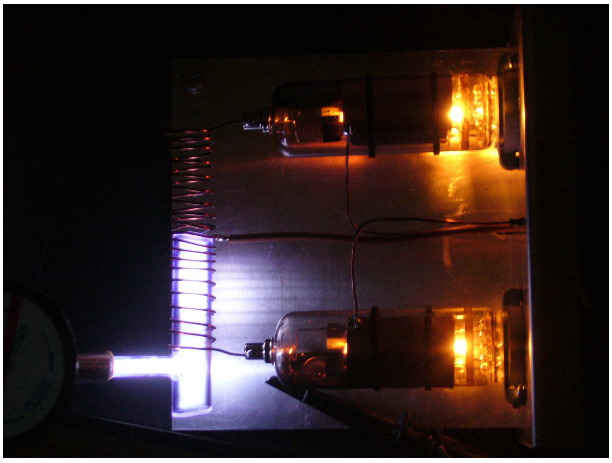

Figure 5.4.: Image of an RF-discharge induced plasma

Based on that literature and [47], a so-called inductively-coupled-plasma (ICP) seem to be the most suitable for high density plasma at low pressures.

A general setup consists of the parts indicated in fig. 5.5 where an inductive RF coupler is fed by an amplified RF-generator.

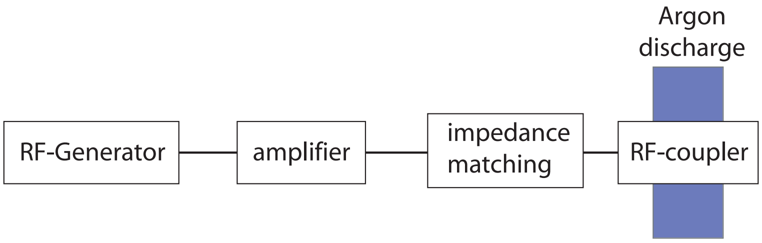

Figure 5.5.: Scheme for producing a RF-driven argon-discharge

The RF-coupler needs to be impedance-matched in order not to reflect the applied power back to the amplifier, which may potentially destroy the latter.

The RF-coupler can e.g. be realized by the geometries shown in fig. 5.3. The helical antenna [48] and the helical resonator [49] need to be driven at their resonance frequency which is determined by their geometry. The helical coil instead works in non-resonant operation and is uncritical in its geometrical dimensions.

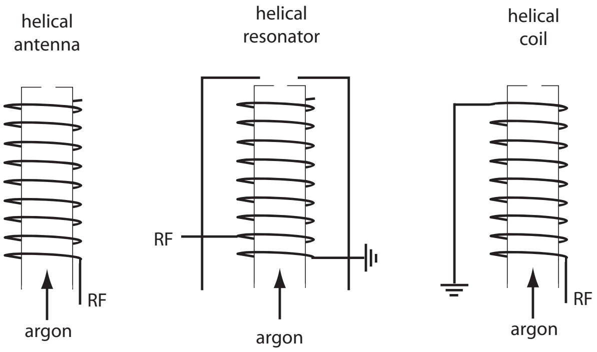

Figure 5.6.: Examples of RF-coupler

Due to their ease in construction and adaption to the vacuum system, these three geometries have been tried. Since the requirements on the RF-signal quality are not very high, inexpensive amateur-radio amplifiers and impedance matching boxes have been used.

In principle, this setup works fine but a change in the resonance frequency of the resonator and the impedance occurs upon plasma ignition. This change in resonance frequency and impedance furthermore depends on pressure and RF-power. Hence, input frequency and impedance matching need to be well adjusted whenever one of these parameters is changed.

Due to that problem a multivibrator circuit [50] has been tried, because it is self-stabilizing through a feedback-loop. In this setup, the RF-generator and the RF-coupler are the same. Therefore, the generated frequency is always the one given by the RF-coupler, even if it is changed by the plasma.

The circuit (see Appendix B) has been built with electron tubes, since they can cope with high power and are less expensive than high power transistors.

The required power supply (1kV, 300mA) is quite expensive and since it does not have to be of high quality it has also been selfmade (see Appendix C for circuit).

The apparatus proves to be far superior to the previous setup. With an input power as little as 10W it can ignite and maintain a gas discharge at pressures down to 10^{-6} mbar whereas the previous setup with a 35W amplifier cannot. Furthermore, there is no need for frequency tuning or impedance matching since it is self-stabilizing.

Due to these features it has been used to perform spectroscopy on ^{39}Ar [29], where the enriched sample is very small, such that a discharge at low pressures down to 10^{-5}mbar is required.

Unfortunately, it is difficult to assemble the multivibrator to the vacuum chamber, as the resonator needs to be inside the vacuum while the rest of the circuit should be outside. Connecting the two parts by cable leads to losses and instabilities, for the cables radiate and represent extra stray capacitances. Furthermore, do the high voltages necessary in that circuit lead to spark-overs in the vacuum due to the large presence of ions and electrons. However, in vacuum it has so far not proven superior to the other setup, apart from the convenience that it does not need to be impedance or frequency matched.

The efficiency of the different RF-setups in the production of metastables has been measured with a spectroscopy setup for source characterization, that will be explained in the following section.

5.4. Source characterization

The particular interest of the source characterization is to obtain certain properties of the metastable argon beam. Conventions for the different quantities of interest are introduced here [2].

- flow $\dot{N}$ $\left[\frac{\text{atoms}}{\text{s}}\right]$
- flux Q $\left[\frac{\text{atoms}}{\text{s m}^2}\right]$
- flux density $q(\theta)$ $\left[\frac{\text{atoms}}{\text{s sr}}\right]$, in particular the flux density in forward direction $q(0)$
- velocity distribution $f(\mathbf{v})$ of the leaving atom beam
- excitation efficiency $\eta_{exc} = \frac{\dot{N}}{\dot{N}_{tot}}$

where $\dot{N}_{tot}$ denotes the total (not only metastable) argon flow. We characterize the source by means of spectroscopy techniques, i.e. absorption and fluorescence. In order to measure the above beam properties, the setup shown in fig. 5.7 is used.

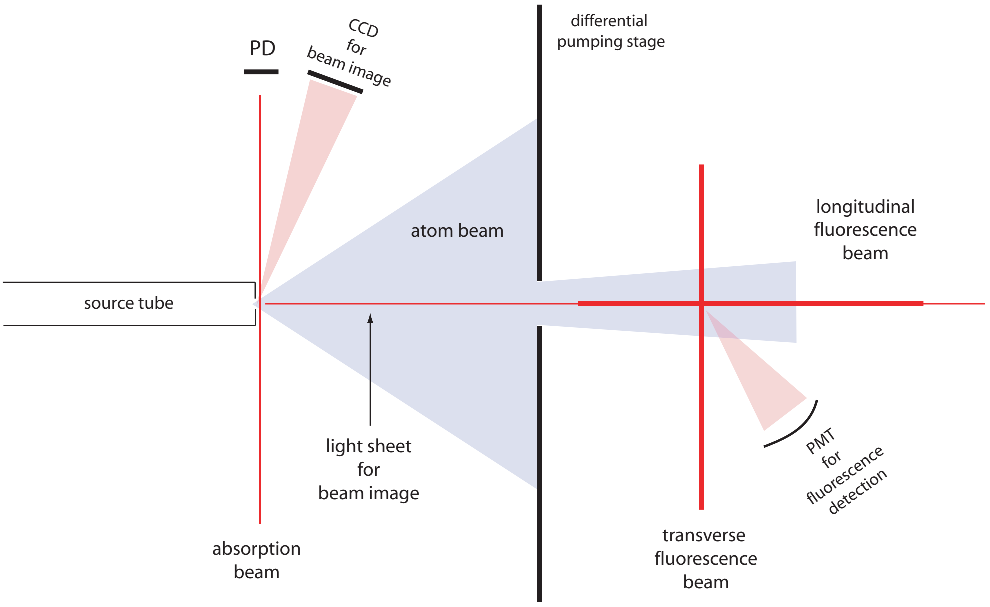
PD
CCD for beam image
differential pumping stage
atom beam
longitudinal fluorescence beam
source tube
light sheet for beam image
PMT for fluorescence detection
absorption beam
transverse fluorescence beam

Figure 5.7.: Sketch of the characterization setup

The atom beam is probed transversally right at the exit of the source tube, which allows for determining the transverse velocity profile by scanning the detuning of the probing laser beam.

The longitudinal velocity profile is obtained from the fluorescence due to longitudinal excitation measured with a Photo-Multiplier-Tube (PMT). With this information all quantities above can be deduced, as will be shown subsequently.

---

[2] these quantities are often not used consistently in literature. Therefore, the conventions made here might differ from notation elsewhere.

For checking consistency also the transversal fluorescence profile is measured. Additionally this yields the transversal profile of the atom beam behind the aperture of differential pumping stage. This will be useful to characterize the collimation.
A beam image behind the source aperture is taken by collecting the fluorescence from a longitudinal sheet of light with a CCD-camera. This image yields qualitative spatial information concerning the production of metastables. The sheet of light is produced from the longitudinal fluorescence beam by cylindrical optics placed on a pivoted arm.

Fig. 5.8 shows an exemplary characterization shot of the source at a pressure of 10^{-4} mbar using the multivibrator. The upper signal shows the absorption directly behind the source aperture whereas the longitudinal and transversal fluorescence can be observed below. At the bottom the signal from the Fabry-Perot-Interferometer (free-spectral-range of 1.5 GHz) is shown, which is used to calibrate the frequency axis.

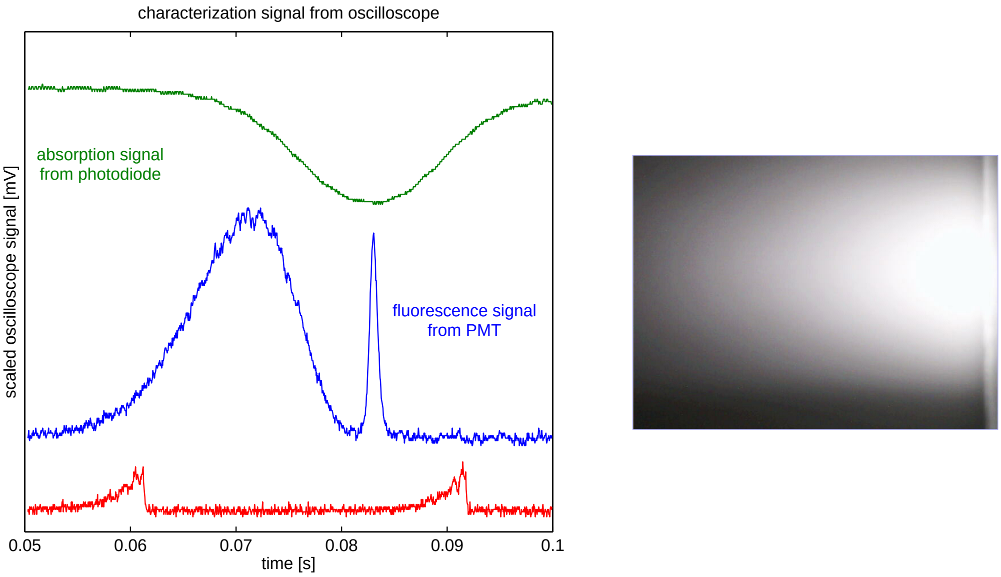

Figure 5.8.: characterization of the source: Fluorescence and absorption signal (left) and beam image (right)

Fig. 5.9 shows a Doppler fit on the absorption and the transversal fluorescence profile. Best fits for the longitudinal velocity profile were obtained assuming a 3D-Maxwell-Boltzmann distribution.

The resulting fit parameters for this measurement are shown in table 5.1, where σ_v denotes the transverse root mean square velocity, $\bar{v}$ the mean longitudinal velocity and $\hat{v}$ the most probable longitudinal velocity.

transverse absorption profile	FWHM=792 MHz	$\sigma_v = 270\,\mathrm{m/s}$
longitudinal fluorescence profile	$\hat{v} = 385\,\mathrm{m/s}$	$\bar{v} = 434\,\mathrm{m/s}$
transversal fluorescence profile	FWHM= 43 MHz	$\sigma_v = 15\,\mathrm{m/s}$

Table 5.1.: Summary of the parameters obtained from fitting the Spectroscopy signals

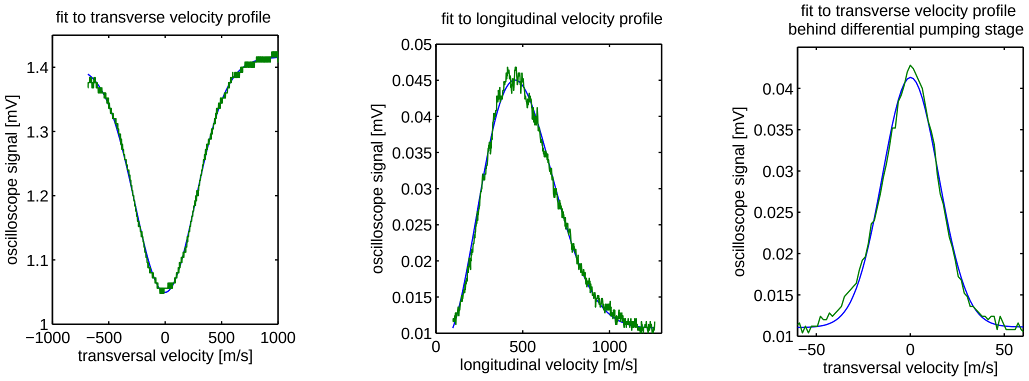

Figure 5.9.: Fits on the measured spectroscopysignals

In general the beam parameters shown for this exemplary characterization measurement depend on the source geometry, pressure, excitation method and RF-power. They also change due to heating caused by the plasma or by the dissipated RF-power as illustrated in fig. 5.10, which shows the fluorescence and the absorption signal as a function of time. The longitudinal temperature increases with time and finally saturates at some 470K after half an hour. The transverse temperature instead remains unaffected while the signal depth decreases.

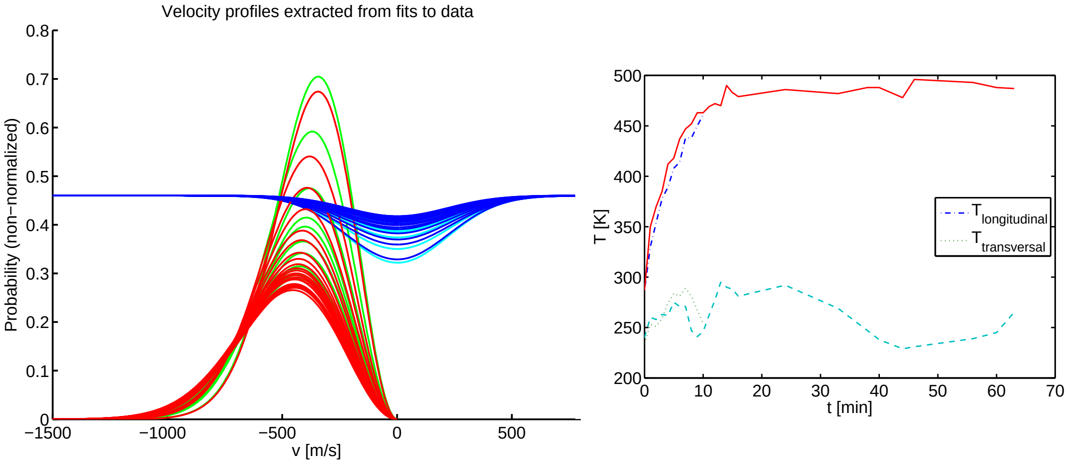

Figure 5.10.: Temperature dependence of the velocity profiles as function of time

5.5. Velocity distribution of the atom beam

The longitudinal and transversal velocity distributions obtained from different source geometries and excitation-schemes can all be described as shown above with the longitudinal velocity distribution

$$f_z(v_z) = \frac{4}{\sqrt{\pi}} \frac{v_z^2}{\hat{v}^3} e^{-\frac{v_z^2}{\hat{v}_z^2}} \tag{5.3}$$

and the transverse velocity distribution

$$f_r(v_r) = \frac{1}{\sqrt{2\pi}\sigma_v} e^{-\frac{v_r^2}{2\sigma_v^2}} \tag{5.4}$$

written in the normalized form.
The question arises how to reconstruct the total velocity distribution $f(\mathbf{v})$ from that. In cylindrical coordinates, the effusive distribution (5.1) writes

$$f(v_z, v_r) = \kappa \sqrt{v_z^2 + v_r^2}\; v_z\; e^{-\frac{v_z^2+v_r^2}{\hat{v}^2}} \tag{5.5}$$

with a normalization constant κ. The observed longitudinal velocity profile $f_z(v_z)$ then has the same shape as

$$f(v_z, 0) = \kappa\, v_z^2\, e^{-\frac{v_z^2}{\hat{v}^2}} \tag{5.6}$$

The transverse velocity profile is obtained by

$$f_r(v_r) = \int_0^\infty f(v_z, v_r)\, dv_z \tag{5.7}$$

This integral is hard to evaluate analytically. Numerical integration yields the profile shown on the left in fig. 5.11 in comparison with the velocity profile obtained from the fitting routine.

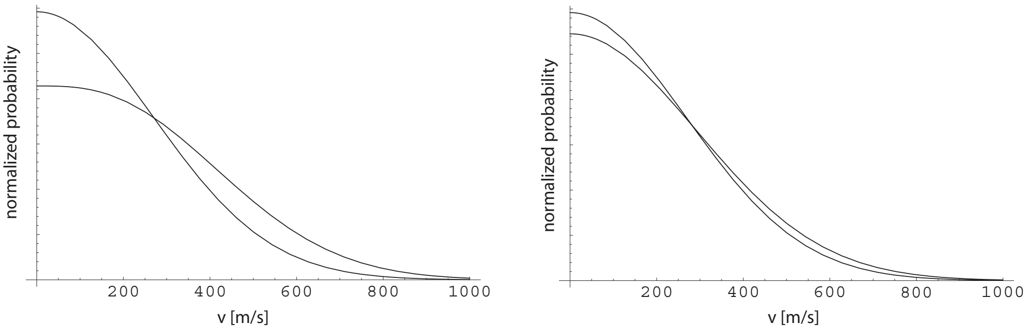

Figure 5.11.: Calculated transverse velocity profile from effusive velocity distribution (left) and from the modified effusive velocity distribution (right) in comparison with the transverse profile obtained from the fitting routine.

The effusive source does not exactly reproduce the observed transverse velocity profile. This might be due to the fact, that the condition for an effusive source, of an aperture size small compared to the dimensions of the chamber is violated. In this measurement, the diameter of the circular aperture was 6 mm while the inner diameter of the tube was 14 mm.

Assuming a slightly more forward directed flow than the effusive flow in (5.1) using a squared cosine

$$f(v,\theta) = \frac{16}{\pi^{3/2}}\,\frac{v^2}{\hat{v}^3}\;e^{-\frac{v^2}{\hat{v}^2}}\;\cos^2\theta \tag{5.8}$$

yields a better agreement as shown on the right in fig. 5.11. In this case the normalized transverse velocity profile is readily obtained to

$$f_r(v_r) = \frac{1}{\sqrt{\pi}\hat{v}}\;e^{-\frac{v_t^2}{\hat{v}^2}} \tag{5.9}$$

which is the shape of the observed transverse profile, with the rms velocity

$$v_{rms} = \frac{\hat{v}}{\sqrt{2}} \tag{5.10}$$

This discussion suggests, to use (5.8) for the velocity profile. Note that this distribution can be deduced from the mean longitudinal velocity alone.

However, depending on the aperture geometry and the temperature this distribution might change. Therefore it is preferred to use the measured width σ_v of the transverse velocity profile. With that the total velocity distribution writes

$$f(v_r,v_z) = \frac{4}{\sqrt{\pi}}\,\frac{v_z^2}{\hat{v}^3}\;e^{-\frac{v_z^2}{\hat{v}^2}}\;\frac{1}{\sigma_v^2}\;e^{-\frac{v_r^2}{2\sigma_v^2}} \tag{5.11}$$

which is normalized by the cylindrical integral

$$\int_0^\infty\int_0^\infty f(v_r,v_z)v_r dv_r dv_z = 1 \tag{5.12}$$

This velocity distribution will be used for most of the subsequent calculations.

Note that (5.8) written in cylindrical coordinates is the same as (5.11) for $\hat{v} = \sqrt{2}\,\sigma_v$.

Having found a velocity distribution that reasonably describes the observed signals, flow, excitation efficiency and flux density in forward direction can be calculated from the spectroscopy measurements.

5.6. Beam parameters from absorption

The scattering of light from a laser beam with frequency ν and intensity I results in intensity loss when the beam travels through a sample of atoms with resonance frequency ν_0 and number density n, given by [3]

$$\frac{dI}{dz} = -h\nu\gamma_s n \tag{5.13}$$

where

$$\gamma_s = \pi\Delta\nu_n \, \frac{s}{1+s+\frac{4(\nu-\nu_0)^2}{\Delta\nu_n^2}} \tag{5.14}$$

is the scattering rate, $s = \frac{I}{I_s}$ the saturation parameter , $\Delta\nu_n$ the natural linewidth of the atomic transition, I_s the saturation intensity and I the intensity of the laser.
For $s \ll 1$, i.e. for light with very little intensity, the scattering rate can be approximated to

$$\gamma_s \approx \pi\Delta\nu_n \, \frac{s}{1+\frac{4(\nu-\nu_0)^2}{\Delta\nu_n^2}} = \frac{\pi^2\Delta\nu_n^2 s}{2} \cdot \underbrace{\frac{\Delta\nu_n/2\pi}{\Delta\nu_n^2/4+(\nu-\nu_0)^2}}_{=:g(\nu)} \tag{5.15}$$

where the normalized line-shape function $g(\nu)$ has been introduced.
Inserting this into equation (5.13) and replacing $s = \frac{I}{I_s}$ yields

$$\frac{dI}{dz} = -\underbrace{\frac{\pi^2 h\nu\Delta\nu_n^2}{2I_s} g(\nu)}_{=:\sigma(\nu)} nI \tag{5.16}$$

where $\sigma(\nu)$ is the so-called scattering cross section. Recalling the saturation intensity (2.13)

$$I_s = \frac{2\pi^2 hc\Delta\nu_n}{3\lambda^3} \tag{5.17}$$

the scattering cross section becomes

$$\sigma(\nu) = \frac{3}{4}\lambda^2\Delta\nu_n g(\nu) \tag{5.18}$$

Solving differential equation (5.16) gives

$$I(z) = I_0 e^{-\sigma(\nu)nz} \tag{5.19}$$

So far the formulas are only valid for the ideal case that all atoms have the same velocity. However, the atoms have different velocities and an atom with velocity v experiences a different frequency due to the doppler shift and thus has the translated lineshape function

$$g(\nu - \nu_0\frac{v}{c}) \tag{5.20}$$

---

[3] in order to avoid any 2π-confusion, everything is expressed in terms of Hz !

If $p(v)$ denotes the velocity distribution in the gas sample, then an average lineshape function is obtained by convoluting the Lorentzian line shape function with the velocity distribution

$$\bar{g}(\nu) = \int_{-\infty}^{\infty} g(\nu - \nu_0 \frac{v}{c}) p(v) dv \tag{5.21}$$

Using the transverse velocity profile obtained in the previous section

$$p(v) = \frac{1}{\sqrt{2\pi}\sigma_v} e^{-\frac{v^2}{2\sigma_v^2}} \tag{5.22}$$

integral (5.21) can be evaluated numerically.
However, also an analytical expression can be derived, as done in the following.
One can show that for $\Delta\nu_n \ll \sigma_D := \nu_0 \frac{\sigma_v}{c}$ (i.e. the natural linewidth of the transition is much smaller than the Doppler width) $\bar{g}(\nu)$ can be approximated by the gaussian line shape function

$$\bar{g}(\nu) \approx \frac{1}{\sqrt{2\pi}\sigma_D} e^{-\frac{(\nu-\nu_0)^2}{2\sigma_D^2}} \tag{5.23}$$

Using equation (5.18) then leads to

$$\sigma(\nu) = \frac{3\lambda^2 \Delta\nu_n}{4\sqrt{2\pi}\sigma_D} e^{-\frac{(\nu-\nu_0)^2}{2\sigma_D^2}} = \sigma_0 e^{-\frac{(\nu-\nu_0)^2}{2\sigma_D^2}} \tag{5.24}$$

whose maximum value is [4]

$$\sigma_0 := \sigma(0) \approx 0.7 \cdot \lambda^2 \cdot \frac{\Delta\nu_n}{\Delta\nu_D} \tag{5.25}$$

where the FWHM Doppler width $\Delta\nu_D := \sqrt{8\ln 2}\ \sigma_D$ has been introduced.
With equation (5.19) the transmitted intensity results

$$I(\nu) = I_0 \cdot e^{-nz\sigma_0 e^{-\frac{(\nu-\nu_0)^2}{2\sigma_D^2}}} \tag{5.26}$$

with the minimum

$$I_{min} := I(\nu_0) = I_0 \cdot e^{-n\sigma_0 z} \tag{5.27}$$

Close to the minimum (5.26) may be approximated

$$I(\nu) \approx I_0 \left(1 - n\sigma_0 z e^{-\frac{(\nu-\nu_0)^2}{2\sigma_D^2}} \right) \tag{5.28}$$

Approximating I_{min} in a similar manner it turns out that the FWHM of the intensity-profile matches the FWHM $\Delta\nu_D$ of the doppler profile. So by measuring the FWHM of the intensity profile one can determine $\Delta\nu_D$ and with (5.25) thereby calculate σ_0 if the natural linewidth $\Delta\nu_n$ and the laser wavelength λ are known.

---

[4] in e.g. [51] this formula somehow appears a factor of 3 smaller

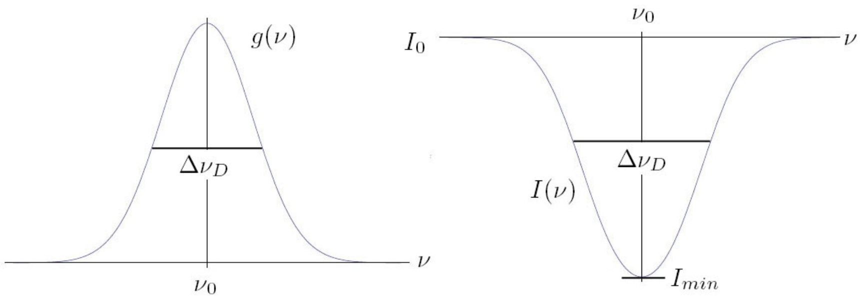

$g(\nu)$
$\Delta\nu_D$
ν
ν_0
ν_0
I_0
ν
$\Delta\nu_D$
$I(\nu)$
I_{min}

Figure 5.12.: Line-shape function and transmitted intensity vs. frequency

In the absorption setup a laser beam is transversely crossing an atomic beam of metastable Argon that is leaving a circular aperture of radius r with mean longitudinal velocity $\bar{v}$. The laser frequency is swept around the resonance frequency ν_0 of the atomic transition and the transmitted signal is observed on a photodiode.

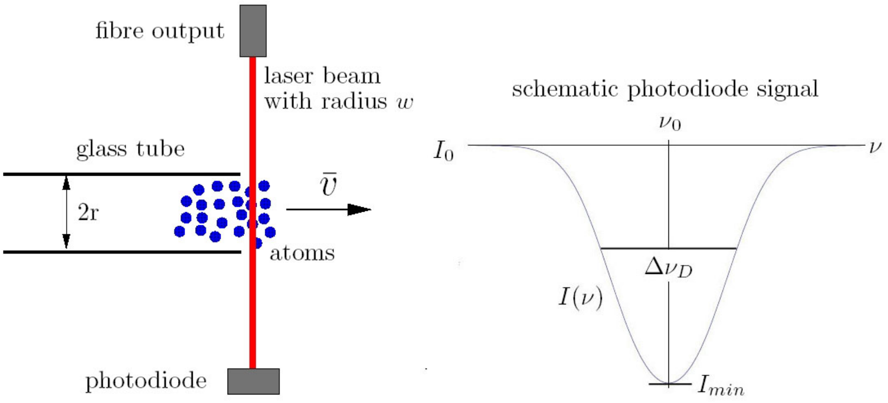

fibre output
laser beam
with radius w
glass tube
2r
$\bar{v}$
atoms
photodiode
schematic photodiode signal
ν_0
I_0
ν
$\Delta\nu_D$
$I(\nu)$
I_{min}

Figure 5.13.: setup of the absorption measurement

With the above theory one can now determine the number of metastable atoms that are leaving the aperture per second. If the radius of the laser beam is sufficiently small and if it passes right behind the source exit, the density n can be assumed to be constant over the volume passed by the laser.
Then (5.27) can be used to get

$$n = \frac{1}{\sigma_0 z} \cdot \ln\left(\frac{I_0}{I_{min}}\right) \tag{5.29}$$

From that the flux is readily obtained by integrating over the longitudinal velocity distribution

$$Q = n \cdot \bar{v} \tag{5.30}$$

If the laser beam passes very close to the aperture, then multiplying by the area of the aperture, $z = 2r$ and using (5.25) yields the flow of metastable Argon atoms

$$\dot{N} = Q \cdot \pi r^2 = \frac{\bar{v} \cdot \pi r^2}{\sigma_0 2r} \ln\left(\frac{I_0}{I_{min}}\right) = 2.3\ \frac{\bar{v}\ r}{\lambda^2} \frac{\Delta\nu_D}{\Delta\nu_n} \ln\left(\frac{I_0}{I_{min}}\right) \tag{5.31}$$

again

$$\dot{N} = 2.3\ \frac{\bar{v}\ r}{\lambda^2} \frac{\Delta\nu_D}{\Delta\nu_n} \ln\left(\frac{I_0}{I_{min}}\right) \tag{5.32}$$

inserting values from the measurement dicussed in the previous section

$$\bar{v} = 434\,\mathrm{m/s} \quad r = 3\,\mathrm{mm} \quad \lambda = 811.754\,\mathrm{nm}$$

$$\Delta\nu_n = 5.86\,\mathrm{MHz} \quad \frac{I_0}{I} = 3/2 \quad \Delta\nu_D = 792\,\mathrm{MHz}$$

yields

$$\dot{N} \approx 2.4 \cdot 10^{14} \frac{\mathrm{atoms}}{\mathrm{s}} \tag{5.33}$$

at a pressure of $p \approx 10^{-4}\,\mathrm{mbar}$, temperature $T = 300\,\mathrm{K}$ and a given pumping speed $S = 2000\,\mathrm{l/s}$ of the turbo pump, the total number of atoms passing the aperture per second is

$$\dot{N}_{tot} = \frac{Sp}{kT} = 4.83 \cdot 10^{22} \cdot p\,/\mathrm{mbar} \frac{\mathrm{atoms}}{\mathrm{s}} \approx 4.83 \cdot 10^{18} \frac{\mathrm{atoms}}{\mathrm{s}} \tag{5.34}$$

where k is the Boltzmann constant.
Thus the excitation efficiency is

$$\eta_{exc} = \frac{\dot{N}}{\dot{N}_{tot}} \approx 5 \cdot 10^{-5} \tag{5.35}$$

which is a factor of ~10 lower than what e.g. [35] reports for a similar setup with Krypton.
The flux density in forward direction $q(0)$ may be estimated by employing the velocity distribution (5.8) to get

$$q(0) = \dot{N}\ \frac{4\cos(0)^2}{\pi} \approx 3 \cdot 10^{14} \frac{\mathrm{atoms}}{\mathrm{s\ sr}} \tag{5.36}$$

5.7. Beam parameters from longitudinal fluorescence

We measure the flux density of the atom beam by fluorescence according to fig. 5.14. The detector measures the number of photons per second $\dot{N}_{ph}(\nu)$ that are emitted by the N atoms located in the fluorescing volume $V = A \cdot d$ into a solid angle $\Delta\Omega$ when probing with a laser of frequency ν.

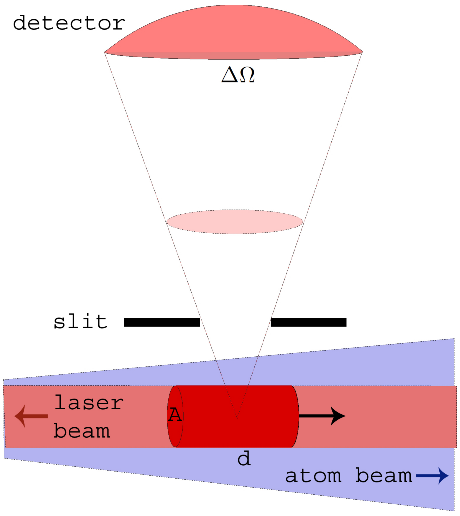

Figure 5.14.: setup of fluorescence measurement

An atom with velocity v scatteres the incident laser light with the rate $\gamma_s(\nu - \nu_0 \frac{v}{c})$. $\dot{N}_{ph}(\nu)$ then is the integral over all velocities weighted by the velocity distribution $p(v)$ and the fraction $\frac{\Delta\Omega}{4\pi \text{ [sr]}}$ of photons that reach the detector

$$\dot{N}_{ph}(\nu) = N \cdot \underbrace{\int_{-\infty}^{\infty} \gamma_s(\nu - \nu_0 \frac{v}{c}) p(v) dv}_{=:\bar{\gamma}_s(\nu)} \cdot \frac{\Delta\Omega}{4\pi \text{ [sr]}} \tag{5.37}$$

From that the number of atoms in the fluorescing volume is obtained by

$$N = \frac{\dot{N}_{ph}(\nu)}{\bar{\gamma}_s(\nu)} \cdot \frac{4\pi \text{ [sr]}}{\Delta\Omega} \tag{5.38}$$

The atom flow through the fluorescing volume then follows by integrating again over the longitudinal velocity profile, which yields

$$\dot{N}_V = \frac{N}{d} \cdot \bar{v} \tag{5.39}$$

The flux density in forward direction is then

$$q(0) = \frac{\dot{N}}{\Delta\Omega_A} \tag{5.40}$$

where Ω_A denotes the solid angle of the area A as seen from the exit of the source. Again an approximate formula as for the absorption can be derived. However, it is easier to evaluate the integral in (5.37) by computer using the previously given $\gamma_s(\nu)$ and the measured longitudinal velocity profile

$$p(v) = \frac{4}{\sqrt{\pi}} \frac{v^2}{\hat{v}^3} e^{-\frac{v^2}{\hat{v}^2}} \tag{5.41}$$

The number of photons $\dot{N}_{ph}$ is obtained from the photomultiplier signal and is calibrated against oscilloscope voltage U_{scope}

$$\dot{N}_{ph} = 2.15 \cdot 10^9 \left[\frac{\text{photons/s}}{\text{V}}\right] \cdot U_{scope} \tag{5.42}$$

Altogether, the flux density in forward direction becomes

$$q(0) = 2.15 \cdot 10^9 \left[\frac{\text{photons/s}}{\text{V}}\right] \cdot \frac{U_{scope}(\nu)}{\bar{\gamma}_s(\nu)} \frac{\bar{v}}{d} \frac{4\pi\ [sr]}{\Delta\Omega} \frac{1}{\Omega_A} \tag{5.43}$$

The longitudinal laser is produced by passing a gaussian beam of waist radius 4.2 mm through an iris with diameter $R = 2.2\,\text{mm}$, in order to approximate a homogenously saturated laser beam. With a beam power of $P = 630\,\mu\text{W}$ behind the iris, the saturation becomes

$$s = \frac{I}{I_s} = \frac{P}{\pi R^2\, I_s} = 2.75 \tag{5.44}$$

The detector area is a rectangle of size 14 mm × 8 mm at 165 mm distance from the volume which corresponds to a solid angle of

$$\Delta\Omega = 4.1 \cdot 10^{-3}\text{sr} \tag{5.45}$$

The fluorescing length is obtained from the geometry of the detector position and the vacuum setup to $d \approx 57\,\text{mm}$. The distance of the fluorescence volume is approximately 40 cm so together with the laser beam radius the solid angle of the fluorescing volume is

$$\Delta\Omega_A = \frac{\pi\ 2.2^2\,\text{mm}^2}{400^2\,\text{mm}^2} = 9.5 \cdot 10^{-4}\,\text{sr} \tag{5.46}$$

Together with the above obtained values for U_{scope} and $\hat{v} = 385\,\text{m/s}$ the flux density in forward direction becomes

$$q(0) \approx 1.1 \cdot 10^{14}\, \frac{\text{atoms}}{\text{s} \cdot \text{sr}} \tag{5.47}$$

From that the flow is obtained to

$$\dot{N} = \frac{\pi}{4}\, q(0) = 0.88 \cdot 10^{14}\, \frac{\text{atoms}}{\text{s}} \tag{5.48}$$

5.8. Beam parameters from transversal fluorescence

For consistency and for a later characterization of the collimation, we also measure the flux density of the atom beam transversally (fig. 5.15)

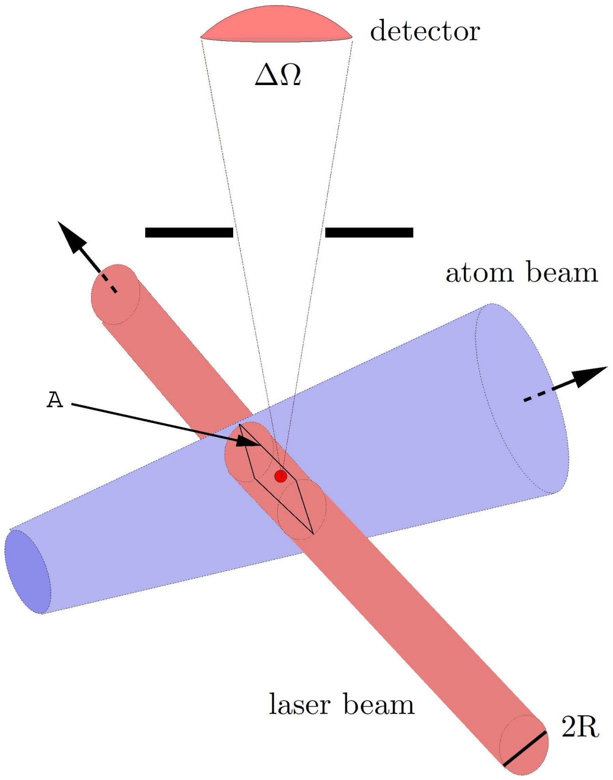

Figure 5.15.: Setup for transversal fluorescence measurement

As for the longitudinal fluorescence, the flux density in forward direction is calculated as in (5.43).

$$q(0) = 2.15 \cdot 10^9 \left[\frac{\text{photons/s}}{\text{V}}\right] \cdot \frac{U_{scope}(\nu)}{\bar{\gamma}_s(\nu)} \frac{\bar{v}}{d} \frac{4\pi\ [\text{sr}]}{\Delta\Omega} \frac{1}{\Omega_A}$$

The mean scattering rate is again obtained by

$$\bar{\gamma}_s(\nu) := \int_{-\infty}^{\infty} \gamma_s(\nu - \nu_0 \frac{v}{c})\ p(v) dv \tag{5.49}$$

but now averaging over the transverse fluorescence velocity profile

$$p(v) = \frac{1}{\sqrt{2\pi}\sigma_v} e^{-\frac{v^2}{2\sigma_v^2}} \tag{5.50}$$

The transversal laser beam has a waist radius of $R = 0.001\,\text{mm}$ and its saturation is calculated analogously as above to $s = 1.92$. The fluorescing length d is the mean over the circular laser beam, thus $d = \frac{\pi}{2} \cdot R = 1.57\,\text{mm}$. The area A is approximately the atom beam diameter [5] (9 mm) times the laser beam diameter. This gives a solid angle of

$$\Delta\Omega_A = \frac{9\,\mathrm{mm}\cdot 2\,\mathrm{mm}}{400^2\,\mathrm{mm}^2} = 1.125\cdot 10^{-4}\,\mathrm{sr} \tag{5.51}$$

Together with the above obtained values for U_{scope}, $\hat{v}$ and σ_v the flux density in forward direction becomes

$$q(0) = 3\cdot 10^{14}\,\frac{\mathrm{atoms}}{\mathrm{s}\cdot\mathrm{sr}} \tag{5.52}$$

From that the flow is obtained as

$$\dot{N} = \frac{\pi}{4}\,q(0) = 2.35\cdot 10^{14}\,\frac{\mathrm{atoms}}{\mathrm{s}} \tag{5.53}$$

5.9. Comparison of the characterization results

In general, all calculations are pessimistic, for the saturation intensity has not been corrected for magnetic substates, as discussed in Chapter 3. This might change the results by a factor of 2...3.

While the measurement from the transversal fluorescence lies close to the result from the absorption measurement, the values from the longitudinal measurement differ by a factor of ~3. The reason for that might be an uncorrectly estimated fluorescence volume. Furthermore, it was observed that the signal height can be changed by more than 20% just by changing the polarization of the laser beam. Therefore, it it possible, that the saturation intensity for a longitudinal laser beam is different then for a transversal one. However, the deviation between the results from longitudinal and transversal measurement needs further investigation.

The absorption results are believed to be the most correct ones, because they do not contain any calibration and they do not contain such a rough estimate as for the fluorescing volume.

5.10. Pressure dependence

As mentioned above, the number of metastables and thereby the overall atom flow critically depends on the pressure. Two processes are competing: the production of metastables through electron impact which increases with pressure and the deexcitation through collisions between metastable atoms, that occurs, when the mean free path becomes comparable to the dimensions of the apparatus. The uncollided flow as a function of the axial position z and the mean free path λ is [45]

$$\dot{N}(z,\lambda) = \dot{N}_0\,e^{-\frac{z}{\lambda}} \tag{5.54}$$

where $\dot{N}_0$ denotes the flow of metastables out of the source tube.

Recalling formula (5.2) for the mean free path, the flow as a function of pressure is obtained

$$\dot{N}(z,p) = \dot{N}_0\,e^{-\frac{z\cdot p/\mathrm{mbar}}{66\,\mu\mathrm{m}}} \tag{5.55}$$

---

[5] given by the size of the aperture of the differential pumping stage

Using the total argon flow as given in eq. (5.34), together with the pressure-dependent excitation efficiency $\eta_{exc}(p)$ the initial flow writes

$$\dot{N}_0 = 4.83 \cdot 10^{22} \cdot p \, \frac{\text{atoms}}{\text{mbar} \cdot \text{s}} \cdot \eta_{exc}(p) \tag{5.56}$$

So all together

$$\dot{N}(z,p) = 4.83 \cdot 10^{22} \cdot p \, \frac{\text{atoms}}{\text{mbar} \cdot \text{s}} \cdot \eta_{exc}(p) \; e^{-\frac{z \cdot p/\text{mbar}}{66\,\mu\text{m}}} \tag{5.57}$$

As long as the pressure is such, that the mean free path is much bigger than a few millimeter, the excitation efficiency can be deduced from the absorption signal right behind the source exit as described above.

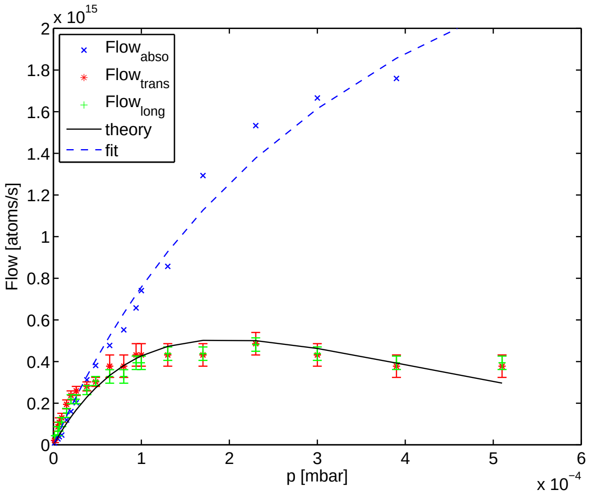

Figure 5.16.: Flow of metastables vs. pressure

To experimentally investigate the pressure dependance of the metastable flow, it has been calculated from spectroscopy measurements for different pressures. Even in the pressure regime, where the mean free path does not play a role, the flow calculated from absorption and fluorescence measurements deviates. Since the three measurements have to be equal in that regime, the fluorescing results have been scaled, such that they coincide with absorption signal (fig. 5.16).

It is visible, that for increasing pressure the flow calculated from fluorescence decreases beyond a certain optimum pressure, while the flow calculated from absorption steadily increases.

The flow from absorption $\dot{N}_{\text{abs}}(p)$ is fitted with the saturation curve indicated in 5.16, which describes the pressure dependence quite well. From that fitting curve $\dot{N}_{\text{abs}}^{fit}(p)$ the excitation efficiency is calculated as

$$\eta_{exc}(p) = \frac{\dot{N}_{\text{abs}}^{fit}(p)}{\dot{N}_{tot}(p)} \tag{5.58}$$

Using this result in (5.57) with $z = 40cm$ (the distance of the fluorescing volume), yields the theoretical curve for the fluorescence results in fig. 5.16. Note that once the fluorescence curves have been adjusted to the absorption curve, the theoretical curve fits without any calibration. Hence the pressure dependence of the signal is described well by the simple theory developed above.

The optimal pressure p_{opt} at which the metastable flow attains its maximum is obtained by

$$\dot{N}(z, p_{opt}) \overset{!}{=} 0 \tag{5.59}$$

which yields

$$p_{opt} \approx 1.8 \cdot 10^{-4}\,\text{mbar} \tag{5.60}$$

5.11. Power dependence

Besides pressure, the applied RF-power is a critical parameter for the production of metastables. In fig. (5.17) the power dependence of the flow is shown for a pressure of $3.4 \cdot 10^{-5}$ mbar, i.e. a pressure regime, where the mean free path does not play a role. The fluorescence curves have been calibrated with the same factors as above and thus do coincide with the absorption curve. The measurements have been made with the helical resonator fed by a 35 W-amplifier.

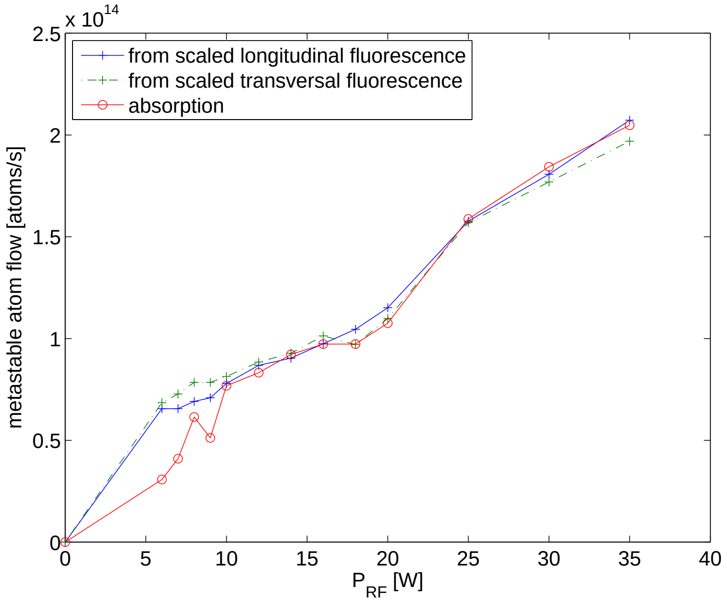

Figure 5.17.: Flow of metastables vs. power

This power dependence suggests that applying more RF-power will lead to a further increase in flow. Therefore a 200 W amplifier has been assembled behind the 35 W amplifier. Apart from several interesting side effects, a significantly higher fluorescence signal was observed but only for short till the 200 W amplifier collapsed.
Hence, future efforts in the improvement of the source will probably include robust high power RF-supplies.

6. Atomic Beam Collimation

The fraction of Argon atoms that reaches the MOT can be calculated from the velocity distribution, i.e.

$$\int_0^\infty \int_0^{v_z \frac{R_{mot}}{r_{mot}}} f(v_r, v_z) v_r dv_r dv_z \approx 4 \cdot 10^{-4} \tag{6.1}$$

if the entrance radius of the MOT $r_{mot} = 15\,\text{mm}$ is at a distance $R_{mot} = 1500\,\text{mm}$. The fraction of Argon atoms that can be detected in the MOT, i.e. those atoms that can be slowed down by the Zeeman-slower, is

$$\int_0^{v_{z,max}} \int_0^{v_z \frac{R_{mot}}{r_{mot}}} f(v_r, v_z) v_r dv_r dv_z \approx 1.3 \cdot 10^{-4} \tag{6.2}$$

where $v_{z,max}$ is the capture velocity of the Zeeman-slower and is determined by its length. For a Zeeman-slower length of 1.5 m it is $v_{z,max} \approx 500\,\text{m/s}$. Both, flow to the MOT and MOT loading rate, can be enhanced a great deal by collimating the emitted atomic beam. One mean to achieve this is by using transverse Doppler-cooling. The difficulty here is to keep atoms of a wide velocity class in resonance during the entire cooling process.

For a start, only consider atoms with a certain inital transverse velocity v_r, and further assume these atoms to remain in resonance during the entire cooling process. In this idealistic case, they experience a resonant scattering force F_{res} obtained from (2.17)

$$F_{res} = \hbar k \gamma / 2 \frac{s}{1+s} < \hbar k \gamma / 2 =: F_{max} \tag{6.3}$$

This translates into the resonant acceleration

$$a_{res} = F_{res}/m < F_{max}/m =: a_{max} \approx 2 \cdot 10^5 \frac{\text{m}}{\text{s}^2} \tag{6.4}$$

Furthermore, the cooling time

$$t_{cool} = \frac{v_r}{a_{res}} \tag{6.5}$$

is required to transversely decelerate them.

For a beam with a longitudinal velocity v_z this leads to a cooling distance of

$$l_{cool} = v_z t_{cool} = \frac{v_r v_z}{a_{res}} \tag{6.6}$$

The final radial distance then results in

$$r_{cool} = \frac{1}{2} a_{res} t_{cool}^2 = \frac{1}{2} \frac{v_r^2}{a_{res}} \tag{6.7}$$

For example, to decelerate atoms with $v_r = 55\,\text{m/s}$ and $v_z = 400\,\text{m/s}$ a cooling distance of at least 10 cm is required and and the final radial distance is ~7.5 mm, which is about the radius of the aperture to the differential pumping stage. Hence, without any transverse compression only atoms with velocities below 55 m/s can potentially be captured by Doppler-cooling. This corresponds to the following maximum fraction of atoms that can reach the MOT

$$\int_0^\infty \int_0^{55} f(v_r, v_z) v_r dv_r dv_z \approx 0.05 \tag{6.8}$$

Together with (6.1) this yields the maximum gain in flow through the MOT of

$$gain_{flow}^{max} = 125 \tag{6.9}$$

The maximum gain in the loading rate of the MOT is obtained analogously as

$$gain_{detected}^{max} \approx 240 \tag{6.10}$$

Remember, that so far all considerations have been made for the ideal case of being in resonance during the entire cooling process. The question persists how to meet this condition.

Using simple Doppler-cooling as described in Chapter 2, the resonant velocity range due to the Doppler-shift is

$$v_c \pm \Delta v = k\delta \pm \frac{1}{2} k\gamma' \tag{6.11}$$

where v_c is the resonant center velocity, Δv the resonant velocity width and $\gamma' = \gamma\sqrt{1+s}$ the power-broadened linewidth. In this scheme, the only way to remain in resonance, when the velocity is changing, is by exploiting power-broadening. Such an approach needs huge laser power. Furthermore, it has the drawback of an increasing final velocity spread, recalling from (2.33) that the Doppler-cooling limit is

$$v_D \geq \sqrt{\frac{\hbar\Gamma}{2m}} \cdot (1+s)^{1/4}$$

Another strategy is to exploit that the Doppler-shift depends on the angle between trajectory and laser beam

$$\omega_D = -\mathbf{k} \cdot \mathbf{v} = -k \cdot (v_z \sin\beta - v_r \cos\beta) \approx -k \cdot (v_z \beta - v_r) \tag{6.12}$$

in the limit of small β, where β denotes the angle between k and the transversal axis as indicated in fig. 6.1. Requiring resonance condition for the entire cooling distance yields the ideal angle β_{ideal} as a function of z

$$\omega_D(z) + \delta \overset{!}{=} 0 \quad \Leftrightarrow \quad \beta_{ideal}(z) = \beta_0 - \frac{a_{res}}{v_z^2} \cdot z \tag{6.13}$$

with

$$\beta_0 = \frac{\delta}{v_z k} + \frac{v_r}{v_z} \tag{6.14}$$

Hence with this collimation scheme it is in principle possible to transversely cool atoms with a certain initial velocity (v_z, v_r) within the given geometrical dimensions l_{cool} and r_{cool}.

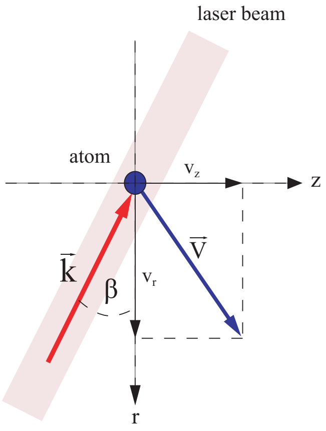

Figure 6.1.: By adapting the angle between laser beam and atom a changing Doppler-shift can be compensated.

The problem remains that not all atoms leaving the source have the same velocity but have velocities that are spread according to the distribution $f(v_z, v_r)$ described in the previous chapter.

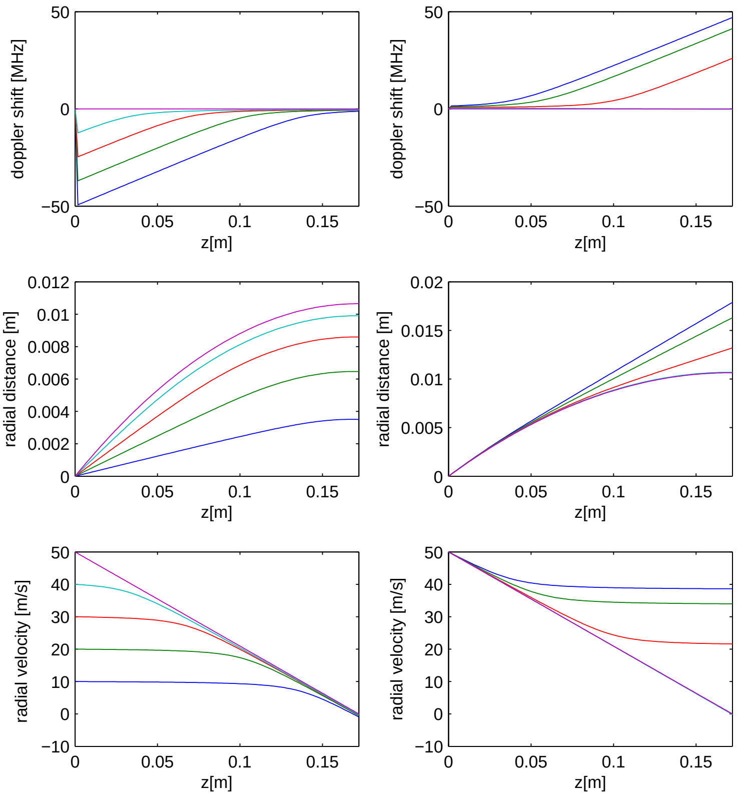

Figure 6.2.: Doppler-shift, velocity and radial distance as function of z along the collimation length. Shown are the curves for different initial radial (left) and axial velocities (right) that differ from (v_z, v_r) for which $\beta(z)$ has been chosen optimal.

Atoms with the same longitudinal velocity v_z and a smaller transversal velocity than v_r will simply get into resonance at a later point (fig. 6.2 left). Their ideal $\beta(z)$ lies on the one for (v_z, v_r). This is not the case for atoms with different longitudinal velocities, since their curves have $\beta_{ideal}(z)$ with different slopes. To a certain extent the actual $\beta(z)$ might be within the reach of the linewidth. This range may be increased by power-broadening. Again the trade-off is that of an increasing final velocity spread. The question remains of how to realize a wavefront that curves like $\beta_{ideal}(z)$. One possibility is to use a converging lens whose curvature is machined such that the right $\beta(z)$ is fulfilled, as indicated in fig. 6.3.

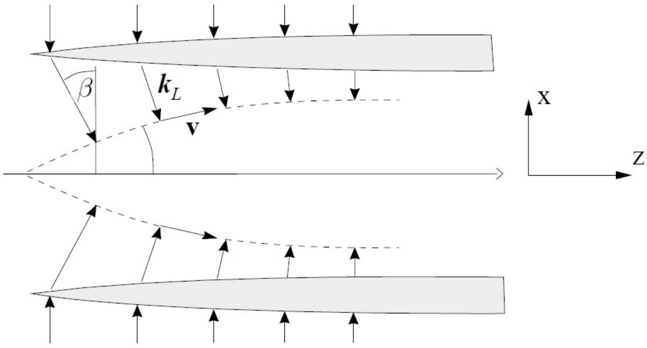

Figure 6.3.: Realization of collimation with curved wavefronts by converging lenses

Recalling the order of the required cooling distance, it becomes clear that this approach requires an enormous amount of laser power.
Another approach is to approximate $\beta_{ideal}(z)$ by the curved wavefronts obtained with tilted mirrors as sketched in fig. 6.5. This Approximation — as will be shown in the following — can be evaluated to be

$$\beta(z) \approx \beta_0 \cdot \sqrt{1 - \frac{z}{l_{cool}}} \tag{6.15}$$

and is compared with the ideal curve in fig. 6.4

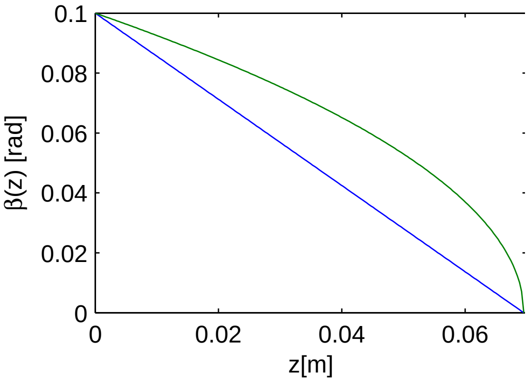

Figure 6.4.: Realization of collimation with curved wavefronts with tilted mirrors

This collimation scheme has been implemented various times with different geometries and features leading to a gain in flux density by 50 to 60 (see e.g. [52, 53, 54]). Due to its ease in construction and small power requirements this collimation scheme is also employed in this experiment.

In the following, some theoretical and geometrical aspects of this collimation scheme will be looked at. In order to find the best design parameters a simulation has been performed, which will be described subsequently and is followed by a detailed discussion of the resulting design.

6.1. Collimating with tilted mirrors

In fig. 6.5 the geometry of the collimation scheme is shown. Using basic trigonometry, the angle between the laser beam and the axis perpendicular to the z-axis can be deduced

$$\beta_n = \beta_0 - 2n\theta \tag{6.16}$$

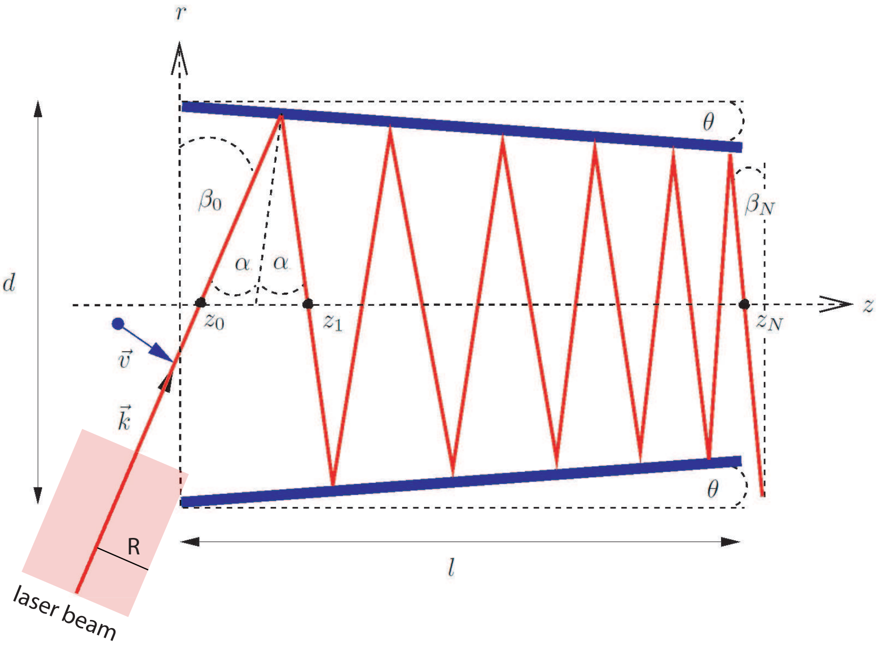

Figure 6.5.: Geometry of the collimation scheme with tilted mirrors

For the intersecting points z_n of the laser beam and the z-axis one further obtains

$$\begin{aligned} z_n &= z_{n-1} + \frac{d}{2}\left[\tan\beta_{n-1} + \tan\beta_n\right] \\ &\approx z_{n-1} + \frac{d}{2}\left[\beta_{n-1} + \beta_n\right] \\ &= z_0 + \frac{d}{2}(\beta_0 + \beta_n) + d\sum_{k=1}^{n-1}\beta_k \end{aligned}$$

Inserting (6.16) for β_k one receives

$$z_n = z_0 + \frac{d}{2}\beta_n + \frac{d}{2}n\beta_0 - \frac{d}{2}n(n-1)\theta \tag{6.17}$$

Increasing the mirror angle θ increases the number of reflected beams and therewith the beam density between the mirrors.
Nevertheless, beyond a certain angle the beam will turn around. From the previous discussion it is evident that a returning beam, e.g. going back the same way, will decollimate. Since the angle β_N at the end of the mirrors is almost zero, the detuning also needs to be close to zero to fulfill (6.13). Furthermore, (6.12) yields that the returning beam is also resonant with atoms of initial velocity v_r but the returning laser beam will accelerate into the wrong direction.
Consequently one wants the point of return to be at the very end of the mirrors, i.e.

$$z_N \overset{!}{=} l \tag{6.18}$$

where N denotes the number of the last reflection, where

$$\beta_N \overset{!}{=} 0 \qquad \Leftrightarrow \qquad N \overset{!}{=} \frac{\beta_0}{2\theta} \tag{6.19}$$

With (6.16) the corresponding maximum mirrorangle θ_{max} results

$$\theta_{max} = \frac{d}{4}\frac{\beta_0^2}{l - z_0} \tag{6.20}$$

If one chooses the distance between the laser beam center and the mirror to be the beam waist radius R, then

$$z_0 \approx \frac{d}{2}\beta_0 - \frac{2R}{\cos\beta_0} \tag{6.21}$$

The entry-angle β_0 of the laser cannot be chosen arbitrarily small, as below a minimum angle β_{min} the reflected beam would be cut off. For small θ this minimum angle can be identified as

$$\beta_{min} = \arctan\left(\frac{R}{d}\right) \tag{6.22}$$

These geometrical relations provide the basis for the calculation of the trajectory of the laser beam and determine boundary values for both laser- and mirror angle.

6.2. Simulation

Upon designing the collimation-apparatus one has to determine many design parameters, namely

- mirrorlength l
- mirrordistance d
- mirrorangle θ
- entry-angle of laser beam β_0
- laser power P
- laser detuning δ
- beam waist radius R
- number of beams (2 or 4)

Altogether these are 8 free parameters. Although the discussion in the previous section might have given a feeling for effects of certain parameters, it is very hard to decide intuitively or analytically upon the best choice of parameters. The main difficulty is set by the vast range of the inital velocity distribution. Therefore, a detailed simulation has been performed to obtain the best choice of parameters.

The whole mirror region is discretized in a $N \times N$-grid. For a given mirror geometry as well as for given laser parameters the trajectory of a Gaussian laser beam is calculated, in particular the angle β_n and the wavevector $\mathbf{k}$ of each partial beam. From that the intensity field $I(z,r) = \sum I_k(z,r)$ of the laser beam is derived (see fig. 6.6) using a mirror-reflectivity of 99% which is slightly below the manufacturer's specifications. Absorption losses have been neglected because the density of ^{39}Ar is far too small to have any noticable effects and ^{40}Ar is far off resonance.

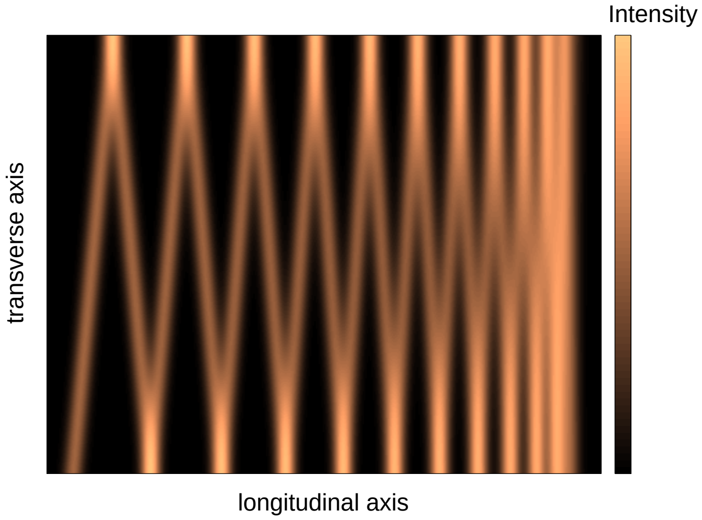

Figure 6.6.: Calculated intensity field of the laser for a given geometry

The trajectory of an atom with initial velocity $(v_z, v_r(0))$ during the collimation process is then calculated iteratively by simply assuming a uniformely accelerated motion in one time step $\Delta t = \frac{l}{N \cdot v_z}$ where v_z is assumed to be constant.

$$\begin{aligned} a(t) &= \frac{F}{m} \\ v_r(t) &= v_r(t-1) + a(t) \cdot \Delta t \\ r(t) &= r(t-1) + v_r(t) \cdot \Delta t \end{aligned}$$

The question arises how to calculate the force F that acts on the atom. Since the low-saturation regime is not the one of interest simply adding the forces of the different laser beams could lead to unphysical scattering rates bigger than $\gamma/2$. For this reason an effective saturation parameter for each laser beam is defined

$$s_i^{\text{eff}} = \frac{s_i}{1 + \frac{4\Delta_i^2}{\gamma^2}} \tag{6.23}$$

where

$$s_i = s_i(r, z) = \frac{I_i(r, z)}{I_s}$$

is the saturation parameter of the i-th beam and

$$\Delta_i = \delta - \mathbf{k}_i \cdot \mathbf{v} = \delta - k[v_z \beta_i - v_r(z)]$$

the sum of laser detuning δ and doppler shift. The corresponding photon scattering rate γ_i can then be calculated as

$$\gamma_i = \frac{\gamma}{2} \frac{s_i^{\text{eff}}}{1 + \sum s_j^{\text{eff}}} \tag{6.24}$$

which can be considered as a normalized version of the scattering rate.
The associated forces

$$F_i = \hbar k \gamma_i \tag{6.25}$$

can then be summed to obtain the total force

$$F = \sum F_i \tag{6.26}$$

At the end of the collimation process the trajectory is extrapolated to find whether the atom can reach the MOT or not.
Heating effects due to spontaneous emission are neglected, since this would increase the calculation time dramatically. Due to the large set of parameters to be varied the calculation time is already very long. Possible heating effects may be estimated by the final velocity spread (2.33).
Being able to calculate the trajectory of one atom with a particular initial velocity (v_z, v_r), the next step is to calculate trajectories for the entire velocity distribution $f(v_z, v_r)$. Subsequently the fraction of atoms reaching the MOT is obtained by evaluating the cylindrical integral

$$in\_MOT = \int_0^\infty \int_0^\infty in\_mot(v_r, v_z) \cdot f(v_z, v_r) v_r dv_z dv_r \tag{6.27}$$

with

$$in\_mot(v_z, v_r) = \begin{cases} 1 & \text{atom reaches MOT} \\ 0 & \text{otherwise} \end{cases} \tag{6.28}$$

The gain in flow can then be calculated by dividing the fraction of atoms reaching the MOT with and without collimation, i.e.

$$gain_{flow} = \frac{in\_MOT_{\text{on}}^{\text{collimation}}}{in\_MOT_{\text{off}}^{\text{collimation}}} \tag{6.29}$$

If instead one is interested in the gain of the MOT loading rate, than only the velocity range that can be slowed down by the Zeeman-slower needs to be considered. Thus, the fraction of detected atoms is

$$Detected = \int_0^\infty \int_0^{v_{z,max}} in\_mot(v_r, v_z) \cdot f(v_z, v_r) v_r dv_z dv_r \tag{6.30}$$

The corresponding gain then writes

$$gain_{detected} = \frac{Detected_{\text{on}}^{\text{collimation}}}{Detected_{\text{off}}^{\text{collimation}}} \tag{6.31}$$

Note that this is already the 3D-gain, since the spherical integration is already included in $f(v_z, v_r)$. Examplery trajectories for a given geometry are shown in fig. 6.7.

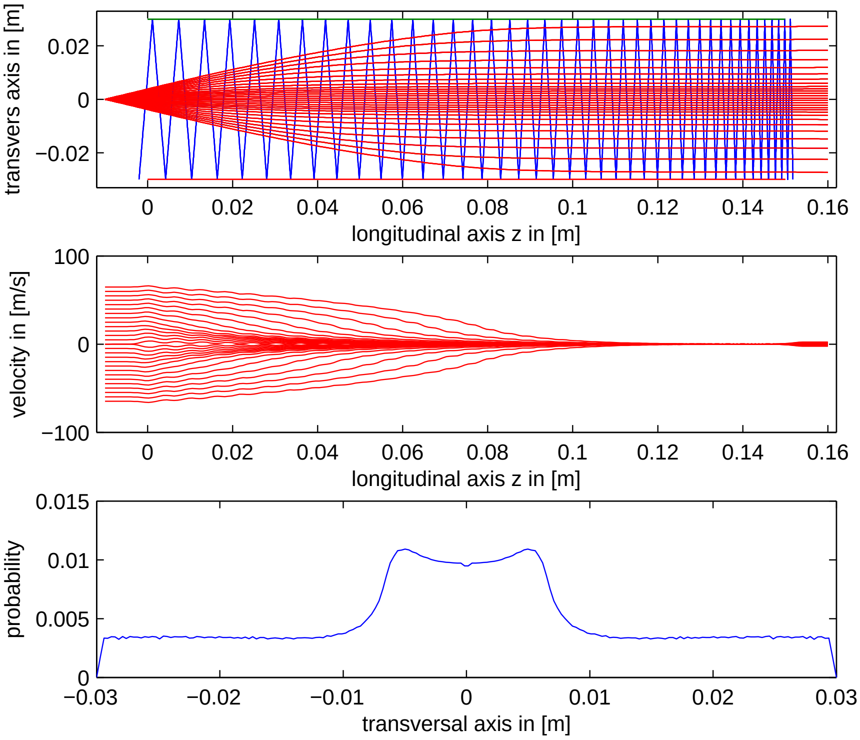

Figure 6.7.: Trajectories and velocities as functions of z plotted for different initial velocities. The bottom plot shows the atomic beam profile at the exit of the collimation region

For simplicity, the aperture of the source is assumed to be a point. Simulations including the width of the apperture reproduce the same results as long as the aperture does not exceed the dimension of the entrance of the differential pumping stage.
Initial velocities that can be detected in the MOT are plotted in fig. 6.8 on top of the entire velocity distribution. Here, a maximum longitudinal velocity of $v_{z,max} = 500\,\mathrm{m/s}$ has been chosen.

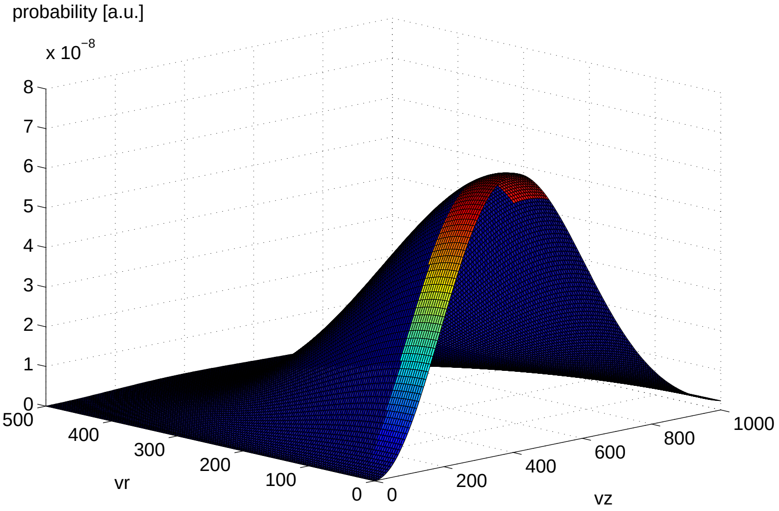

Figure 6.8.: Fraction of the velocity distribution that is detected in the MOT

To make sure that the mirror region and the velocity distribution is sufficiently discretized the simulation has been let run for different numbers N of iteration steps and for different velocity discretizations N_{v_z}, N_{v_r}. It results that the gain converges for increasing values and that for $N = N_{v_z} = N_{v_r} = 150$ the error is less then 5%.

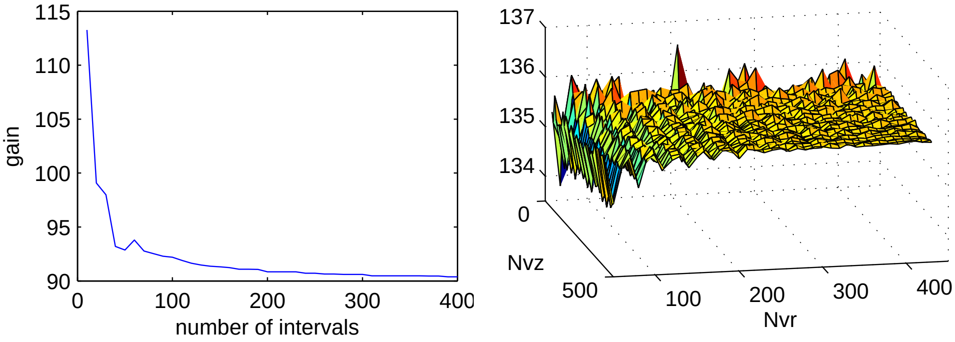

Figure 6.9.: Gain as function of discretization steps

Now the search for the optimal design parameters shall start:
For fixed mirror geometry, laser beam radius and power the simulation calculates the

gain over a wide mirrorangle/laserangle/detuning range. This yields that the entry angle of the laser beam β_0 always tends towards the minimum angle β_{min} while the mirrorangle always tends towards θ_{max} (fig. 6.10).

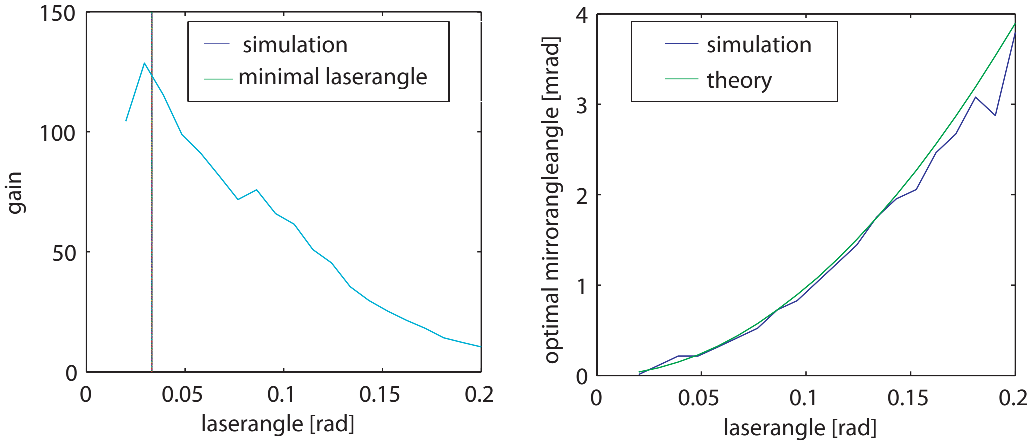

Figure 6.10.: Maximum gain as function of the laserangle β_0 (left) and optimal mirrorangle as function of laserangle (right)

Since this is case for various random mirror geometries and laser beam parameter these findings are assumed to be the general case. Therefore these 2 parameters are from now on fixed which reduces the number of free parameters by 2 and thereby drastically shortens the calculation time for a simulation run.
Furthermore, it results that changing the mirrordistance does not have any effect apart from different β_{min} and θ_{max} according to formula (6.22) and (6.20) respectively. Therefore, this parameter is also fixed to $d = 6\,\text{cm}$, which is the largest technically possible value due to mechanical limitations of the vacuum setup.
The mirrorlength confines the maximum cooling distance and thereby also the velocity range, that can be captured. Hence, one would expect the gain to increase with the mirrorlength saturating when reaching the boundary parts of the velocity distribution. This is confirmed by the simulation results and plotted in fig. 6.11. Based on these curve the mirrorlength has been chosen $l = 15\,\text{cm}$.

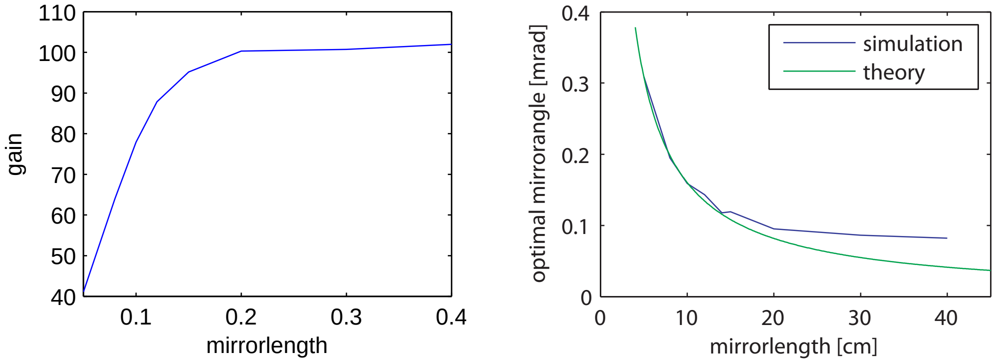

Figure 6.11.: Maximum gain as function of mirrorlength l (left) and optimal mirrorangle as function of mirrorlength (right) for a total laser power of 100 mW

Next, the effect of laser power is considered. With increasing saturation the scattering force approaches the maximum force F_{max} as well as the maximum velocity range, that can potentially be captured, is reached. Thus, the gain is expected to saturate with increasing laser power. This is indeed the case as fig. 6.12 shows together with the increasing optimal detuning.

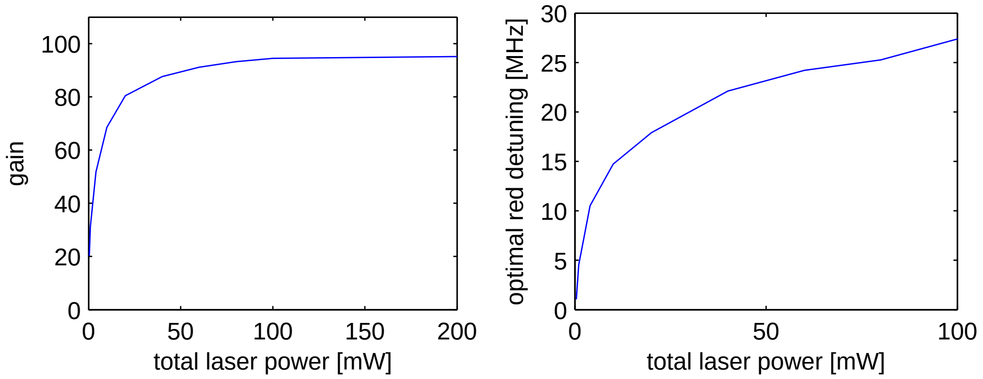

Figure 6.12.: Gain (left) and optimal red detuning vs. total laser power

The laser beam radius resulted to be uncritical and has been chosen to $R_z = 2.5\,\mathrm{mm}$ in longitudinal direction. To ensure coverage of the entire atom beam, the radius in the other direction has been chosen comparable to the aperture of the differential pumping stage to $R_x = 9\,\mathrm{mm}$.

The detuning remains a free parameter in all simulations. This way the experimental situation is reflected, where the detuning is an adjustable knob, that can be turned easily.

Fig. 6.13 shows how the gain depends on the detuning and the mirrorangle while keeping all other parameters fixed. Changing the mirrorangle only by some 100 μrad already results in a decrease in gain by a factor of 2. Hence, adjusting the mirrorangles requires precise control.

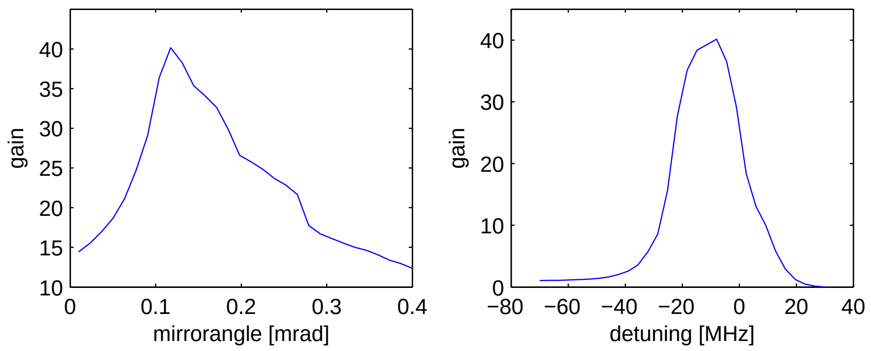

Figure 6.13.: Maximum gain as a function of the mirrorlength l (left) and optimal mirrorangle as a function of the mirrorlength (right) for a total laser power of 20 mW. For large red detuning the gain converges to unity since the laser beam is far off resonance. For large positive detuning the laser beam decollimates the atom beam and thus the gain tends to zero.

Finally, setting the total laser power to 100 mW the resulting design parameters obtained from simulation are summarized in table 6.2.

mirrorlength	150mm
mirrordistance	60mm
laser beam diameter	5 mm × 18 mm
entry angle of laser beam	33 mrad
mirrorangle	0.11 mrad
detuning	$-2\pi \cdot 25$ MHz
laser power	100 mW
$gain_{flow}$	100
$gain_{detected}$	190

Note that the gain values are close to the maximum possible gain values (6.9) and (6.10) obtained from theoretical considerations.

The gain might be further increased by additional low-saturation molasses to compensate for the remaining velocity spread as done in [52].
Recalling, that the velocity range that can be captured is limited by the apperture of the entry hole to the next stage, another possibility to increase gain would be to not only collimate the beam but to also compress it with a magneto-optical-lens as done in [55].

6.3. Design

Based on the simulation results the collimator has been designed such that it can be aligned outside the vacuum and then be assembled as a whole (fig. 6.14.)

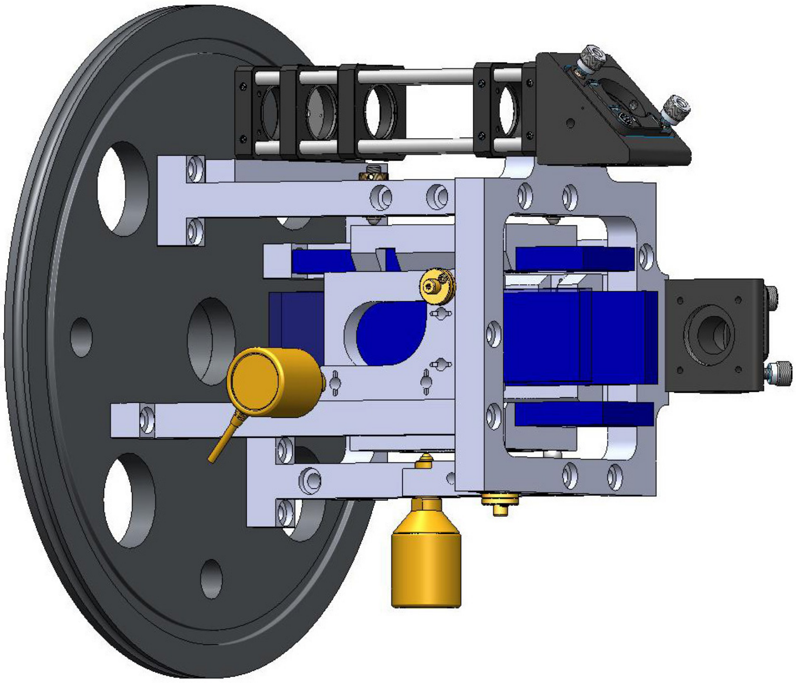

Figure 6.14.: Technical drawing of the collimator

The assembling is achieved by mounting the entire apparatus on the exit flange (ISO-250-K), which bears two optical vacuum feedthroughs for introducing the laser beams. The fibre is connected to the beam shape optics, which are mounted on the collimator frame via a cage system. The laser beam-shaper consists of a fibre port and two cylindric lenses that produce an elliptical beam with 5 mm $\times$ 18 mm diameter followed by a mirror that allows precise alignment of the laser beam into the collimator mirrors. Two of those are 15 cm $\times$ 4 cm big while the others are 1 cm longer for easier laser beam coupling. All mirrors bear a dielectric coating and have a reflectivity bigger than 99.7%. This is important considering the large number of reflections.

The simulation shows that the laser beam angle is best chosen to be minimal and that little deviations from the optimum can be compensated by adapting the mirrorangle. Therefore, β_0 is aligned once outside the vacuum with manual screws and from then on stays fixed.

The mirrorangles instead can be varied from outside the vacuum with stepper motors which allows for fine-adjustment on the flux signal. Nevertheless, the mirrorangles can be pre-aligned outside the vacuum to θ_{max}, where the number of reflections is maximum and the laser beam is just before returning. As shown above, the resolution for adjusting the mirrorangle needs to be some 10 μrad, which translates into a required resolution of about 1 μm for the stepper motors, easily fulfilled by the ones chosen (Newport NSA200,

resolution 100nm).
The mirror-holders as well as the collimator frame have been carefully machined by the workshop division. Fig. 6.15 shows the machined collimator.

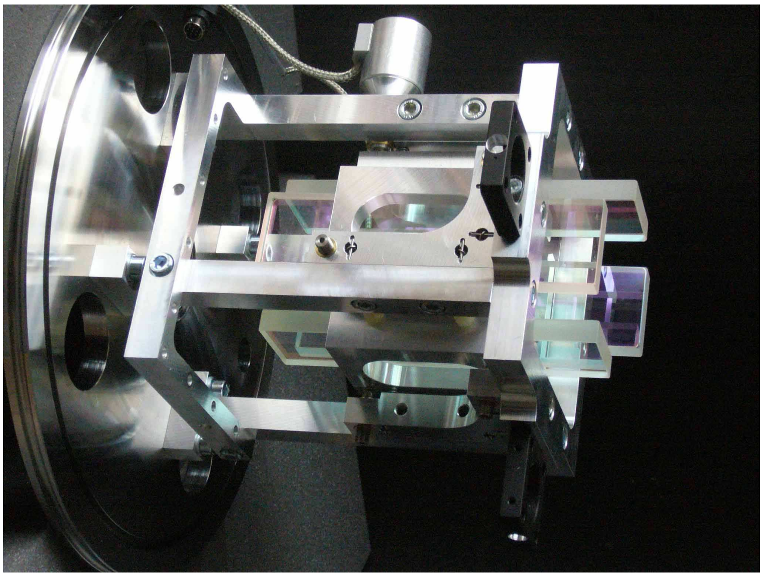

Figure 6.15.: Picture of the machined collimator

6.4. First result

The manufacturing of the collimator was accomplished right before handing this thesis in. Nevertheless, it has been assembled, which took less than a day, to have a first glance. The longitudinal fluorescence profile with and without collimation is shown in fig. 6.16.

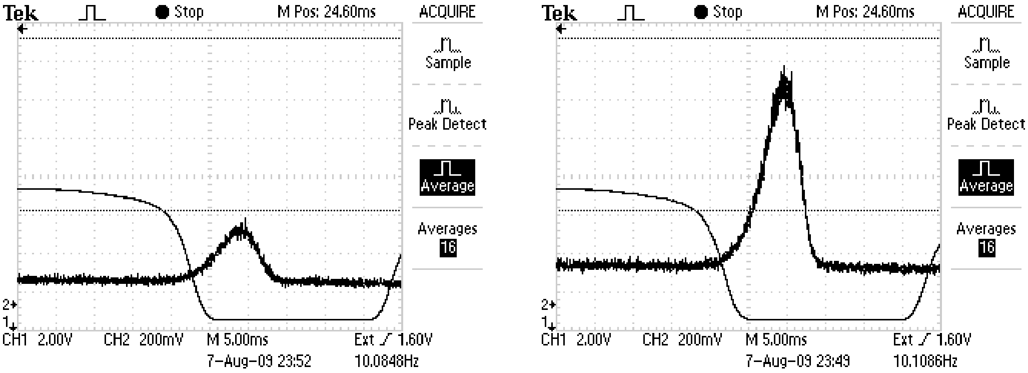

Figure 6.16.: First signal of the longitudinal fluorescence profile without collimation (left) and with collimation (right)

First the signal without collimation shall be considered. As calculated in the previous Chapter, the longitudinal fluorescence signal is proportional to the flux density in forward direction $q(0)$. From that the flow of metastable atoms in the MOT is obtained to

$$\dot{N}_{MOT} = q(0) \cdot \Omega_{MOT} \tag{6.32}$$

where

$$\Omega_{MOT} = \frac{\pi r_{mot}^2}{R_{mot}^2} \tag{6.33}$$

denotes the solid angle of the MOT aperture, $R_{mot} \approx 1500\,\mathrm{mm}$ the distance of the MOT from the source and $r_{mot} \approx 15\,\mathrm{mm}$ the radius of the MOT entrance.
Now the signal with collimation is considered. Since the atom beam is now collimated, the flow in the MOT is the same as if the MOT was at the point, where the fluorescence is measured. This corresponds to an effective solid angle

$$\Omega'_{MOT} = \frac{\pi r_{mot}^2}{R_{mot}'^2} \tag{6.34}$$

where $R'_{mot} \approx 400\,\mathrm{mm}$ is the distance of the fluorescing volume from the source exit. Thus, the flow in the MOT would be

$$\dot{N}'_{MOT} = q(0)' \cdot \Omega'_{MOT} \tag{6.35}$$

Obtaining $q(0)' \approx 3.5\ q(0)$ from the comparison of the two signal maxima in fig. 6.16, the flow enhancement through the MOT results

$$\frac{\dot{N}'_{MOT}}{\dot{N}_{MOT}} = \frac{q(0)'}{q(0)} \cdot \frac{R^2}{R'^2} \approx 3.5 \cdot \left(\frac{1500\,\mathrm{mm}}{400\,\mathrm{mm}}\right)^2 \approx 50 \tag{6.36}$$

This experimental gain is smaller than the gain obtained from simulation by a factor of two. However, note that this result was measured with only very rough alignment due to lack of time. The laser angle was not exactly set to β_{min} and the resolution of the stepper motors has not been set down to the required level. Hence, also the mirrorangles could not be adjusted to its optimum value θ_{max}. Furthermore, the laser that provided the collimation beams was not stabilized. Thus, a drift in detuning ocurred which deteriorated the collimation. A significant improvement in flow-gain is expected by curing above defects.

7. Summary and Outlook

A summary of this work and at the same time an outlook will be given, by collecting experimental values from the foregoing chapters and using them for an estimation of the counting rate of ^{39}Ar in the MOT.

7.1. Estimation of the ^{39}Ar counting rate in the MOT

The number of ^{39}Ar atoms being detected in the MOT per second is

$$\dot{N}_{mot} = \dot{N}_{tot} \cdot R \cdot \eta_{geom} \cdot \eta_{exc} \cdot \eta_{coll} \cdot \eta_{zs} \cdot \eta_{mot} \cdot \eta_{hfs} \tag{7.1}$$

where

$$\dot{N}_{tot} = 4.83 \cdot 10^{22} \cdot p\,/\mathrm{mbar} \frac{\mathrm{atoms}}{\mathrm{s}}$$

is the previously introduced total number of atoms leaving the source per second, which is maximum for the pressure

$$p \approx 10^{-4}\,\mathrm{mbar} \tag{7.2}$$

The isotopic ratio of an argon sample of age t is

$$R = \frac{N_{39}}{N_{40}} = 8.1 \cdot 10^{-16} \cdot e^{-\ln 2\ t/\tau} \tag{7.3}$$

where $\tau = \ln 2\, T_{1/2}$ is the mean half-life introduced in Chapter 1. Inserting a reasonable value for the age of a water sample

$$t = 3\ \tau \approx 540\,\mathrm{a}$$

yields

$$R \approx 10^{-16} \tag{7.4}$$

The fraction of atoms that reaches the MOT without any manipulation,

$$\eta_{geom} \approx 4 \cdot 10^{-4} \tag{7.5}$$

was obtained from the velocity distribution in Chapter 5.

$$\eta_{exc} \approx 5 \cdot 10^{-5} \tag{7.6}$$

is the excitation efficiency, also obtained in Chapter 5.

$$\eta_{coll} = 100 \tag{7.7}$$

is the gain in flux produced by the collimation, discussed in Chapter 6.

$$\eta_{zs} \approx 0.6 \tag{7.8}$$

is the fraction of atoms that leave the Zeeman-slower which can be detected in the MOT, assuming a zeeman slower length of 1.5 m[1].

$$\eta_{mot} \approx 0.8 \tag{7.9}$$

is the fraction of atoms entering the MOT that is detected [30].
As described in chapter three ^{39}Ar splits into 5 hyperfine levels. Therefore only $\frac{1}{5}$th of the ^{39}Ar atoms can be detected. Assuming a further repumper yields

$$\eta_{hfs} \approx 2/5 \tag{7.10}$$

Inserting all these numbers in (7.1) gives

$$\dot{N}_{mot} \approx 1\,\frac{\text{atoms}}{\text{h}} \tag{7.11}$$

Assuming Poisson distribution for 5% accuracy one needs at least

$$\frac{\sqrt{N}}{N} \overset{!}{=} 0.05 \quad \Leftrightarrow \quad N \overset{!}{=} 400 \quad {}^{39}\text{Ar atoms} \tag{7.12}$$

which results in a measuring time of

$$t_{counting} \approx 12\,\text{days} \tag{7.13}$$

This result is not very promising, considering that a measuring time of a couple of hours is intended. However, the excitation efficiency might have been underestimated, due to the insecurity in the saturation intensity. Furthermore, can the excitation efficiency be further enhanced by using more RF power, as was shown in Chapter 5. If this is still not enough, a more sophisticated collimation scheme may be employed, e.g. including a compression stage.
Before closing this thesis, a little outlook is given, how a future dating procedure might take place.

7.2. Measurement of a natural water sample

This ATTA project at the university of Heidelberg is a collaboration between the group of Markus K. Oberthaler at the Kirchhoff Institute for Physics (KIP) and the group of Werner Aeschbach-Hertig at Institute for Environmental Physics (IUP). The latter group is in charge of sample processing, i.e. degassing and Argon extraction. Thereafter, the extracted argon would be introduced to the ATTA-apparatus and the counting rate of ^{39}Ar in the MOT is measured. For an example, in the ATTA setup for Krypton described in [31] e.g. the counting rate for ^{81}Kr is $\sim 10\,\frac{\text{atoms}}{\text{h}}$. Since the quantity of interest is the isotopic ratio

---

[1] this results from the velocity distribution integrated over longitudinal velocity up to $v_{z,max} = 500\,\text{m/s}$

$$R_{sample} = \frac{^{39}\text{Ar}}{\text{Ar}} \tag{7.14}$$

measuring only ^{39}Ar is not enough.
Strategies to measure the ratio could be

- calibrating the setup with a modern sample. Its corresponding counting rate in the MOT would define the modern standard
- on the timescale of ^{39}Ar, the isotope ^{81}Kr is stable. Since its wavelength is very close to the one of ^{39}Ar, its counting rate could be measured concurrently in the same setup. From the ratio of counting rates the isotopic ratio of ^{39}Ar could be obtained.
- spiking the sample with a well defined amount of an argon isotope. If the abundance of the spiking isotope is of the same order as ^{39}Ar, both isotopes could be counted concurrently. The spiking isotope would thereby provide the modern standard.

The progress of the experiment will show, which method proves best.

A. Detailed transition scheme of ^{40}Ar

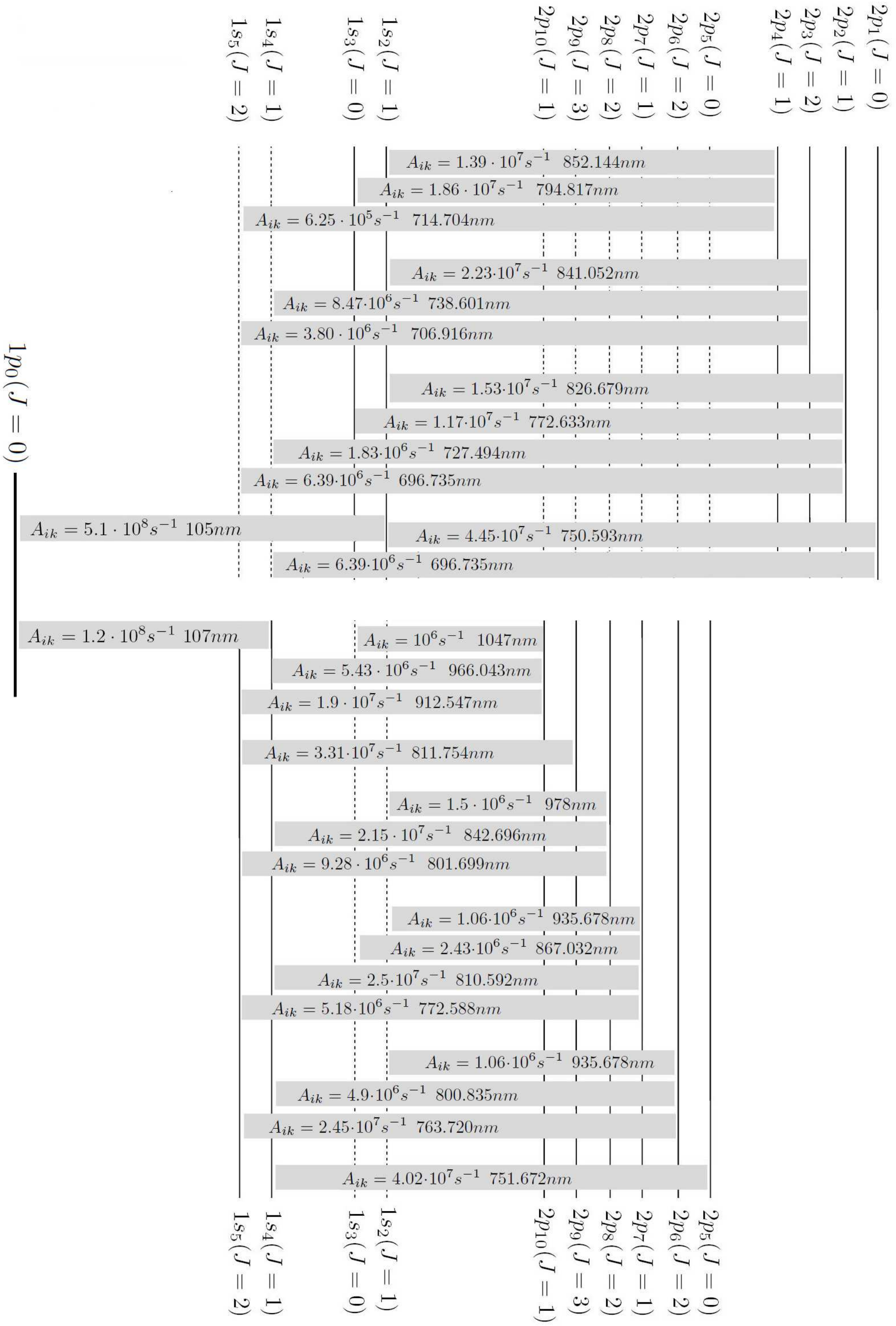
$2p_1(J=0)$
$2p_2(J=1)$
$2p_3(J=2)$
$2p_4(J=1)$
$2p_5(J=0)$
$2p_6(J=2)$
$2p_7(J=1)$
$2p_8(J=2)$
$2p_9(J=3)$
$2p_{10}(J=1)$
$1s_2(J=1)$
$1s_3(J=0)$
$1s_4(J=1)$
$1s_5(J=2)$
$1p_0(J=0)$
$A_{ik} = 1.39 \cdot 10^7 s^{-1}$ $852.144nm$
$A_{ik} = 1.86 \cdot 10^7 s^{-1}$ $794.817nm$
$A_{ik} = 6.25 \cdot 10^5 s^{-1}$ $714.704nm$
$A_{ik} = 2.23 \cdot 10^7 s^{-1}$ $841.052nm$
$A_{ik} = 8.47 \cdot 10^6 s^{-1}$ $738.601nm$
$A_{ik} = 3.80 \cdot 10^6 s^{-1}$ $706.916nm$
$A_{ik} = 1.53 \cdot 10^7 s^{-1}$ $826.679nm$
$A_{ik} = 1.17 \cdot 10^7 s^{-1}$ $772.633nm$
$A_{ik} = 1.83 \cdot 10^6 s^{-1}$ $727.494nm$
$A_{ik} = 6.39 \cdot 10^6 s^{-1}$ $696.735nm$
$A_{ik} = 5.1 \cdot 10^8 s^{-1}$ $105nm$
$A_{ik} = 4.45 \cdot 10^7 s^{-1}$ $750.593nm$
$A_{ik} = 6.39 \cdot 10^6 s^{-1}$ $696.735nm$
$A_{ik} = 1.2 \cdot 10^8 s^{-1}$ $107nm$
$A_{ik} = 10^6 s^{-1}$ $1047nm$
$A_{ik} = 5.43 \cdot 10^6 s^{-1}$ $966.043nm$
$A_{ik} = 1.9 \cdot 10^7 s^{-1}$ $912.547nm$
$A_{ik} = 3.31 \cdot 10^7 s^{-1}$ $811.754nm$
$A_{ik} = 1.5 \cdot 10^6 s^{-1}$ $978nm$
$A_{ik} = 2.15 \cdot 10^7 s^{-1}$ $842.696nm$
$A_{ik} = 9.28 \cdot 10^6 s^{-1}$ $801.699nm$
$A_{ik} = 1.06 \cdot 10^6 s^{-1}$ $935.678nm$
$A_{ik} = 2.43 \cdot 10^6 s^{-1}$ $867.032nm$
$A_{ik} = 2.5 \cdot 10^7 s^{-1}$ $810.592nm$
$A_{ik} = 5.18 \cdot 10^6 s^{-1}$ $772.588nm$
$A_{ik} = 1.06 \cdot 10^6 s^{-1}$ $935.678nm$
$A_{ik} = 4.9 \cdot 10^6 s^{-1}$ $800.835nm$
$A_{ik} = 2.45 \cdot 10^7 s^{-1}$ $763.720nm$
$A_{ik} = 4.02 \cdot 10^7 s^{-1}$ $751.672nm$
$2p_5(J=0)$
$2p_6(J=2)$
$2p_7(J=1)$
$2p_8(J=2)$
$2p_9(J=3)$
$2p_{10}(J=1)$
$1s_2(J=1)$
$1s_3(J=0)$
$1s_4(J=1)$
$1s_5(J=2)$

B. circuit of multivibrator

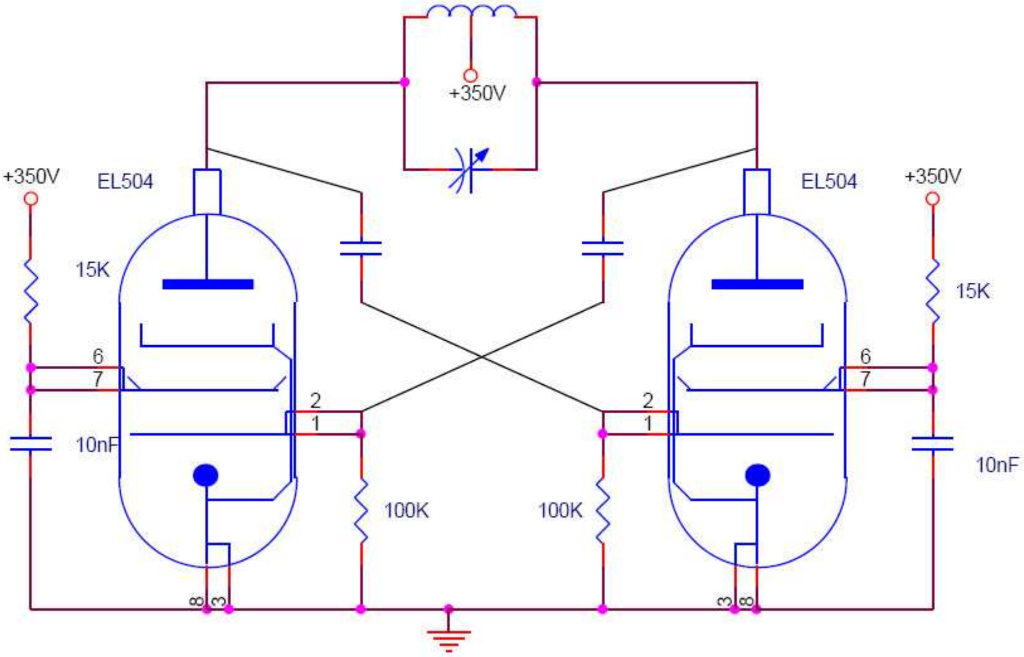
+350V
+350V
EL504
+350V
EL504
+350V
15K
15K
6
7
6
7
2
1
2
1
10nF
10nF
100K
100K
8
3
3
8

C. circuit of power supply

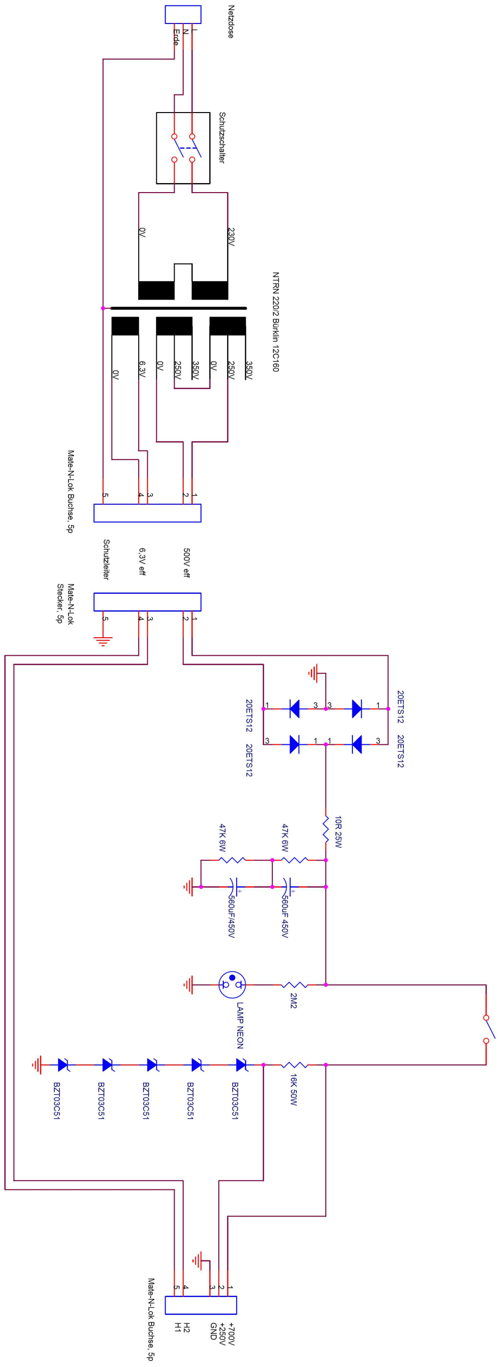
Netzdose
L
N
Erde
Schutzschalter
0V
230V
NTRN 220/2 Bürklin 12C160
0V
6,3V
0V
250V
350V
0V
250V
350V
Mate-N-Lok Buchse, 5p
5
4
3
2
1
Schutzleiter
6,3V eff
500V eff
Mate-N-Lok Stecker, 5p
5
4
3
2
1
20ETS12
20ETS12
20ETS12
20ETS12
1
3
3
1
3
1
1
3
10R 25W
47K 6W
47K 6W
560uF/450V
560uF 450V
2M2
LAMP NEON
16K 50W
BZT03C51
BZT03C51
BZT03C51
BZT03C51
BZT03C51
Mate-N-Lok Buchse, 5p
1
2
3
4
5
+700V
+250V
GND
H2
H1

D. Some constants

Table D.1.: Physical constants and properties of argon.

Atomic Mass Unit amu	$1.66053886 \cdot 10^{-27}$ kg	
Planck constant h	$6.626068 \cdot 10^{-34} \frac{\mathrm{m^2 \cdot kg}}{\mathrm{s}}$	
Boltzmann constant k_B	$1.3806503 \cdot 10^{-23} \frac{\mathrm{m^2 \cdot kg}}{\mathrm{s^2 \cdot K}}$	
Bohr magneton μ_B	$9.27400949 \cdot 10^{-24} \frac{\mathrm{J}}{\mathrm{T}}$	
Speed of light c	$2.99792458 \cdot 10^{8} \frac{\mathrm{m}}{\mathrm{s}}$	
Magnetic permeability μ_0	$1.25663706 \cdot 10^{-6} \frac{\mathrm{m \cdot kg}}{\mathrm{s^2 \cdot A^2}}$	
Isotope	^{40}Ar	^{39}Ar
Relative abundance	0.996	$8.5 \cdot 10^{-16}$
Mass m	39.96 amu	38.96 amu
Halflife time $\mathrm{T}_{1/2}$	-	269a
Nuclear spin I	0	$+\frac{7}{2}$
Nuclear magnetic moment μ/μ_K	-	-1.3
Relevant transition	$1s_5 - 2p_9$	
Ground state Landé factor g_g	1.506	
Excited state Landé factor g_e	1.338	
Wavelength λ	811.757 nm	
Linewidth γ	$2\pi \cdot 5.85$ MHz	
Lifetime τ	27.09 ns	
Saturation intensity I_0	$1.44 \frac{\mathrm{mW}}{\mathrm{cm^2}}$	
Doppler temperature T_D	141 μK	

E. acknowledgements

I want to thank

- Markus Oberthaler and Werner Aeschbach-Hertig for supervising and grading my diploma work, fruitful discussions, expertise, inspiration and finally for initiating this wonderful project
- Joachim Welte for introducing me to the experiment, team work, plasma fun, being a never fading source of energy, last-minute assembling of the collimator and much more
- all Argonauts for being a great team, steady cooperativeness, enlivening office ours and proof-reading this work. In particular
  - Jiri Tomkovic for plenty computer support and being a major tomatoe and egg customer
  - Michael Schreiber for electronic support and botanic excursions
  - Isabelle Steinke for a pleasant time in the ATTA-lab and the Yoga room
  - Matthias Henrich for bearing my long legs and painting the collimator
- Fabienne Haupert, for carefully proof-reading this thesis and a – in every respect – well-climated last week in her office
- Thomas Reichelt for productive collaboration and measuring the Radon content of my tab-water
- all matterwavers for waving matters and being a great team
- Jürgen Schölles for steady electronic support and introduction to higher dimensional physics
- all members of the workshop division, especially
  - Julia Bing, Michael Lutz, Morris Weisser and Werner Lamade for building an excellent collimator, being a great help during its construction and finishing it before my diploma deadline
  - Siegfried Spiegel for introducing me to his reign and many mechanical solutions
- Winfried Schwarz and Mario Trieloff from the geologic institute for fruitful collaboration
- Ms. Scheurich for blowing us the most ingenious things from glass

- the Karrengang for keeping many hidden treasures
- Henry Westphal for great support with the multivibrator
- Erika and Martin Schindler for everything
- Daniel Ritterbusch for being my brother and culinary advisor
- all Wildwuchs gardeners for a memorable time and many veggies
- my body and brain for surviving the last four weeks without severe damage

Bibliography

[1] F. Kahn. *Das Atom - endlich verständlich.* 1949.

[2] P. Collon, W. Kutschera, and Z.-T. Lu. Tracing noble gas radionuclides in the environment. *Annual Review of Nuclear and Particle Science*, 54(1):39–67, 2004.

[3] C. Y. Chen, Y. M. Li, K. Bailey, T. P. O'Connor, L. Young, and Z.-T. Lu. Ultrasensitive Isotope Trace Analyses with a Magneto-Optical Trap. *Science*, 286(5442):1139–1141, 1999.

[4] N. C. Sturchio, X. Du, R. Purtschert, B.E. Lehmann, M. Sultan, L. J. Patterson, Z. T. Lu, P. Mueller, T. Bigler, K. Bailey, T. P. O'Connor, L. Young, R. Lorenzo, R. Becker, Z. El Alfy, B. El Kaliouby, Y. Dawood, and A. M. A. Abdallah. One million year old groundwater in the sahara revealed by krypton-81 and chlorine-36. *Geophys. Res. Lett.*, 31:L05503, 2004.

[5] I. D. Moore, K. Bailey, J. Greene, Z.-T. Lu, P. Müller, T. P. O'Connor, Ch. Geppert, K. D. A. Wendt, and L. Young. Counting Individual Ca41 Atoms with a Magneto-Optical Trap. *Phys. Rev. Lett.*, 92(15):153002, 2004.

[6] S. Hoekstra, A. K. Mollema, R. Morgenstern, H. W. Wilschut, and R. Hoekstra. Single-atom detection of calcium isotopes by atom-trap trace analysis. *Phys. Rev. A*, 71(2):023409, Feb 2005.

[7] H.H. Loosli. A dating method with 39Ar. *Earth and Planetary Science Letters*, 63(1):51 – 62, 1983.

[8] Werner Aeschbach-Hertig. Physics of Aquatic Systems II, lecture notes.

[9] W. Aeschbach-Hertig. private communication.

[10] H.H. Loosli and H. Oeschger. Detection of 39Ar in atmospheric argon. *Earth and Planetary Science Letters*, 5:191 – 198, 1968.

[11] J. A. Corcho Alvarado, R. R. Purtschert, F. Barbecot, C. Chabault, J. Rueedi, V. Schneider, W. Aeschbach-Hertig, R. Kipfer, and H. H. Loosli. Constraining the age distribution of highly mixed groundwater using 39ar: A multiple environmental tracer (3h/3he, 85kr, 39ar, and 14c) study in the semiconfined fontainebleau sands aquifer (france). *Water Resour. Res.*, 43, 2007.

[12] P. Cook and A. Herczeg. *Environmental tracers in subsurface hydrology.* Kluwer academic publishers, 1968.

[13] J. A. Corcho Alvarado, Barbecot, R. Purtschert, M. Gillon, W. Aeschbach-Hertig, and R. Kipfer. European climate variations over the past half-millennium reconstructed from groundwater. *Geophys. Res. Lett.*, in press, 2009.

[14] H.H. Loosli, M. Möll, H. Oeschger, and U. Schotterer. Ten years low-level counting in the underground laboratory in Bern, Switzerland. *Nuclear Instruments and Methods in Physics Research Section B: Beam Interactions with Materials and Atoms*, 17(5-6):402 – 405, 1986.

[15] Ph. Collon, M. Bichler, J. Caggiano, L. Dewayne Cecil, Y. El Masri, R. Golser, C. L. Jiang, A. Heinz, D. Henderson, W. Kutschera, B. E. Lehmann, P. Leleux, H. H. Loosli, R. C. Pardo, M. Paul, K. E. Rehm, P. Schlosser, R. H. Scott, W. M. Smethie, and R. Vondrasek. Development of an AMS method to study oceanic circulation characteristics using cosmogenic 39Ar. *Nuclear Instruments and Methods in Physics Research Section B: Beam Interactions with Materials and Atoms*, 223:428 – 434, 2004. Proceedings of the Ninth International Conference on Accelerator Mass Spectrometry.

[16] W. Kutschera, M. Paul, I. Ahmad, T.A. Antaya, P.J. Billquist, B.G. Glagola, R. Harkewicz, M. Hellstrom, D.J. Morrissey, R.C. Pardo, K.E. Rehm, B.M. Sherrill, and M. Steiner. Long-lived noble gas radionuclides. *Nuclear Instruments and Methods in Physics Research Section B: Beam Interactions with Materials and Atoms*, 92(1-4):241 – 248, 1994.

[17] Rodney Loudon. *The quantum theory of light.* Oxford Univ. Press, Oxford [u.a.], 2008.

[18] Claude Cohen-Tannoudji, Bernard Diu, and Franck Laloë. *Quantum mechanics.* Wiley [u.a.], New York [u.a.].

[19] Claude Cohen-Tannoudji, Jacques Dupont-Roc, and Gilbert Grynberg. *Atom-photon interactions.* Wiley-VCH, Weinheim, 2004.

[20] P. W. Milonni and J. H. Eberly. *Lasers.* Wiley, New York, NY [u.a.], 1988.

[21] H. J. Metcalf and P. v. Straten. *Laser cooling and trapping.* Springer, New York ; Berlin ; Heidelberg [u.a.], 1999.

[22] T. Gruner and D.-G. Welsch. Green-function approach to the radiation-field quantization for homogeneous and inhomogeneous kramers-kronig dielectrics. *Phys. Rev. A*, 53(3):1818–1829, Mar 1996.

[23] Robin Kaiser Alain Aspect, Nathalie Vansteenkiste. Preparation of a pure intense beam of metastable helium by laser cooling. *Chemical Physics*, 145:307–315, 1990.

[24] W. Roedel. *Physik unserer Umwelt: die Atmosphäre.* Springer, Berlin ; Heidelberg [u.a.], 1994.

[25] V. D. Ashitkov, A. S. Barabash, S. G. Belogurov, G. Carugno, S. I. Konovalov, I. O. Pilugin, G. Puglierin, R. R. Saakyan, V. N. Stekhanov, V. I. Umatov, and I. A. Vanushin. New experimental limit on the 42Ar content in the Earth's atmosphere. *Nuclear Instruments and Methods in Physics Research Section A: Accelerators, Spectrometers, Detectors and Associated Equipment*, 416(1):179 – 181, 1998.

[26] The Berkeley Laboratory Isotopes Project.

[27] H. Gauck. Ein quasi-zweidimensionales Gas ultrakalter Argonatome vor einer Oberfläche. Master's thesis, University of Konstanz, 1999.

[28] I. Steinke. Diplomarbeit.

[29] J. Welte, I. Steinke, M. Henrich, F. Ritterbusch, M. K. Oberthaler, W. Aeschbach-Hertig, W. Schwarz, and M. Trieloff. Hyperfine spectroscopy of the 1s5-2p9 transition of 39Ar. *unpublished.*

[30] J. Welte. Single atom detection by fluorescence. Master's thesis, University of Heidelberg, 2007.

[31] X. Du, K. Bailey, Z.-T. Lu, P. Mueller, T. P. O'Connor, and L. Young. An atom trap system for practical 81Kr dating. *Review of Scientific Instruments*, 75(10):3224–3232, 2004.

[32] I. Velchev, W. Hogervorst, and W. Ubachs. Precision vuv spectroscopy of ar i at 105 nm. *J. Phys. B: At. Mol. Opt. Phys.*, 32:L511ŰL516, 1999.

[33] H. Pauly. *Basic theory, production and detection of thermal energy beams*, volume 28. Springer, Berlin ; Heidelberg ; New York, 2000.

[34] B. Brutschy and H. Haberland. A high-intensity beam of metastable helium atoms with good velocity resoiution. *Journal of Physics E: Scientific Instruments*, 10:90–94, 1976.

[35] C. Y. Chen, K. Bailey, Y. M. Li, T. P. O'Connor, Z.-T. Lu, X. Du, L. Young, and G. Winkler. Beam of metastable krypton atoms extracted from a rf-driven discharge. *Review of Scientific Instruments*, 72(1):271–272, 2001.

[36] M. DeKieviet, M. Durr, S. Epp, F. Lang, and M. Theis. Source for atomic beams of metastable gases: Design and performance. *Review of Scientific Instruments*, 75(2):345–348, 2004.

[37] Y. Ding, K. Bailey, A. M. Davis, S.-M. Hu, Z.-T. Lu, and T. P. O'Connor. Beam of metastable krypton atoms extracted from a microwave-driven discharge. *Review of Scientific Instruments*, 77(12):126105, 2006.

[38] Y. Ding, S.-M. Hu, K. Bailey, A. M. Davis, R. W. Dunford, Z.-T. Lu, T. P. O'Connor, and L. Young. Thermal beam of metastable krypton atoms produced by optical excitation. *Review of Scientific Instruments*, 78(2):023103, 2007.

[39] D. W. Fahey, W. F. Parks, and L. D. Schearer. High flux beam source of thermal rare-gas metastable atoms. *Journal of Physics E: Scientific Instruments*, 13(4):381–383, 1980.

[40] A. Faulstich, A. Schnetz, M. Sigel, T. Sleator, O. Carnal, V. Balykin, H. Takuma, and J. Mlynek. Strong Velocity Compression of a Supersonic Atomic Beam Using Moving Optical Molasses. *EPL (Europhysics Letters)*, 17(5):393–399, 1992.

[41] R. S. Freund. High current low voltage electron bombarder for excitation of a molecular beam. *Review of Scientific Instruments*, 41(8), 1970.

[42] Resonance Ltd. private communication Bill Morrow.

[43] G. A. Hebner and P. A. Miller. Behavior of excited argon atoms in inductively driven plasmas. *Journal of Applied Physics*, 87(12):8304–8315, 2000.

[44] H. Conrads and M. Schmidt. Plasma generation and plasma sources. *Plasma Sources Science and Technology*, 9(4):441–454, 2000.

[45] A. J. Lichtenberg M. A. Lieberman. *Principles of plasma discharges and materials processing.* JOHN WILEY & SONS, INC., 1994.

[46] A. A. Fridman and L. A. Kennedy. *Plasma physics and engineering.* Taylor & Francis, New York [u.a.], 2004.

[47] Michael A. Lieberman. private communication.

[48] J. Schölles. private communication.

[49] R.O. Schildknecht W. W. MacAlpine. Coaxial resonator with helical inner conductor. *proceedings of the IRE*, 47:2099–2105, 1959.

[50] Sascha Laue, Michael Schüler, and Henry Westphal. *private communication and "Die Oszillatoren 50..70MHz und 140 MHz", AbschluSSbericht Mixed Signal Baugruppen*, 2006.

[51] B. E. Saleh and M. C. Teich. *Fundamentals of photonics.* Wiley, Hoboken, N.J., 2007.

[52] C. Slowe, L. Vernac, and L. V. Hau. High flux source of cold rubidium atoms. *Review of Scientific Instruments*, 76(10):103101, 2005.

[53] W. Rooijakkers, W. Hogervorst, and W. Vassen. An intense collimated beam of metastable helium atoms by two-dimensional laser cooling. *Optics Communications*, 123(1-3):321 – 330, 1996.

[54] Kawanaka. Generation of an intense low-velocity metastable-neon atomic beam. *Applied Physics B: Lasers and Optics*, Volume 56, Number 1, 1993.

[55] M. D. Hoogerland, J. P. J. Driessen, E. J. D. Vrcdenbregt, H. J. L. Megens, M. P. Schuwer, H. C. W. Beijerinck, and K. A. H. van Leeuwen. Bright thermal atomic beams by laser cooling: A 1400-fold gain in beam flux. *Applied Physics B: Lasers and Optics*, Volume 62(4):323–327, 1996.

Declaration:

I hereby confirm that I wrote this thesis on my own and that I did not use other sources or means than stated.

Heidelberg, the ______________________ ______________________

Signature